Mechanically Robust

Compositionally Complex Alloys

Submitted by: Simon Jason Tsianikas

                                 ID: 1607246

Principal Supervisor: Zonghan Xie

                                 School of Mechanical Engineering

Co-supervisor: Yujie Chen

                                 School of Mechanical Engineering

Thesis submitted for the degree of Doctor of Philosophy

The University of Adelaide

School of Mechanical Engineering

Table of Contents

List of Figures

Abstract

Compositionally complex alloys (CCAs), including high- and medium- entropy alloys and steels, defy conventional alloy design rules by including multiple principal elements in the alloy composition. This has unlocked the possibility to synthesise an endless list of compositionally unique alloys with unfathomable properties, which could be applied in many industries such as power generation, manufacturing, and aerospace. Among the myriad of attractive properties, much research has been undertaken into their mechanical properties, including investigations into in how these materials are challenging the frontiers of strength-ductility limitations. This requires deep analysis into the structure-property relationship of these alloys, focussing on the role and evolution of nano-structural features, grain boundaries, and crystal structure, in response to deformation. The aim of this research work is to characterise the deformation mechanisms of CrCoNi and FeMnCoCr-based CCAs, and develop insight into how materials can be engineered to exhibit optimum mechanical properties.

The first chapter of this thesis introduces the field of CCAs, highlighting the key developments and innovations in the field thus far, provides a summary of strengthening mechanisms, and introduces aims and objectives of the thesis. The second chapter presents an overview of the methodology applied, including preparation, fabrication, structural and chemical characterisation, and mechanical testing techniques.

In the third chapter, an analysis of the deformation mechanisms of hierarchical nanostructured CrCoNi with dual-phase face-centred cubic (FCC) and hexagonal

closed-packed (HCP) phases is conducted. The results suggest that multiple deformation pathways could be activated in CrCoNi with assistance of growth defects, thereby imparting this technically important alloy with appreciable ductility.

The fourth chapter focusses on a body-centred cubic (BCC) FeMnCoCr-based interstitial high entropy alloy (iHEA) which incorporates B, C and O. The unusual combination of hardening effects brought about by interstitial strengthening, grain boundary segregation engineering, compositional fluctuations, and fine grain size, greatly strengthened the alloy by inhibiting dislocation motion. Deformation induced HCP/FCC nanolaminates enhanced plasticity via strain partitioning. Taken together, the newly developed BCC-structured iHEA affords not only high strength, but also confers remarkable ductility through multiple deformation pathways.

In the fifth chapter, a $Fe_{72.4}Co_{13.9}Cr_{10.4}Mn_{2.7}B_{0.34}$ high entropy steel is investigated. The distribution of iron and chromium shows an unusual, characteristic spinodal-like pattern at the nanometre scale, where compositions of Fe and Cr show strong anticorrelation and vary by as much as 20 at.%. The impressive plasticity is accommodated by the formation and operation of multiplanar, multicharacter dislocation slips, mediated by coherent interfaces, and controlled shear bandings. The excellent strength-ductility combination is thus enabled by a range of distinctive strengthening mechanisms, rendering the new alloy a potential candidate for safety critical, load-bearing structural applications.

In the sixth chapter, the effect of deformation on hierarchical compositional fluctuations is investigated. As plastic strain increases, the alloy is able to prolong its ductility via a lattice strain relaxation mechanism. This phenomenon is rationalised in terms of the dislocation behaviour exhibited during glide plane softening.

In the last chapter, major conclusions are drawn from this research. Some possible future work is proposed as extensions of what has been achieved.

Declaration

I certify that this work contains no material which has been accepted for the award of any other degree or diploma in my name in any university or other tertiary institution and, to the best of my knowledge and belief, contains no material previously published or written by another person, except where due reference has been made in the text. In addition, I certify that no part of this work will, in the future, be used in a submission in my name for any other degree or diploma in any university or other tertiary institution without the prior approval of the University of Adelaide and where applicable, any partner institution responsible for the joint award of this degree.

The author acknowledges that copyright of published works contained within this thesis resides with the copyright holder(s) of those works.

I give permission for the digital version of my thesis to be made available on the web, via the University's digital research repository, the Library Search and also through web search engines, unless permission has been granted by the University to restrict access for a period of time.

I acknowledge the support I have received for my research through the provision of an Australian Government Research Training Program Scholarship.

Name: … ....

Signature: .. ……………… Date: 11/03/22

Supervisor Declaration

I declare that I have read the contents of this report and provided feedback to the student based on the context contained herein.

Name: Zonghan Xie

Signature: ....   Date: 11/03/22

Name: Yujie Chen

Signature: .   ...   Date: 11/03/22

Acknowledgements

First and foremost, I would like to thank my mum and dad for their constant and immeasurable support. They worked hard and made many sacrifices to ensure I received the best education and opportunities to grow and develop into the person I am today. Their support extended beyond adolescence and into my adulthood while I completed my undergraduate, honours, and postgraduate degrees. Home cooked meals and a place to sleep have always been welcome constants in my life. I would not be where I am today without their continued support over the years, and this journey would not have been possible without them. I would also like to thank my brother, Jonathon, for his support and company over the many years. Finally, I would like to thank my grandfather, παππού Σίμο, and the rest of my extended family and family friends.

I extend my deepest gratitude to my supervisors Zonghan Xie and Yujie Chen. Zonghan cultivated my interest in materials science first via a summer research project, and subsequently by employing me as a tutor for Materials-based subjects every year since 2014. He believed in me right from the beginning and taught me everything I know about how to write papers and proposals and effectively present data, and was always able to put my work into context within the broader world of materials science. Thank you for reminding me that "nothing is wasted in the long march", and encouraging me to take additional opportunities and prioritise good research outcomes over increasing my publication count. A delayed paper is eventually good, but a rushed paper is forever bad. Yujie's expertise (theoretical and experimental) constantly proved invaluable and equipped me with most of the advanced characterisation skills I have today. She was frequently able to correct and hone my skills in this field, and came to my rescue every time my discussion was missing that one critical paragraph, and in correcting my interpretations and analyses of experimental data.

crystallography, data collection, and sample preparation; "good research starts and ends with good sample preparation."

A heartfelt thank you goes to my friends Alexis, Alan, Ashleigh, Gemma, Hannah, Jesse, John, Kate, Luke, James, Robin, Stephen, et al. for keeping me sane during my leisure time, including the countless board game and video game sessions, dinners, camping trips, and general hangs over the years. Making the jump from honours to postgrad was likely only possible due to the fact I was awarded my Bachelor's degree with First Class Honours. Thus, special mention is made to my group members and friends from my final year project; Gerard, Jamie, Andy, and Mark. I would also like to thank Huxley for being a good friend, gym buddy, and for his help with processing XRD data.

I very much appreciate my fellow colleagues for their company, joining me for the Friday "Winedowns" (thank you to Anthony Zander for funding those!), encouraging me to exercise more whether it be via bouldering, hiking, the corporate cup or gym, and our numerous weekend getaways at the Shack or camping trips. At the risk of forgetting someone, I am grateful to Ben, Erwin, Elliott, Matthew, Mathu, Ngan, Shaun, Thijs, Vidler, Xiaopeng (Gavin), and Yuecheng (Lenore). In the earlier days, Muna was a constant source of advice and guidance, and I will never forget the comic relief provided by Isaac and Sunly in our wonderful office, S324a.

Undertaking a PhD has affirmed the importance of a healthy work-life balance. I would therefore like to thank The University of Adelaide Volleyball Club, the Henley Hawks Volleyball Club, the Quicksand Beach Volleyball Community, the Adelaide University Snow Ski Club, and the UniSA Shodokan Aikido Club and its members with whom I trained with, and/or were responsible for organising and running club activities.

Finally, a big thank you to anyone who decides to actually take the time to read this thesis. I hope it's not too painful.

Papers Included in this Thesis-by-Publication

This thesis-by-publication consists of a combination of published journal articles and one journal article submitted for publication in accordance with the Academic Program Rules of The University of Adelaide. A complete list of articles authored by the candidate is presented here.

Publications #1 and #3 are reproduced in accordance with Elsevier's policy; authors can include their articles in full or in part in a thesis or dissertation for non-commercial purposes. Publication #2 is reproduced in accordance with the policies stipulated by the Royal Society of Chemistry. Publication #4 has been submitted to a journal, and therefore the officially published version will contain some minor differences.

Published Works

1. S. J. Tsianikas, Y. Chen, and Z. Xie (2020). "Deciphering deformation mechanisms of hierarchical dual-phase CrCoNi coatings." Journal of Materials Science & Technology **39**: 7-13.

2. S. J. Tsianikas, Y. Chen, J. Jeong, S. Zhang, Z. Xie (2021). "Self-toughened body-centred cubic structured high entropy alloy", Nanoscale 13 (6), 3602-3612.

3. S. J. Tsianikas, Y. Chen, J. Jeong, S. Zhang, Z. Xie (2022). "Forging strength-ductility unity in a high entropy steel", Journal of Materials Science & Technology 113, 158-165.

Works Submitted for Publication

4. S. J. Tsianikas, Y. Chen, Z. Xie (2022). "Adaptive attenuation of hierarchical composition fluctuations extends the plasticity of a high entropy steel".

Additional Works Related to this Thesis

Conference Proceedings

The following conference presentations are of close relevance to the main research topic, but are not included as part of this thesis:

1. S. J. Tsianikas, Y. Chen, Z. Xie (2018). Mechanically Robust Medium Entropy Alloy Coating for Surface Protection, Digital Poster, 19th International Microscopy Congress, Sydney, Australia.

2. S. J. Tsianikas, Y. Chen, J. Jeong, S. Zhang, Z. Xie (2020). High Entropy Alloy Displays Unique Strengthening and Deformation Pathways, 2020 virtual Materials Research Society - Spring/Fall Symposium.

Grants and Additional Scholarships

1. Hans-Jürgen and Marianne Ohff Research Grant (2019). Awarded to Simon Tsianikas to complete a six-month research internship at the Max-Planck-Institut für Eisenforschung.

2. Frank Perry Travelling Scholarship in Engineering (2020). Awarded to Simon Tsianikas to present work at the virtual Materials Research Society (MRS) – Spring/Fall Symposium.

Nomenclature

List of Acronyms

APT – Atom Probe Tomography

ARB – Accumulative Roll Bonding

BCC – Body-Centred Cubic

BF – Bright Field

CCA – Compositionally Complex Alloy

DCFI – Drift Corrected Frame Integration

DM – Diffraction Mapping

EBSD – Electron Backscatter Diffraction

ECAP – Equal Channel Angular Pressing

EDS / EDX – Energy Dispersive X-Ray Spectroscopy

EELS – Electron Energy Loss Spectroscopy

FCC – Face-Centred Cubic

FFT – Fast Fourier Transform

FIB – Focused Ion Beam

GB – Grain Boundary

GBSE – Grain Boundary Segregation Engineering

GPA – Geometric Phase Analysis

HAADF – High-Angle Annular Dark Field

HCP – Hexagonal Close-Packed

HEA – High Entropy Alloy

HES – High Entropy Steel

HPT – High-Pressure Torsion

HR – High Resolution

IMC – International Microscopy Congress

LCO – Local Chemical Order

MCA – Multiple- or Multi- Component Alloys

MEA – Medium Entropy Alloy

MPIE – Max-Planck-Institut für Eisenforschung

MPEA – Multi-Principal Element Alloy

MRS – Materials Research Symposium

NSD – Nanoscale Segment Detrapping

OIM – Orientation Image Microscopy

PED – Precession Electron Diffraction

SAED – Selected Area Electron Diffraction

SEM – Scanning Electron Microscopy

SFE – Stacking Fault Energy

SPD – Severe Plastic Deformation

SRO – Short-Range Order

STEM – Scanning Transmission Electron Microscopy

TEM – Transmission Electron Microscopy

TKD – Transmission Kikuchi Diffraction

TRIP – TRansformation Induced Plasticity

TWIP – TWinning Induced Plasticity

UCS – Ultimate Compressive Strength

UTS – Ultimate Tensile Strength

XRD – X-Ray Diffraction

List of Symbols

Symbol	Term	Base Units
k_y	Strengthening Coefficient	Pa m$^{0.5}$
d	Grain size	m
R_a	Roughness Value or Surface Roughness	m
σ	Engineering Stress	Pa
σ_Y	Yield Stress	Pa
σ_{UTS}	Ultimate Tensile Strength	Pa
σ_T	True Stress	Pa
σ_0	Friction Stress	Pa
E	Young's Modulus	Pa
F or P	Force or Load	N
P_{max}	Peak Indentation Load	N
A_0	Original Cross-Sectional Area	m^2
A_i	Instantaneous Cross-Sectional Area	m^2
A_p	Final Cross-Sectional Area	m^2
l_0	Initial Length	m
l_i	Instantaneous Length	m
l_p	Final Length	m
l_f	Fracture Length	m

u	Displacement	m
u_{el}	Elastic Component of Displacement	m
u_p	Plastic Component of Displacement	m
ε	Engineering Strain	-
ε_e	Elastic Component of Strain	-
ε_p	Plastic Component of Strain	-
ε_t	Total True Strain	-
ε_T	True Strain	-
ν	Poisson's Ratio	-
ν_i, E_i	Indenter Parameters	-
$\%EL$	Ductility	%
E_r	Reduced Modulus	Pa
H	Hardness	Pa
$S = \frac{dP}{dh}$	Initial Unloading Stiffness	Pa m$^{0.5}$
h_f	Contact Depth	m
h	Indenter Displacement	m
d_{hkl}	Interplanar spacing of Miller indices (h, k, l)	m
λ	X-Ray Diffractometer Wavelength	m
θ	Angle of Incident Wavelength	°
n	Order of Reflection (1, 2, 3, …)	-

a	Lattice Parameter	m
a_{BCC}	Lattice Parameter for a BCC crystal	m
a_{FCC}	Lattice Parameter for an FCC crystal	m
a_{HCP}	Lattice Parameter (basal) for an HCP crystal	m
c	Height (i.e. non-basal length) of the HCP unit cell	m
R	Atomic Radius	m
x_i	Observed Value	-
$\bar{x}$	Mean Value	-

Chapter 1

Introduction

In this chapter, a brief introduction of the research area is provided and the motivation behind the thesis topic is discussed. A broad literature review introduces terms and concepts that will be applied in the methodology and journal articles that follow. Although this chapter aims to provide the necessary background relevant to the theoretical development in the subsequent chapters of this thesis, it is assumed that the reader is familiar with the subject of materials science. For a comprehensive treatment of this subject, the reader is referred elsewhere [1]. Finally, the overall aims and specific objectives for this thesis are outlined.

1.1 Metallic Alloys

Metallic alloys are crucial to everyday life and represent a large area of research in the field of materials science. Very rarely is it possible for a pure metal to yield the most desirable qualities required for an application. Typically, conventional alloys are a binary mixture or contain one primary element with low quantities of other alloying elements [2]. However, by adding multiple principal elements to an alloy's composition,

it is possible to obtain different types of alloys. The proceeding subsections will examine different types of compositionally complex alloys (CCAs) in further detail.

1.1.1 High- and Medium- Entropy Alloys

For thousands of years, traditional solute-solvent design philosophy has been the basis for the development of alloy systems. Following a series of innovations, High Entropy Alloys (HEAs) have become a significant field of research beginning with the independent works of Cantor et al. [3] and Yeh et al. [4] in the mid-2000s. These alloys possess novel and advantageous properties that traditional alloys do not, such as high thermal stability, wear resistance, oxidation resistance, electric resistivity, and corrosion resistance [5].

The term was originally coined because it was posited that the formation of random solid solutions can prevail over intermetallic compounds primarily due to the high configurational entropy of mixing in comparison to traditional alloys. One of the earliest definitions specified that the alloy had to consist of a single solid solution, and contain at least five principal elements in an equiatomic or near equiatomic concentration (between 5% and 35%) [4]. The expression used to determine if a solid solution or an intermetallic compound will form is given in equation 1.1;

$$\Delta G_{mix} = \Delta H_{mix} - T\Delta S_{mix} \hspace{2cm} 1.1$$

where G_{mix} is the Gibbs free energy of mixing, T is the absolute temperature, ΔH_{mix} is the enthalpy of mixing and S_{mix} is configurational molar entropy of mixing in an ideal solid solution [5]. If ΔH_{mix} is smaller than $T\Delta S_{mix}$, then the formation of a disordered solid solution is favoured. The configurational entropy of mixing for a random solid solution with N components is defined per equation 1.2; The mixing configurational entropy of an equimolar compound with N elements can be calculated according to Boltzmann's hypothesis (equation 1.2);

$$\Delta S_{mix} = -R \sum_{i} c_i ln c_i \qquad\qquad 1.2$$

where R is the gas constant (8.314 J/K mol), and c_i is the molar content of the ith component. If the alloy has an equiatomic composition, the configurational entropy of mixing reaches its maximum (equation 1.3);

$$\Delta S_{mix} = -R ln N \qquad\qquad 1.3$$

The entropy-based definition specifies thresholds for low (< 0.69R), medium (0.7R < x < 1.60R) and high (> 1.61R) entropy alloys. A pure element thus has a mixing entropy of zero, whereas an alloy with five elements has a mixing entropy of 1.61 J/K·mol. Five elements are designated as the minimum number of elements required to counterbalance the mixing enthalpy in most alloy systems [6, 7], and an alloy with three or four elements is termed a Medium Entropy Alloy (MEA). This is not without issues however, as even some binary metallic alloys do not have random atomic positions [6]. Some other definitions require HEAs to be strictly equimolar, use different classification thresholds (> 1.5R) or impose the requirement that the microstructure must be one single phase [6]. Due to conceptual challenges of the entropy-based definition, these design rules were later relaxed [8]. Ultimately there is no right or wrong answer, and the intent of the work will determine the appropriate approach [6]. It is the types of elements used and the processing techniques, and not just the sheer quantity of elements or level of mixing entropy, that are the important factors in alloy design.

HEAs are reported to have four core effects: high entropy, lattice distortion, sluggish diffusion and cocktail effects [7]. The high entropy effect is somewhat qualitative with a broad classification of high, medium or low taking into account the phase, number of elements, and compositions. Each element in a HEA has the same possibility to occupy a lattice site, and as every element has differing atomic radii, this leads to the lattice distortion effect [5]. This effect is said to contribute to excess configurational

entropy, increased hardness, reduced electrical and thermal conductivity and reduced temperature dependence of these properties [6]. Sluggish diffusion is proposed to arise from the formation of nanocrystals and amorphous phases on solidification, and is based on microstructural stability observations. This hypothesis is challenged by Miracle and Senkov [6], as measuring diffusion coefficients accurately is challenging when there is compositional complexity and has only been addressed in one study, meaning a wider dataset is required. Finally, the cocktail effect refers to unexpected and desirable properties resulting from synergising constituent parts, which are not obtainable from any sole element [5]. A practical example of the cocktail effect is the combination of high strength and ductility simultaneously which are otherwise often mutually exclusive [6].

MEAs are typically comprised of three or four principal elements. After the initial intense research focus on HEAs, some of this attention later shifted to MEAs [9-12]. While superior performance of HEAs is attributed to high configurational entropy, Yoshida et al. [12] have shown that ternary CrCoNi outperforms quinary CoCrFeMnNi in strength-ductility trade-off and fracture toughness despite having a lower configurational entropy. CrCoNi has also been determined to be significantly stronger than MnFeNi [10] despite the fact that they have equal configurational entropy. The reason for the advanced properties of CrCoNi (viz. hardness, ductility, toughness and yield strength) compared to quinary alloy CrMnFeCoNi is owed to nanotwinning being a prominent deformation mechanism in this MEA [10]. This mechanism is reached relatively early to provide high and steady work hardening, which supresses plastic instability from pronounced dislocation activity. Due to this feature, CrCoNi is championed as a material which can defeat the ubiquitous strength-ductility trade-off, with a tensile strength of 1 GPa at room temperature, a failure strain of 70%, and a fracture toughness above 200 MPa·m$^{0.5}$, and superior performance at cryogenic temperatures

[9]. Zhang et al. [13] also attributes negative stacking fault energy at 0 K leading to high propensity for twinning for these properties, adding that although twins usually impede dislocation motion and induce strengthening, multiple twinning systems, referred to as twinning induced plasticity (TWIP) [14], can improve the ductility. Lastly, CrCoNi has been shown to exhibit a new, two-step FCC → HCP → FCC (twinned) phase transformation [15], which has not been otherwise observed in studies of bulk CrCoNi due to a lack of atomistically detailed characterisation, and/or lack of suitable stresses to overcome dual-phase transformation barriers.

Other modifications to this alloy design strategy can also be made, which venture further outside of HEA and MEA fundamentals. The addition of interstitial elements results in the formation of an interstitial HEA (iHEA) [16], and an HEA with a very high iron content is referred to as a high entropy steel (HES) [17]. Other terms can be used to refer broadly to all of the aforementioned alloys at once, without the risk of violating definitions. Typically, multiple principal element alloys (MPEAs), multiple- or multi-component alloys (MCA), and compositionally complex alloys (CCAs) have been used. These terms encapsulate the key concepts of HEAs and maintain the general principle of having multiple elements present in high concentrations, while relaxing some of the strict rules in defining HEAs.

1.1.2 Interstitial High Entropy Alloys

The strategy of creating new and unique alloys by modifying the bulk composition of alloys can be further expanded through the addition of interstitial elements. Typical elements added include carbon [16], oxygen [18], boron [19, 20], and nitrogen [21]. Grain boundary characteristics, interstitial strengthening, and consequently mechanical response can be adjusted through solute decoration of grain boundaries achieved via grain boundary segregation engineering (GBSE) [22], driven by the Gibbsian reduction in grain boundary energy [20]. In one application, the addition of

carbon to a FeMnCoCr-based alloy resulted in a unification of TWIP and TRIP effects to improve its strain hardening capacity [16]. Boron has also been added to a FeMnCoCr-based alloy, driving grain refinement, and enhancing the bonding strength of grain boundaries [20]. Meanwhile, oxygen has been added to a refractory TiZrHfNb HEA, resulting in the formation of O-Zr-Ti-rich complexes capable of pinning dislocations and promoting cross-slip, resulting in an increase in the tensile strength by 48% and tensile ductility by 95% [18]. If the host lattice is highly distorted, multiple interstitial elements in high concentrations (> 2 at.%) can be introduced, such as the addition of C, N, and O into an equiatomic TiNbZr alloy, to achieve massive solid solution strengthening [23]. Interstitial strengthening is a cost-effective way to strengthen a material, as it is more efficient to alloy grain boundaries only instead of the entire bulk, and elements such as carbon, boron, oxygen, and nitrogen are relatively inexpensive and abundant, and therefore cheaper to use than alloying the bulk with expensive elements [20].

1.1.3 Spinodal High Entropy Alloys

Phase decomposition, as opposed to phase separation, has also been considered undesirable in the quest to achieve single phase solid solutions in HEA design. Akin to the design of new CCAs, attention has also progressively shifted toward exploiting, rather than evading, phase metastability, with one of the key benefits being the multiphase interface that results [24]. This could manifest as a formation of low-misfit coherent nanoprecipitates in an alloy matrix (e.g. isotropic Ni_3Al-type $L1_2$ particle strengthening within an FCC phase [25]), or more simply the decomposition of one structure into two (or more) regions of the same crystal structure with disparate lattice parameters and therefore elastic strain distribution (e.g. NbTi-rich β and HfV-rich β^* BCC regions in a HfNbTiV alloy [26]), creating a rugged terrain for the passage of dislocations.

1.1.4 High Entropy Steels

A compositionally complex iron-based alloy can be defined as a high entropy steel [17]. Optimum alloy design lies not in maximisation of entropy, but rather the avoidance of the formation of brittle intermetallic phases. For example, the non-equiatomic $Fe_{40}Cr_{30}Mn_{10}Co_{10}$ alloy is homogenous single-phase FCC, whereas the equiatomic FeMnCoCr has a complex multiphase microstructure [27]. A non-equiatomic mixing rule provides a larger compositional space for developing HEAs without intermetallic phases. Thus, systems based on a solid solution matrix rich in Fe provide a large compositional space, and are a good starting point for blending further components in [17]. While magnesium and aluminium alloys, carbon fibre composites, and other related materials are lightweight, they do not provide the same unique combination of absolute strength, specific strength, ductility, toughness, and cost-effectiveness as steel [17]. Thus, further innovations in steel microstructure physics and alloy design remains an important endeavour.

1.1.5 Alloy Preparation

CCAs can be prepared using a myriad of techniques, such as casting, and powder metallurgy. When more than five elements are involved, there are challenges associated with conventional ingot metallurgy processing methods [28]. Further, synthesising and testing the performance of materials one-by-one is an inefficient approach in the exploration of new materials. A faster and cheaper alternative is synthesis via deposition, such as magnetron sputtering or laser cladding [29]. Laser cladding allows strong metallurgical interfaces to be formed between the layer and matrix, however, crack and pore formation is a common issue [29]. Sputter deposition provides excellent control over stoichiometry, and yields very unique microstructures which would otherwise require complicated mechanical processing techniques to

induce severe plastic deformation (SPD), such as high-pressure torsion (HPT), equal channel angular pressing (ECAP), accumulative roll bonding (ARB), etc. [30]. Among the key deposition parameters for controlling the resultant microstructure are the applied voltage, distance between target and substrate, target composition, type of substrate, and deposition rate [31].

1.2 Strengthening Mechanisms

To obtain excellent mechanical properties, it is necessary to combine multiple strengthening and deformation mechanisms simultaneously. Important mechanisms relevant to this thesis and proceeding publications are elaborated in this subsection.

1.2.1 Enhanced Solid Solution Strengthening

Solid solution strengthening of alloys is a phenomenon whereby the lattice of a host metal is strained via the introduction of impurity atoms, consequently impeding dislocation motion and improving strength [1]. As mentioned in Section 1.1.2, in HEAs, and by extension in CCAs, the extent of lattice distortion is further heightened due to the higher number and concentration of alloying elements, as demonstrated in Figure 1. The lattice distortion can be enhanced further by selecting atoms with a larger lattice parameter mismatch compared to constituent species, e.g. VCoNi has higher lattice distortion than CrCoNi due to the dissimilar atomic radius of V [32]. Thus, the enhanced solid solution strengthening in CCAs leads to an improvement in the strength compared to traditional alloys.

Single element:
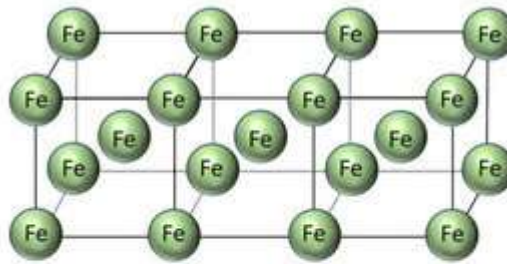
Conventional alloy:
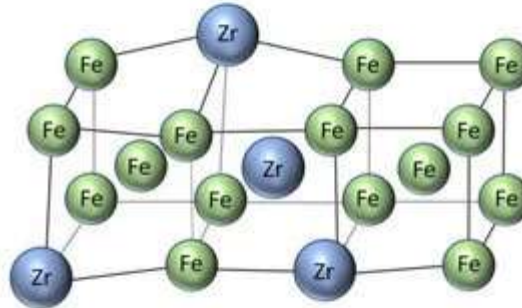
High-entropy alloy:
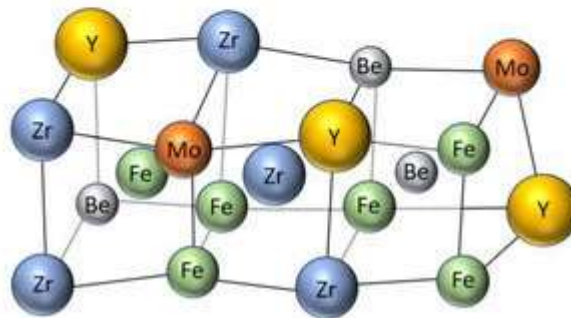
Figure 1: Depiction of the influence of alloying on lattice strain; (a) pure Ti, (b) Ti alloyed with Nb, and (c) a TiNbTaZrHf HEA. Reproduced with a license through RightsLink from [33].

1.2.2 Short Range Ordering

The close or regular arrangement of atomic pairs on length scales over a few atomic distances are said to exhibit Short Range Ordering (SRO). This phenomenon arises due to the occurrence of energetically favourable interactions between different types of atoms. For example, in the FCC VCoNi MEA, V-Co and V-Ni interactions are preferred, whereas V-V interactions are avoided [34]. It is distinctly different to structures resulting from spinodal decomposition, or compositional undulations via the rendering of SFE [35]. BCC CCAs and their derivatives in particular have different

deformation behaviour compared to conventional BCC metals and alloys due to SRO. Deformation in BCC alloys is controlled by screw dislocation glide [36], but due to the 'rugged terrain' present due to the chemical complexity [37, 38], edge dislocations are also present during deformation [39]. Ergo, screw dominated dislocation is no longer the governing process controlling strength; rather, edge dislocations are slowed down to glide with a similar speed to screw dislocations [39, 40]. The numerous short-distance obstacles created by the SRO structure trip and trap gliding dislocations (i.e. stick-slip dislocation motion). The resulting nanoscale segment detrapping (NSD) mechanism induces a barrier governing dislocation mobility, where it becomes more energetically unfavourable to dislodge a trapped dislocation segment in a favourable position [41]. After detrapping from its local SRO environment, a curved area corresponding to a particular NSD is formed. Dislocation movement controls the strength of an alloy, and therefore this effect is of high significance; SRO has been attributed to the increase of yield strength by 25% in a CrCoNi alloy [42].

1.2.3 Twinning Induced Plasticity

Deformation by slip or by twinning is a critical factor in a material's deformation behaviour. Twinning leads to relatively small bulk plastic deformation compared to that resulting from slip [1], in a process referred to as Twinning Induced Plasticity (TWIP). It can also provide high and steady work hardening, and supress plastic instability from pronounced dislocation activity [10]. Plastic deformation of FCC metals under certain conditions can result in deformation twinning, and the formation of twin/matrix lamellae [43]. As mentioned in Section 1.1.1, in CrCoNi, nanotwinning is achieved through its negative stacking fault energy, which leads to a high propensity for twinning, leading to superior performance at cryogenic temperatures [9].

1.2.4 Controlled Shear Banding
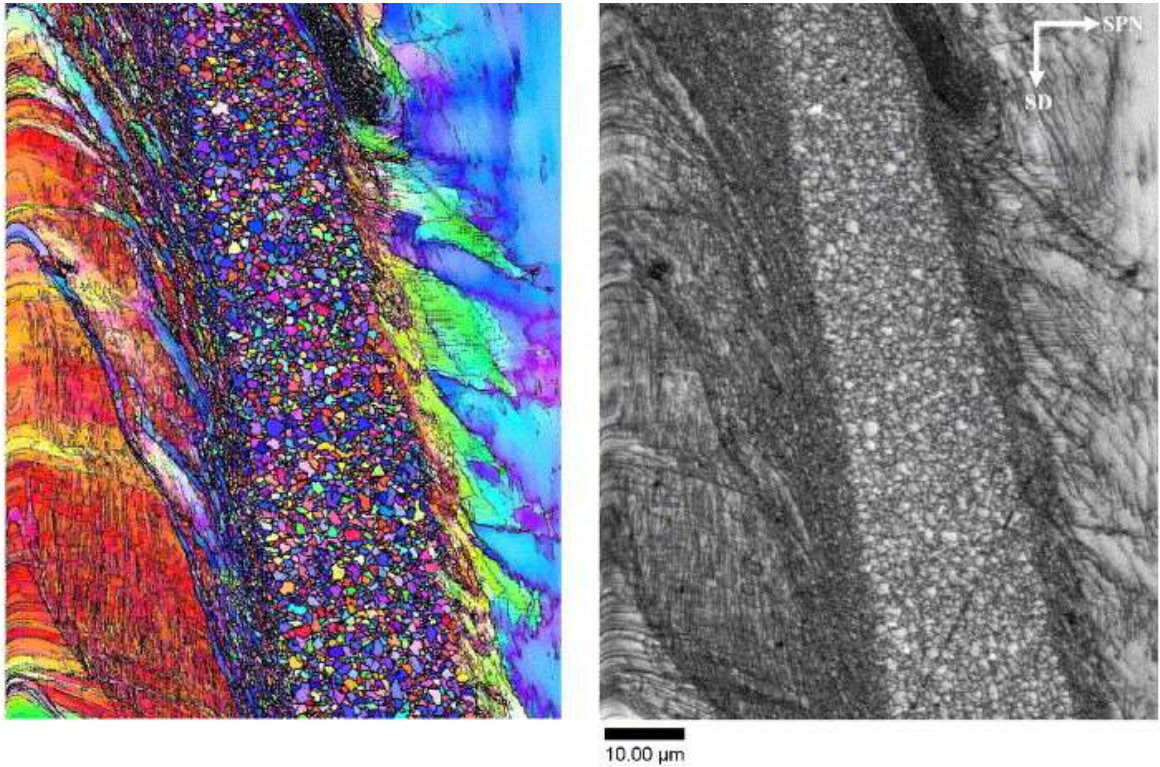
Figure 2: OIM and corresponding image quality map of a shear band in an interstitial free steel. Reproduced with a license through RightsLink from [44].

Also referred to as strain localisations, shear bands are narrow zones of intense shearing strain and collective dislocation activity, developed during severe deformation of metals and alloys during intense dynamic loading [44]. Shear banding typically occurs when other deformation mechanisms have been exhausted, such as when homogenous dislocation slip is inhibited, or when there is an insufficient number of crystallographic slip systems. It is a softening mechanism, often manifested by a sudden drop in local flow stress, with a high extent of deformation exhibited inside the shear band [45]. In such cases this mechanism acts as an alternative deformation mode, which could circumvent catastrophic failure. An example of shear banding is depicted in Figure 2.

1.2.5 Transformation Induced Plasticity in Dual-Phase Alloys
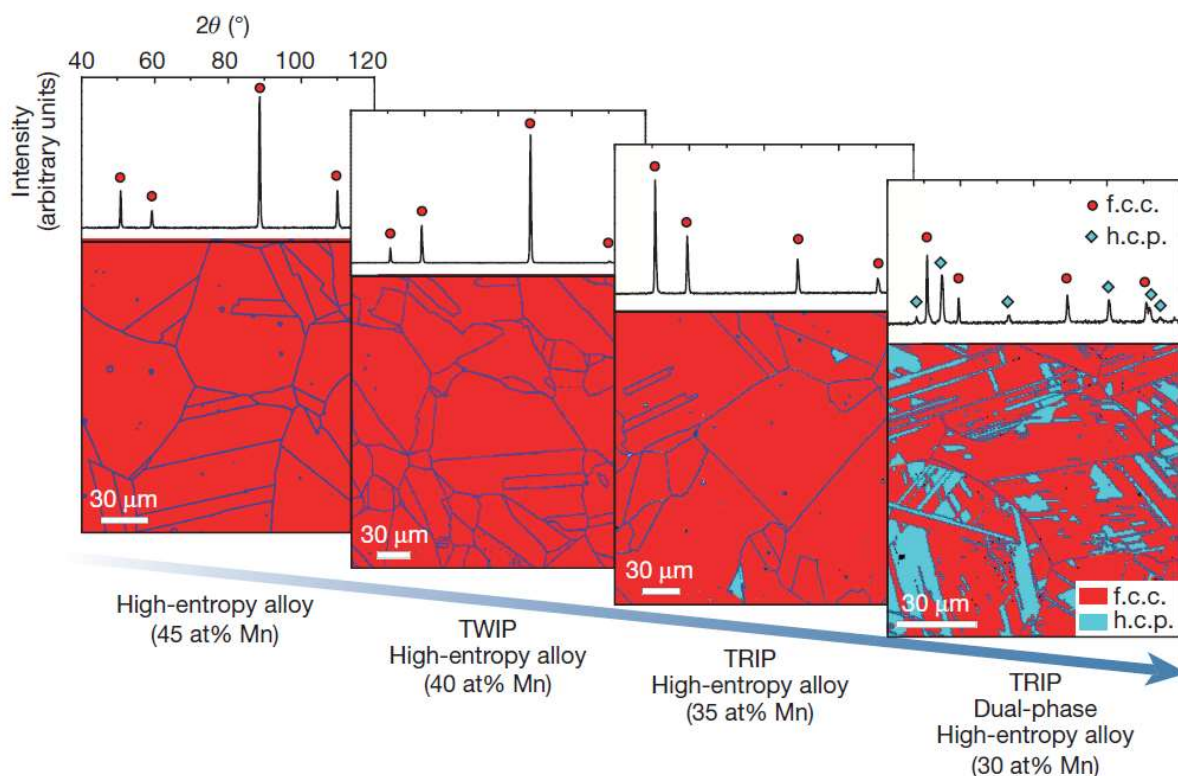
Figure 3: XRD patterns and EBSD phase maps of $Fe_{80-x}Mn_xCo_{10}Cr_{10}$ HEAs. The Mn content plays a vital role in tuning innate phase stability. Reproduced with a license through RightsLink from [46].

HEAs originally aimed to create a single solid solution, as phase separation would cause the formation of brittle intermetallic compounds [47]. After the design and evaluation of a dual-phase FeMnCoCr alloy with dual phase FCC and HCP structures, this design restriction was relaxed [48]. The micro-composite effect can impede dislocation motion, resulting in improved strength [49]. Meanwhile, mechanical properties can be further tweaked by changing the fraction of each phase, accomplished via tailoring the stacking fault energy [46]. An example of this is shown in Figure 3, where the phase stability is tailored via the Mn content. This thermodynamic metastability can also lead to phase transformations upon deformation. Phase metastability improves the strength of an alloy by increasing phase boundary area, and by allowing phase transformations to occur during deformation [50]. This is termed TRansformation Induced Plasticity (TRIP), which combines interface hardening with transformation induced hardening, improving strength and

ductility simultaneously [51]. An example of this is shown in Figure 4 in a phase analysis of the deformed microstructure of a $Co_{20}Cr_{20}Fe_{34}Mn_{20}Ni_6$ alloy.
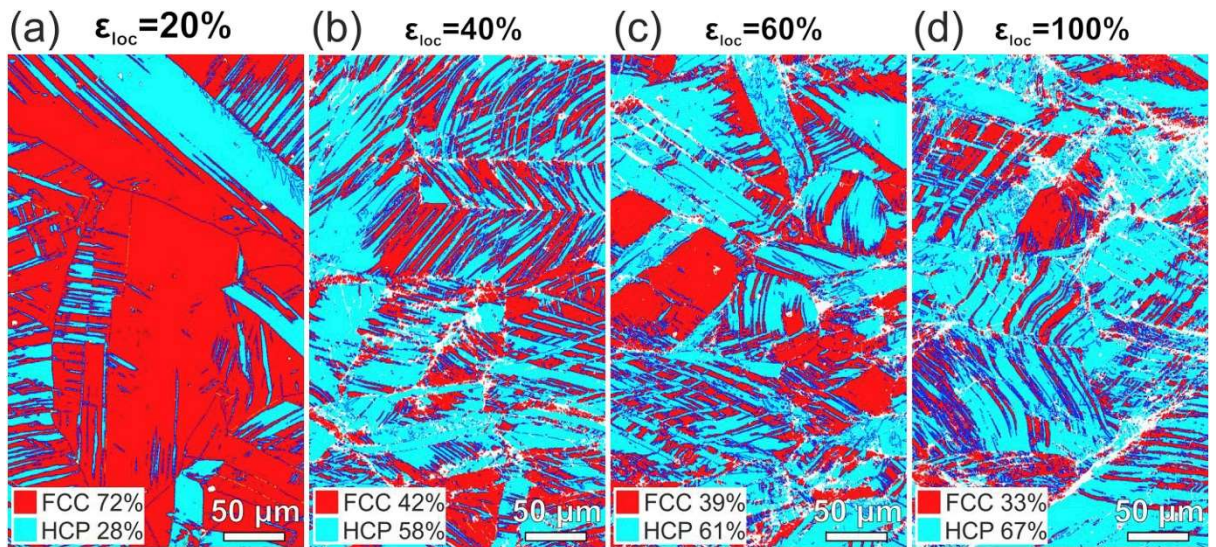
Figure 4: EBSD phase maps of $Co_{20}Cr_{20}Fe_{34}Mn_{20}Ni_6$ with HCP fraction increasing with increasing tensile deformation from (a) to (d). Reproduced with a license through RightsLink from [52].

Bi-directional TRIP, where dynamic forward and reverse phase transformations occur, is also a possibility. In the case of a dual-phase FCC and HCP alloy, this was enabled through a near-zero yet positive SFE, with other factors such as local dissipative heating, local stress fields, lattice defects acting as pinning points for dissociated partials, and SF partitioning effects, influencing the reaction either towards FCC or HCP phases [53]. Whereas a high SFE in an FCC structure would lead to deformation twinning and planar dislocation patterns, the low SFE results in near-identical stability of FCC and HCP phases [53]. The continued reactions lead to the formation and refinement of hierarchical nanolaminate structures, providing extensive work hardening capacity and thus improving strength, without sacrificing ductility.

1.2.6 Grain Refinement

The strength of a material is related to the moveability of its dislocations. When the grain size becomes smaller, there are more barriers for the passage of dislocations. Thus, strength increases during grain refinement [1]. Materials with grains in the nanometre range are called nanocrystalline materials, and exhibit outstanding yield

stress, high hardness, and good fatigue resistance [54]. Grain size, *d*, and yield strength, σ_Y, can be related using the Hall-Petch equation;

$$\sigma_Y = \sigma_0 + \frac{k_y}{\sqrt{d}} \qquad\qquad 1.4$$

Where k_y is the strengthening coefficient, and σ_0 is a constant related to the frictional stress resisting the motion of gliding dislocations or the internal back stress. This expression demonstrates the inverse relationship that the yield stress and grain size have.

1.3 Research Gaps

The field of CCAs and their derivatives is vast, and the number of yearly publications about HEAs alone continues to grow exponentially [55]. While HEAs are a primary area of research which continuously push the strength-ductility frontier, other types of CCAs warrant examination, such as MEAs, iHEAs, metastable CCAs, and HESs. In addition, for the purposes of this thesis, the following four gaps in the literature are highlighted.

- The CrCoNi alloy exhibits excellent properties, and worthy of further investigation are the roles of TRIP, grain refinement, and shear banding in its marked plastic response.

- While iHEAs are examined frequently, it is rare for multiple interstitial elements to be added at once. Thus, an examination of the effect of adding multiple interstitial elements on alloy metastability, and unification of multiple strengthening mechanisms, such as interstitial strengthening, grain boundary segregation engineering, TRIP, and TWIP effects, is warranted.

- Aside from single-phase or multi-phase alloys, CCAs with a compositional gradient or spinodal-like structure also demonstrate unique deformation behaviour due to their high density of coherent interfaces and the uneven terrain

traversed by dislocations. The resulting multiplanar, multicharacter dislocation slip behaviour requires further examination.

- In addition to spinodal structures, recent investigations have uncovered the important role that SRO plays in strengthening materials. Despite this advance, it is unclear what happens to these compositional fluctuations when the respective alloys are subject to deformation.

1.4 Aim and Objectives

The overall aim of this project is to examine and integrate multiple deformation mechanisms in CCAs, which will lead to improved understanding for the design of mechanically robust CCAs. The thesis spans four academic articles, which form the basis for the aims and objectives in this project. In order to conduct materials characterisation, Focussed Ion Beam (FIB) milling, Transmission Electron Microscopy (TEM), High Resolution (HR) Scanning Transmission Electron Microscopy (STEM), and various nanomechanical testing techniques are applied. The specific objectives are:

1. Examine innate and resultant defects, and the crystal structures of undeformed and post-mortem equiatomic ternary MEA CrCoNi. Characterise the deformation mechanisms of CrCoNi, paying particular attention to changes in planar defects, shear banding, phase transformation, and grain refinement. This will be achieved via nanoindentation and HR STEM techniques with particular focus on structural characterisation of undeformed and post-mortem samples.

2. Analyse the deformation mechanisms of a BCC-structured $Fe_{51.2}Mn_{24.3}Co_{11.9}Cr_{10.1}B_{1.4}O_{0.3}C_{0.3}$ iHEA alloy. Examine the influence of doping with not just one, but three interstitial elements (B, C, O) on mechanical

properties. Evaluate and quantify the evolution of deformation induced phase transformations. Determine the influence of GBSE on alloy mechanical properties, and examine the distribution of segregation. This study adds Atom Probe Tomography (APT) and Precession Electron Diffraction (PED) mapping to the arsenal of experimental characterisation tools, which can probe the material in three dimensions, and quantify phase fractions, respectively.

3. Evaluate the strengthening mechanisms in a $Fe_{72.4}Co_{13.9}Cr_{10.4}Mn_{2.7}B_{0.34}$ BCC-structured high entropy steel exhibiting nanoscale spinodal-like fluctuations. The distribution of the fluctuations, and the extent of GBSE will be examined in detail in three dimensions with APT, and its role in alloy strengthening will be examined. The multicharacter, multiplanar dislocation behaviour of this BCC CCA will also be examined in further detail using HR STEM analysis techniques.

4. Investigate the effect that deformation has on chemical compositional fluctuations in a CCA over multiple length scales. The method of investigation will primarily involve strain mapping at the atomic scale, and Energy Dispersive X-Ray Spectroscopy (EDS) at the nanoscale of pre- and post- mortem samples. A detailed dynamic dislocation-based mechanism for this phenomenon will be proposed.

Chapter 2

Methodology

In this chapter, the methodology used to achieve the aims of the thesis are outlined. A brief summary of the techniques and their application for obtaining the results presented in the subsequent publications is provided. For a more comprehensive treatment of methodology background information, such as fundamentals of physics phenomena (e.g. electron wave/particle duality, interactions of electrons with matter, etc.), the reader is referred elsewhere [56].

2.1 Alloy Preparation

All sample synthesis is conducted at the Advanced Coatings Applied Research Laboratory (ACARL) at the Department of Mechanical and Biomedical Engineering (MBE) City University in Hong Kong by Dr Zhifeng Zhou. The coatings are deposited by closed field unbalanced magnetron sputtering ion plating (CFUMSIP) onto AISI M2 high speed steel substrates, using a UDP650 magnetron sputtering system (Teer Coatings Ltd, UK). The steel substrates are hardened to HRC 60, finely polished to R_a ~0.03 μm, degreased, ultrasonically cleaned, and subsequently blown dry in flowing

nitrogen gas. An alloy target (China Material Technology Co. Ltd) with dimensions of 345 mm x 145 mm x 5 mm is used for the deposition. The substrate is stationary during deposition, and the target-to-substrate distance is fixed at 170 mm. The substrate holder is biased with pulsed DC at a frequency of 250 kHz. The vacuum chamber is pumped down to a background pressure of < 2e-6 Torr by controlling the flow rate of Ar (50 sccm). The deposition process includes plasma ion cleaning (-450 V bias, 30 min) prior to deposition. Ion etching of the steel substrate is used to remove the oxide layer on the substrate surface. No external heating is used during coating deposition. Further details on each particular synthesis are available in the respective publications.

2.2 Specimen Fabrication

Focussed ion beam (FIB) milling is a technique that can be used to prepare thin foil specimens for analysis in a Transmission Electron Microscope (TEM). The FIB comprises of a Scanning Electron Microscope (SEM), used for general imaging, in-tandem with an ion beam, used for milling, deposition, or welding. The ion beam is at 52 degrees to the SEM beam, and thus acquiring images using both beams provides depth perception to a traditionally 2D technique. Prior to TEM sample preparation, platinum is deposited on the surface to protect the sample from damage during milling. The FIB assembly also includes a micromanipulator; an 'arm' which can be adjusted in three directions (retract/insert, up/down, and clockwise/anti-clockwise) which can be attached to the foil via platinum deposition, and can be used to "lift-out" a sample.
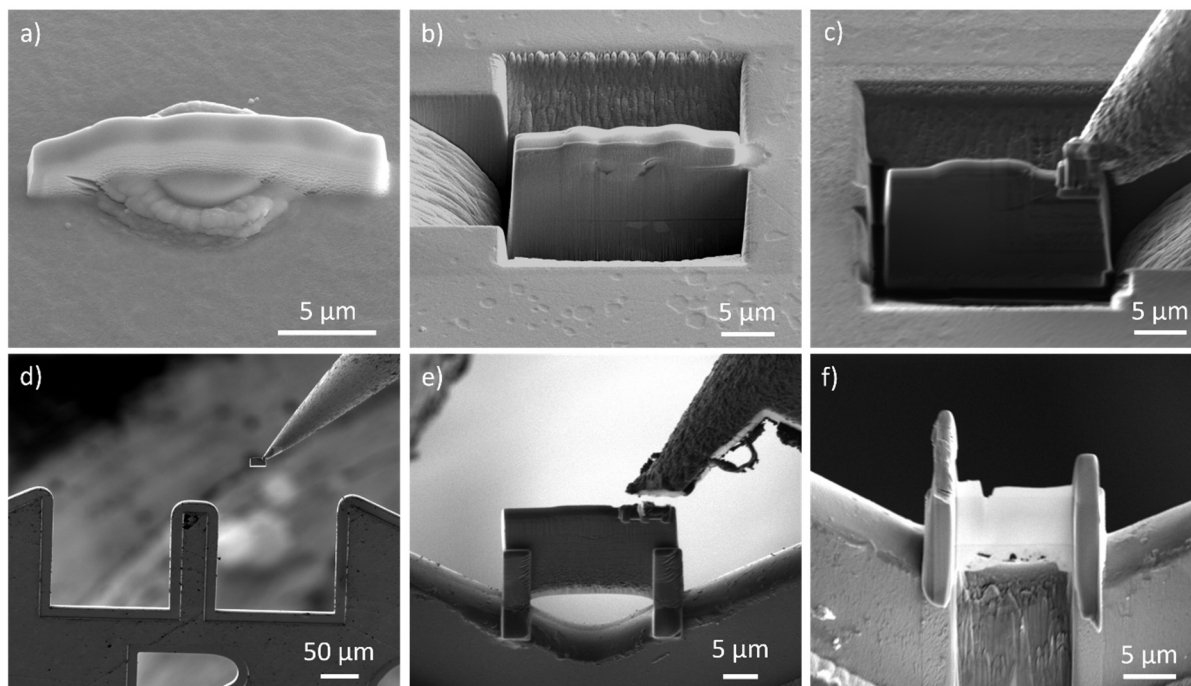
Figure 5: Lift-out method breakdown; (a) platinum deposition to protect the specimen during subsequent milling stages, (b) milling of three large regions around the indent, (c) attaching micromanipulator and milling remaining contact of foil with bulk sample (noting the 180° scan rotation), (d) transferring TEM sample to FIB grid, (e) welding sample to grid, with subsequent milling to sever connection between the foil and the micromanipulator, and (f) TEM sample that has achieved "electron transparency" after thinning via milling the front and back sides.

The lift-out is achieved by retracting the micromanipulator after dropping the stage post-milling. After mounting to a 'grid', the foil is thinned by the electron beam (with a progressively decreasing beam current, and a final low-kV "polishing" stage) until it becomes "electron transparent". This means that it is thin enough to transmit sufficient electrons such that enough intensity falls on a screen or film to yield an interpretable image. Generally, the sample thickness should be in the vicinity of 50 nm. A breakdown of this process is shown in Figure 5. To improve foil quality further, the overall dimensions of the foil can be minimised (when only interested in a particular region of analysis, such as under the site of indentation). Minimising the amount of deposited platinum in order to reduce redeposition onto the foil, and milling from the bottom-up by increasing the tilt angles (e.g. from $52 \pm 1.5°$ to $52 \pm 3°$), are other strategies that can be used. For ultra-fine grained materials, some milling damage to the foil may be tolerable so as to obtain ultra-thin regions for analysis, making it possible to avoid grain overlap when subsequently imaging atomic columns.

The FIB can also be used to prepare tips for analysis via Atom Probe Tomography (APT) following the protocol depicted in Figure 6. First, a triangular prism is lifted out from the sample using the FIB's micromanipulator, and slices are cut and mounted on posts on a commercially available microtip array [57]. After this, the tips are 'sharpened' using an annular (donut-shaped) pattern with a progressively decreased diameter of inner annulus and beam current, making them suitable for analysis via APT.

The preparation of micropillars for compression is also carried out using the FIB. The fabrication procedure is similar to that of APT tip sharpening; annular patterns are constructed to mill the sample surface, ensuring enough clearance for the indenter is provided. The inner diameter and beam current are progressively reduced, such that a pillar with a desired diameter and aspect ratio, with minimum tapering, is obtained.
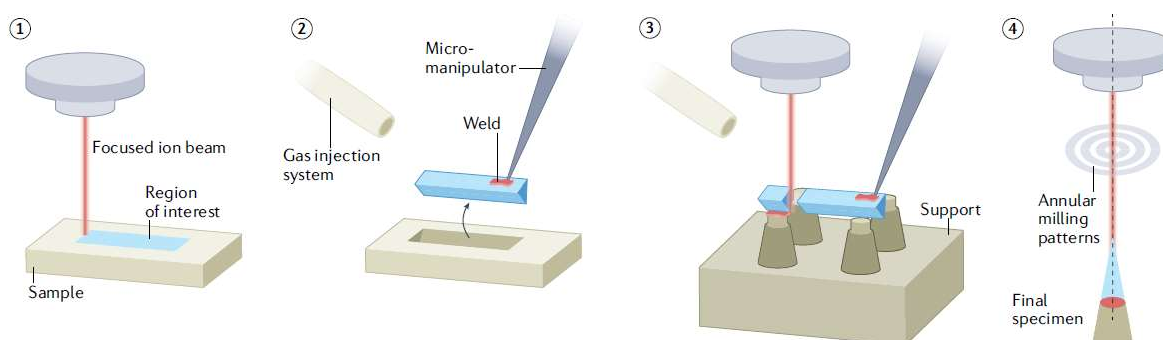
Figure 6: Four-step protocol for FIB lift-out specimen preparation for APT analysis. Reproduced with a license through RightsLink from [58].

2.3 Structural and Chemical Characterisation

2.3.1 X-Ray Diffraction

X-Ray Diffraction (XRD) can be used to investigate the crystal structure a material with a non-amorphous structure. An XRD spectrum is essentially a one-dimensional profile scan of a polycrystalline diffraction pattern. The advantage is that it can reveal the crystal structure(s) present in an alloy without having to use advanced characterisation techniques such as TEM, and their associated sample preparation techniques. If

examining coatings, the spectra are collected at a low incident angle (e.g. ~2°) to minimise any interference from the substrate. The interplanar spacing, d_{hkl}, at Miller indices (h, k, l), can be obtained via Equation 2.1, which relates d_{hkl} with the angle of diffraction, θ, the diffractometer wavelength, λ, and corresponding order of reflection, n, which takes integer values (1, 2, 3, …);

$$2d_{hkl}sin\theta = n\lambda \qquad\qquad 2.1$$

2.3.2 Scanning Electron Microscopy

Due to the limited image resolution in light microscopes, Scanning Electron Microscopy (SEM) uses secondary electrons to create images of samples at much smaller length scales. It is useful in applications requiring imaging at higher length scales than those warranted by TEM, such as imaging sample topography, or for preparing TEM foils in-conjunction with an ion beam. An SEM equipped with an Electron BackScatter Diffraction (EBSD) detector can also be used to obtain EBSD data from the sample directly (after polishing), from which useful and interpretable data such as phase maps, and inverse pole figures (which clearly depict grain orientations), can be generated [59]. The equivalent technique for use on a TEM foil (instead of bulk sample) is Transmission Kikuchi Diffraction (TKD) [60].

2.3.3 Transmission Electron Microscopy

A TEM uses transmitted electrons, rather than secondary electrons, to see nano- and atomic-scale features [56]. The transmitted electrons are projected onto a screen in order to see detailed structural information. It is also possible to use a TEM to detect a range of signals from which several kinds of spectra and diffraction patterns can be obtained [56]. Diffraction patterns are very important analytical tools which contain information on the crystal structure, lattice repeat distance, and specimen shape. A variation of this technique is Precession Electron Diffraction (PED), which offers a broad range of reflections, providing more information for phase determination

algorithms, and has a small probe size, which is useful for probing nanograins, among other advantages [61]. Other useful TEM-based techniques include Electron Energy Loss Spectroscopy (EELS) [62], which can be particularly useful for probing the composition of light elements. Scanning Transmission Electron Microscopy (STEM) is a type of TEM in which the beam is focussed to a fine spot, and rastered over the sample. If the foil is suitably thin and of good quality, STEM can be used to obtain high resolution images which show the arrangements of atomic columns, from which crystal structure can be inferred, and defects such as dislocations, grain boundaries, stacking faults and twinning, can be easily imaged. Fast Fourier Transforms (FFT) of STEM images can be obtained digitally, which can be used for crystal structure determination. If the material has a complicated nanostructure, FFTs can be obtained from different regions in the image(s) to determine the orientation relationship between possible phases.

2.3.4 Atom Probe Tomography

Atom probe tomography (APT) is an established materials characterisation method based on time-of-flight mass spectrometry that provides elemental and compositional modelling of materials by providing a three-dimensional reconstruction of atoms from a sample with a sub-nanometre spatial resolution [57]. This technique is useful for inferring how the distribution of elements influences material properties, and to probe the complex, hierarchical structures of bulk materials. After data is obtained, a commercial software package can be used to assign isotope peaks in the mass spectrum, and subsequently visualise the data and perform a myriad of processing techniques (visualisation of individual elements or element groups, examination of interfaces, 1D and 2D compositional profiling, isosurface construction, etc.). It is a destructive technique; an atom probe tip can only be used once to obtain one dataset. A comprehensive overview of this technique is available elsewhere [58].

2.4 Mechanical Characterisation

2.4.1 Mechanical Properties

In order to properly characterise CCAs, it is important to measure their mechanical properties. The following section contains a brief explanation of the key properties measured and reported in the subsequent chapters to accurately appraise alloy strength and deformability. Most mechanical properties can be conceptually understood according to a generic stress-strain curve, such as the one presented in **Error! Reference source not found.**.
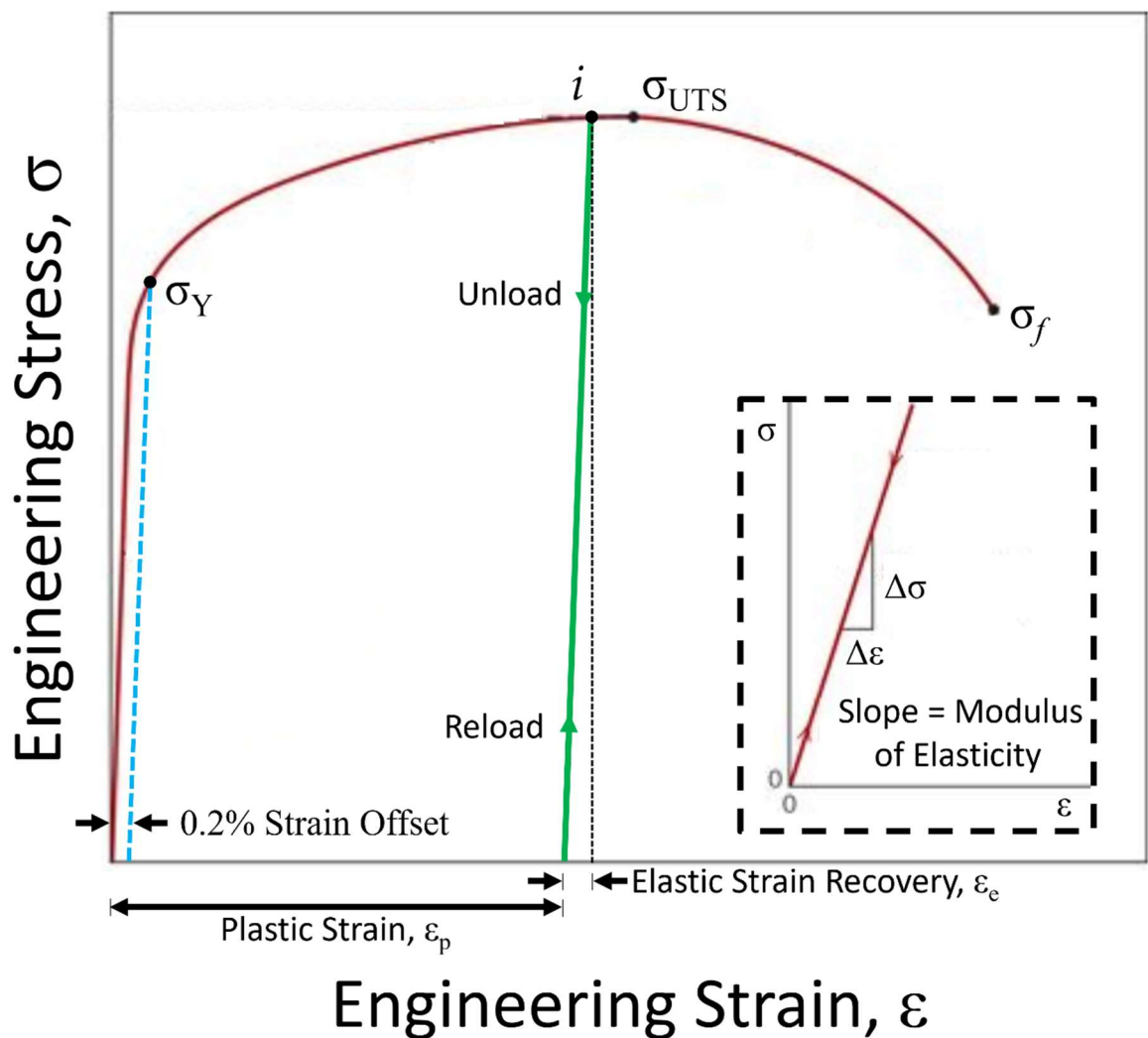
Figure 7: Generic engineering stress (σ) – strain (ε) curve for a ductile material. Adapted from [1].

- *Young's Modulus*

The Young's modulus, E, also referred to as the modulus of elasticity, is a material property correlated to the material's resistance to elastic deformation, or its stiffness. It is represented by the slope of the stress-strain curve in the elastic region of deformation, i.e. a ratio of tensile stress, σ, and tensile strain, ε, as per Equation 2.2;

$$E = \frac{\Delta\sigma}{\Delta\varepsilon} \qquad 2.2$$

- *Strain: Elastic Strain and Plastic Strain*

Engineering strain, ε, is a dimensionless parameter equal to the change in length at some instant during deformation, Δl, divided by the original length, l_0, as defined in Equation 2.3. The change in length during tensile deformation is simply the current length, l_i, minus the original length.

$$\varepsilon = \frac{\Delta l}{l_0} = \frac{l_i - l_0}{l_0} \qquad 2.3$$

There are two components of strain; elastic strain and plastic strain. The elastic component of strain can be calculated using Hooke's Law (Equation 2.6), whereas the plastic strain can be obtained by subtracting the elastic strain from the total strain. Elastic and plastic strain components (ε_e and ε_p, respectively) are illustrated in **Error! Reference source not found.**, for an arbitrary unloading point at i (where the loading-unloading path is annotated in green).

- *Ductility*

Ductility is the amount of plastic or permanent damage that has been sustained at fracture. It can be quantified by the amount of plastic strain sustained at fracture as a percent elongation, using a fracture length, l_f, as per Equation 2.4;

$$\%EL = \left(\frac{l_f - l_0}{l_0}\right) \times 100 \qquad 2.4$$

- **Stress and Strength**

Engineering stress is defined in Equation 2.5 as a measure of the instantaneous load or force, F, applied perpendicular to the specimen cross-section, A. Increasing the load over a particular area will increase the stress, whereas applying an identical load to a specimen with a larger cross-sectional area would reduce the resultant stress. The units of stress are Newtons per metre squared, denoted as N/m^2 or $N\ m^{-2}$, which is defined as a Pascal, denoted by Pa. Stress is related to strain via Hooke's Law, as per Equation 2.6.

$$\sigma = \frac{F}{A} \qquad\qquad 2.5$$

$$\sigma = E\varepsilon_e \qquad\qquad 2.6$$

Strength is a term for how much stress a material can accommodate. There are many different types of strengths (yield strength, tensile strength, and fracture strength are depicted in **Error! Reference source not found.**) which each have their own definitions. The yield strength, σ_Y, is the amount of stress required to initiate yielding, i.e. permanent plastic deformation. It also marks the point beyond which the stress-strain curve no longer exhibits linear behaviour. The exact point at which the stress-strain curve transitions from linear to non-linear is ambiguous, a 0.2% strain offset can be used to determine the yield stress (depicted in **Error! Reference source not found.**). The ultimate tensile strength, σ_{UTS}, occurs at the maximum value of engineering stress. The fracture strength, σ_f, is the stress at which failure occurs.

- **True Stress and True Strain**

Engineering stress does not take into account the change in cross-sectional area during deformation, because the calculation uses the initial geometry only. Therefore, Equation 2.7 and Equation 2.8 can be applied to calculate true stress, σ_T, and true strain, ε_T, respectively.

$$\sigma_T = \frac{F}{A_i} \qquad\qquad 2.7$$

$$\varepsilon_T = ln\frac{l_i}{l_0} \qquad\qquad 2.8$$

Where A_i is the instantaneous or current cross-sectional area, as opposed to the original cross-sectional area.

- ***Hardness***

Hardness is a measure of resistance to localised plastic deformation. It is possible to gain a relative understanding of how hard something is by indenting it with other materials. If the material being tested is damaged or not, it can be placed on a scale from 1 (talcum powder; very soft) to 10 (diamond; very hard). Sophisticated methods exist to quantitatively measure hardness in units of GPa, such as through nanoindentation (outlined in Section 2.4.2).

2.4.2 Nanoindentation

A nanoindentation system equipped with a Berkovich indenter can be used to measure mechanical properties, viz. hardness, H, and modulus of elasticity, E. These parameters are calculated using the Oliver-Pharr method (Figure 8), where P_{max} is the peak indentation load, h_{max} is the corresponding indenter displacement, h_f is the contact depth of the indenter impression after unloading, and S is the initial unloading stiffness [63]. The reduced modulus, E_r, and Poisson's Ratio, v, are related to E via Equation 2.9;

$$\frac{1}{E_r} = \frac{(1-v^2)}{E} + \frac{(1-v_i^2)}{E_i} \qquad\qquad 2.9$$

where v_i and E_i are indenter parameters.
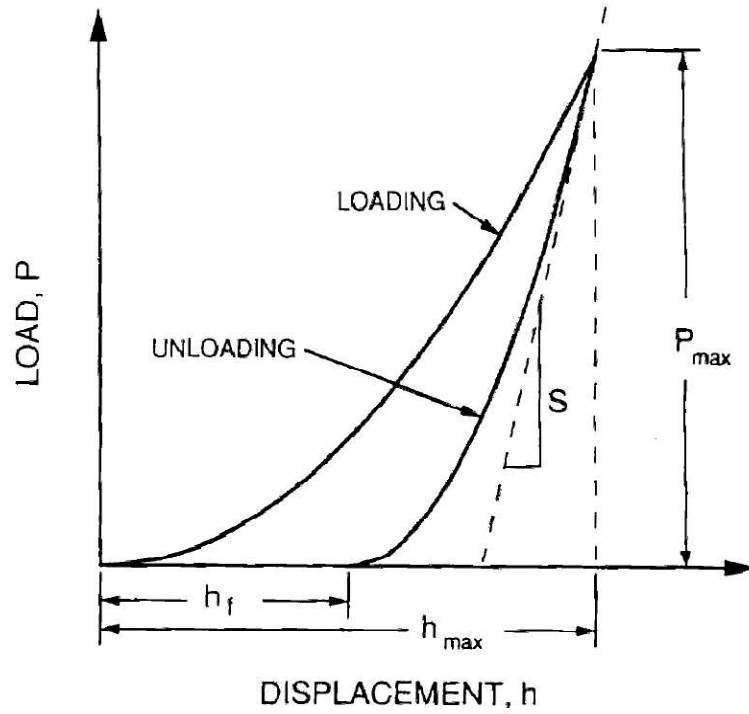
Figure 8: Schematic representation of load versus indenter displacement data for an indentation experiment. This figure is reproduced with a license through RightsLink [63].

If the indenter load is *P*, the elastic displacement of the indenter is *h*, and *A* is the projected area of the elastic contact, then *S* can be obtained via Equation 2.10;

$$S = \frac{dP}{dh} = \frac{2}{\sqrt{\pi}} E_r \sqrt{A}$$ 2.10

The hardness is defined in Equation 2.11;

$$H = \frac{P_{max}}{A}$$ 2.11

Calibration of the instrument is routinely performed with a standard fused quartz specimen ($E_r \sim 69$ GPa). In this work, the load function consists of loading to 50 mN, and then an unloading, which typically produces a penetration depth corresponding to about 10% of the total film thickness. The values reported in the publications are an average of multiple indentations, and the standard deviation is calculated using sample standard deviation (see Appendix B for further details).

After recording the mechanical properties obtained by using the Berkovich indenter, the alloys are deformed using a spherical indenter. Cross-sections of the spherical

indents are used to prepare deformed foils for analysis, as the indent impression is isotropic and thus the milling pattern orientation will not influence the resultant foil.

2.4.3 In-situ SEM nanomechanical testing
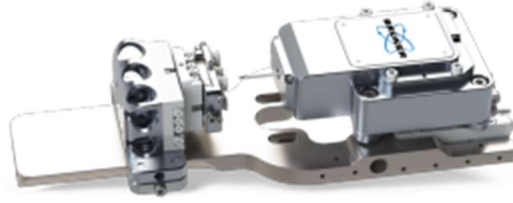
Figure 9: Hysitron PI 89 SEM PicoIndenter system.

The PI 89 SEM PicoIndenter (Figure 9) is used to conduct in situ compression tests of micropillars inside an SEM. The experiment outputs load and displacement data, which can then be converted into engineering and true stress and true strain data.

When calculating true stress and true strain, it can be difficult to obtain instantaneous values to conduct corresponding calculations. However, the geometry of the specimen is related to the measured load and displacement, as outlined by Greer et al. [64], which can simplify the scope of the calculations required. During deformation, it is assumed that the plastic volume of the cylinder is conserved. Thus, the product of final height and cross-sectional area, l_p and A_p, respectively, must equal the product of the initial height and cross-sectional area, as outlined in Equation 2.12;

$$A_p l_p = A_0 l_0 \qquad\qquad 2.12$$

The true stress in the elastic region obeys Hooke's law, and incorporating Equation 2.2, the following expression is obtained;

$$\varepsilon_e = \frac{\sigma}{E} = \frac{1}{E}\frac{P}{A_p} = \frac{1}{E}\frac{P l_p}{A_0 l_0} \qquad\qquad 2.13$$

The total true strain during deformation is the sum of elastic strain (Equation 2.13), and plastic strain components, expressed in Equation 2.14;

$$\varepsilon_t = \varepsilon_e + \varepsilon_p = \frac{1}{E}\frac{Pl_p}{A_0 l_0} - \ln\left(\frac{l_p}{l_0}\right) \qquad\qquad 2.14$$

Where P is the load applied to the pillar. The elastic compressive displacement is obtained by multiplying the elastic strain by the final height;

$$u_{el} = \frac{1}{E}\frac{P}{A_0 l_0} l_p^2 \qquad\qquad 2.15$$

The plastic compressive displacement is simply the displacement at any point on the loading curve, u, less the elastic displacement, as follows:

$$u_p = u - \frac{1}{E}\frac{P}{A_0 l_0} l_p^2 \qquad\qquad 2.16$$

Substituting the expression for u_p into $l_p = l_0 - u_p$, a quadratic expression in terms of l_p is obtained. Equation 2.17 can be obtained by applying the quadratic formula to solve for l_p;

$$l_p = \frac{EA_0 l_0}{2P}\left(1 - \sqrt{1 - 4\left(\frac{P}{EA_0 l_0}\right)(l_0 - u)}\right) \qquad\qquad 2.17$$

Finally, to obtain the corresponding stress, the measured load can simply be divided by the plastic area;

$$\sigma = \frac{PA_0 l_0}{l_p} \qquad\qquad 2.18$$

Thus, the true stress and strain can be calculated using Equations 2.14, 2.17, and 2.18, relying only on measured data (load, displacement), and constants.

Chapter 3

Deciphering deformation mechanisms of hierarchical dual-phase CrCoNi coatings

Statement of Authorship

Title of Paper	Deciphering deformation mechanisms of hierarchical dual-phase CrCoNi coatings
Publication Status	☑ Published ☐ Accepted for Publication ☐ Submitted for Publication ☐ Unpublished and Unsubmitted work written in manuscript style
Publication Details	S. J. Tsianikas, Y. Chen Y., and Z. Xie (2020). "Deciphering deformation mechanisms of hierarchical dual-phase CrCoNi coatings." Journal of Materials Science & Technology 39: 7-13.

Principal Author

Name of Principal Author (Candidate)	Simon Tsianikas	
Contribution to the Paper	Acquiring Data, Knowledge, Analysis, Drafting	
Overall percentage (%)	70%	
Certification:	This paper reports on original research I conducted during the period of my Higher Degree by Research candidature and is not subject to any obligations or contractual agreements with a third party that would constrain its inclusion in this thesis. I am the primary author of this paper.	
Signature		Date **24/02/2021**

Co-Author Contributions

By signing the Statement of Authorship, each author certifies that:

     i.   the candidate's stated contribution to the publication is accurate (as detailed above);

     ii.   permission is granted for the candidate in include the publication in the thesis; and

     iii.   the sum of all co-author contributions is equal to 100% less the candidate's stated contribution.

Name of Co-Author	Yujie Chen	
Contribution to the Paper	Knowledge, Analysis, Drafting	
Signature		Date 24 / 02 / 2022

Name of Co-Author	Zonghan Xie	
Contribution to the Paper	Conception, Knowledge, Analysis, Drafting	
Signature		Date 18/2/2022

Research Article

Deciphering deformation mechanisms of hierarchical dual-phase CrCoNi coatings

S.J. Tsianikas [a,*], Y. Chen [a,b,**], Z. Xie [a,c]

[a] School of Mechanical Engineering, The University of Adelaide, Adelaide, SA, 5005, Australia
[b] Centre for Advanced Thin Film Materials and Device, Faculty of Materials and Energy, Southwest University, Chongqing, 400715, China
[c] School of Engineering, Edith Cowan University, WA, 6027, Australia

ARTICLE INFO

ABSTRACT

Hierarchical CrCoNi medium entropy alloy (MEA) thin films with a dual-phase face-centred cubic (FCC) and hexagonal closed-packed (HCP) nanostructure were prepared on M2 steel substrates by closed field unbalanced magnetron sputtering. Nanoindentation tests show an ultra-high hardness of 9.5 GPa, attributable to large amounts of innate planar defects (i.e., growth twins and stacking faults) impeding dislocation motion in the coatings. A deep analysis of undeformed and post-mortem samples reveals grain refinement as the dominant deformation mechanism in FCC dominated regions, while phase transformation and shear banding played major roles in regions occupied by HCP phase. The grain refinement was facilitated by twin/matrix lamellae, with dislocations piling up and arranging into interconnecting grain boundaries. The shear banding was accelerated by innate planar defects in the HCP phase due to a lack of slip systems. Of particular interest is the observation of HCP → FCC phase transformation, which was catalysed by deformation-induced grain reorientation with innate stacking faults acting as embryos to grow the FCC phase. The results of this work suggest that multiple deformation pathways could be activated in CrCoNi coatings with assistance of growth defects, thereby imparting these technically important coatings appreciable ductility.

© 2020 Published by Elsevier Ltd on behalf of The editorial office of Journal of Materials Science & Technology.

1. Introduction

Following the discovery of high entropy alloys (HEAs), ternary alloy systems termed medium entropy alloys (MEAs) have emerged and are promising for more impact. This stems from the work of Gali and George [1], who demonstrated that increasing the number of alloying elements from four to five does not always improve the degree of solid solution strengthening. In addition, Wu et al. [2] reported no correlation between mechanical properties and number of principal elements, and, provided examples of alloys with the same configurational entropy but different strengths. The results of these studies and others prove that the nature of elements used is the crucial factor in the creation and development of high-performing alloys, rather than simply the number of principal elements used [3]. A prominent MEA that has been investigated in recent years is the ternary alloy CrCoNi [3–7]. Fabricated in a bulk form, its mechanical properties are superior to that of widely reported quinary alloy CrMnFeCoNi despite having lower configurational entropy [4]. Specifically, its reported tensile strength and ductility are ∼1 GPa and ∼70%, respectively [3], attributable to interactions between dislocations and 3D twin architectures [7]. More recently, a high hardness (∼10 GPa) has been reported in sputter-deposited CrCoNi coatings [8], supposedly attributed to its unique microstructural features including twin boundaries [9], stacking faults, a dual-phase structure, and textured columnar grains [8].

Most HEAs and MEAs are prepared in a bulk form through arc melting and casting, which incurs very high material and energy costs and, therefore, research into HEA and MEA thin-film and coating deposition onto low-cost metal substrates is receiving increased attention [10]. Aside from lowering the costs to a great extent, these films and coatings also exhibit excellent mechanical properties [8,10–15], when compared to their bulk counterparts [8,15].

The efficacy of CrCoNi as a protective coating has been examined by Cao et al. [16,17] and Chen et al [8]. The incorporation of the Ti wetting layer increases coating adhesion [18] and, more impor-

tantly, can cause the grains to change from an elongated shape to much finer equiaxed morphology; induced grain refinement can change from 50 nm to 20 nm [16]. The work of Cao et al. [16,17] looked into the differences between coatings with and without interlayers and rationalised mechanical properties by evaluating the phase composition, grain diameter and defects (innate & post-mortem). Chen et al. [8] examined a monolithic CrCoNi coating via high angle annular dark field (HAADF) scanning transmission electron microscopy (STEM), and shed light on its exceptional mechanical properties by unpacking the hierarchical nanostructure of the as-deposited coating. However, their work and analysis is limited to microstructural characterization, and consequently, the deformation mechanisms of the CrCoNi alloy coating remain unexplored.

In this study, we employed nanoindentation and HAADF STEM techniques to investigate the deformation mechanisms of the CrCoNi coatings with particular focus on structural characterization of both undeformed and post-mortem thin film samples. The CrCoNi coatings synthesised via magnetron sputtering demonstrate an ultra-high hardness, and possess a high density of planar defects, a mixture of FCC & HCP phases, and textured columnar nanograins. This study adds critical insights to previous studies of CrCoNi coating by revealing its deformation mechanisms, featuring (1) HCP → FCC phase transformation, (2) grain refinement and (3) shear banding.

2. Materials and methods

The CrCoNi/Ti coatings were deposited at a rate of $\sim$72 nm/min by closed field unbalanced magnetron sputtering ion plating (CFUMSIP) onto AISI M2 high speed steel substrates, using a UDP650 magnetron sputtering system (Teer Coatings Ltd, UK). The steel substrates were hardened to HRC 60, finely polished to $R_a \sim$0.03 μm, degreased, ultrasonically cleaned, and subsequently blown dry in flowing nitrogen gas. One CrCoNi alloy target (China Material Technology Co. Ltd) with composition of 1:1:1 at%, purity of 99.5% and dimensions of 345 mm × 145 mm × 5 mm was used for the deposition. The substrates were stationary during deposition, and the target-to-substrate distance was fixed at 170 mm. The substrate holder was biased with pulsed DC at a frequency of 250 kHz. The vacuum chamber was pumped down to a background pressure of $<2 \times 10^{-6}$ Torr by controlling the flow rate of Ar (50 sccm). The DC current applied to the CrCoNi target was fixed at 4.0 A (sputtering power 1.5 kW). The deposition process of the coatings comprises three major steps: plasma ion cleaning ($-$450 V bias, 30 min), Ti interlayer deposition ($-$60 V bias, 200 nm thickness), and CrCoNi deposition ($-$60 V bias, 14 min). Ion etching of the steel substrates at the first stage was used to remove the oxide layer and contaminants on the substrate surface. The CrCoNi target current (DC) was maintained at 4.0 A (sputtering power $\sim$1.5 kW), corresponding to a nominal deposition rate of $\sim$72 nm/min. The titanium target current (DC) was set at 4.0 A (sputtering power $\sim$1 kW), corresponding to

a nominal deposition rate of 10 nm/min. No external heating was used during coating deposition.

Focussed ion beam milling (FIB) (FEI Helios Nanolab 600, The Netherlands) was used to prepare and extract thin sections to a thickness of $\sim$50 nm for analysis via scanning transmission electron microscopy (STEM) and energy dispersive X-ray spectroscopy (EDX) (Titan Themis 80–200, The Netherlands). The microstructure was studied with a field emission transmission electron microscope (TEM) (Phillips CM200, Netherlands).

A nanoindentation system (Fischer-Cripps Laboratories IBIS Nanoindenter, Australia) equipped with a Berkovich indenter was used to measure mechanical properties, viz. hardness (H) and modulus of elasticity (E). Calibration of this instrument was routinely performed with a standard fused quartz specimen ($E_r \sim$ 69 GPa). The load function consisted of a loading up to 50 mN, and then an unloading. The penetration depth corresponded to about 10% of the total film thickness to minimise the effect of the substrates, and the hardness and modulus were calculated using the Oliver-Pharr method [19] on the load-displacement data measured (see Fig. S1). The values reported are an average of fifteen indentations, and the standard deviation was also calculated and provided. In order to prepare deformed samples for TEM analysis, a spherical indenter (radius = 5 μm) was used at loads of 200 mN and 400 mN.

3. Results

3.1. Microstructural analysis

Fig. 1(a) shows EDX mapping for the undeformed sample, revealing a homogenous distribution of Co, Cr and Ni atoms (and therefore no locally enriched regions). The microstructure obtained via TEM (Fig. 1(b)) shows a columnar grain structure, with grain widths of approximately 20–30 nm. It consists distinctive regions of; perfect FCC, FCC with stacking faults, FCC with twinning, and alternating FCC & HCP phases within a single column (Fig. 1(c, d and e), respectively). Extensive STEM investigations reveal that these unique regions are randomly distributed within each columnar grain. A close examination indicates that regions of mixed FCC and HCP are predominantly FCC, with the HCP volume fraction varying between 25% and 40%. The volume fraction of HCP was calculated by dividing the thickness of HCP lamellae by the total thickness (i.e. HCP + FCC) examined in five columnar grains observed in STEM images, and was found to be larger close to the substrate and smaller near the surface.

3.2. Mechanical properties

The results of the nanoindentation testing are shown in Table 1. The wear parameters H/E and H^3/H^2 values are also tabulated, which represent the material's elastic strain to failure, and resistance to plastic deformation, respectively [20]. The values of hardness (H) and modulus of elasticity (E) measured are similar to

Table 1
Nanoindentation Values obtained from this project, and values obtained from literature, with H/E and H^3/E^2 values.

Sample	Hardness (GPa)	Young's Modulus (GPa)	Wear Parameter H/E	H^3/E^2
CrCoNi/Ti (Present Study)	9.5 ± 0.1	238 ± 4	0.0399	0.0151
CrCoNi (1 μm and 3 μm) [16]	$\sim$10	$\sim$250	0.0400	0.016
CrCoNi/Ti (1 μm and 3 μm) [16]	$\sim$9.2	$\sim$230	0.0400	0.014
CrCoNi/Ti (multilayered) [17]	7.6 ± 0.43	233 ± 13	0.033	0.0081
CrCoNi [8]	10	267	0.0375	0.014
$Co_{19}Cr_{19.2}Fe_{19.2}Ni_{19.1}Cu_{23.5}$ [38]	3.72	188.5	0.0197	0.0014
$Co_{13}Cr_{12.2}Fe_{12.4}Ni_{13.2}Cu_{17.7}Al_{31.5}$ [38]	2.62	174.3	0.0150	0.00059
$Al_{0.3}CoCrFeNi$ [39]	3.33	216	0.0154	0.00079
AlCoCrFeNi [39]	10.1	251	0.0402	0.016
AlCoCrCuFeNi [40]	8.13	172	0.0473	0.018
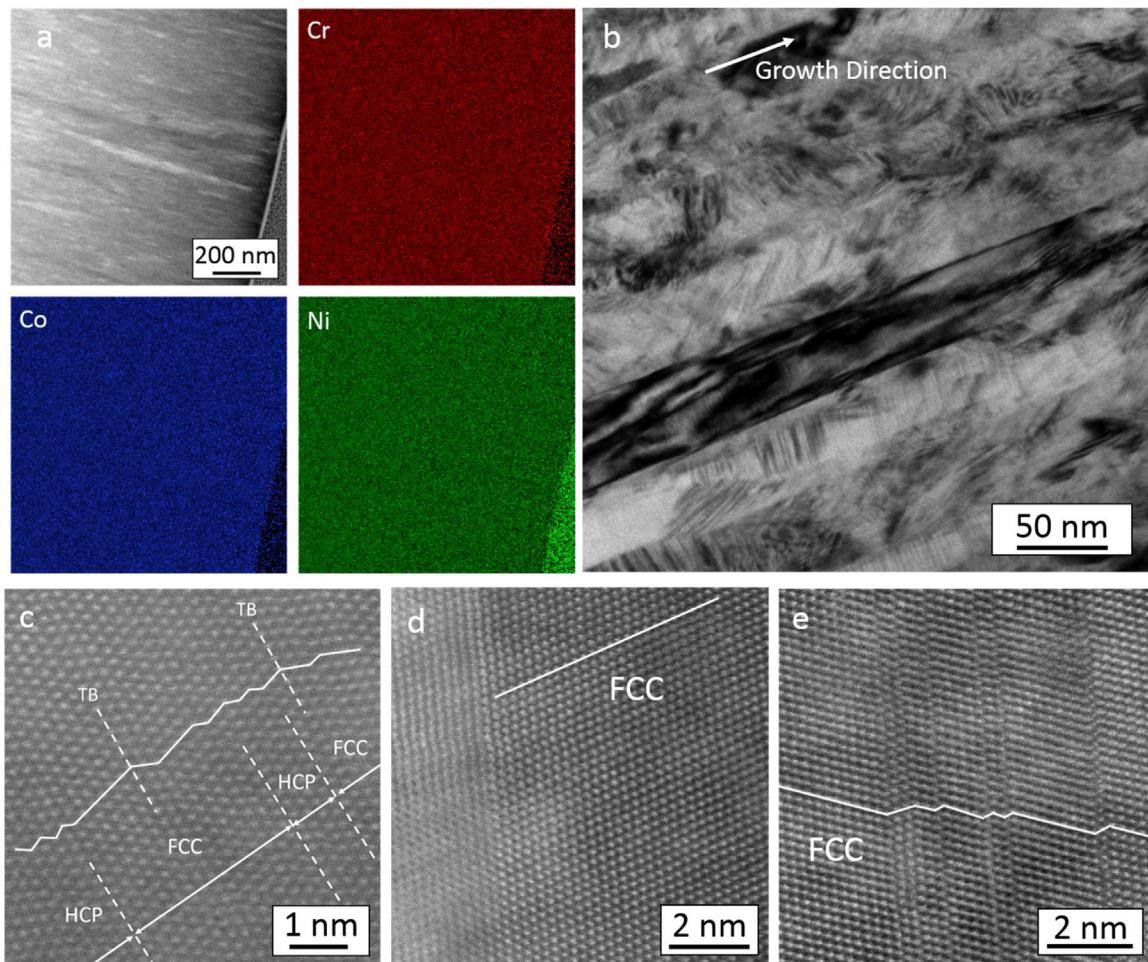
Fig. 1. As-deposited CrCoNi sample; (a) EDX mapping of a selected region of the sample shown in the top-left pane. A small segment of platinum is included in the bottom-right for reference, (b) nanocolumnar structure, (c) alternating HCP and FCC phases, with twinning present, (d) perfect FCC crystal and grain boundary, and (e) FCC region with stacking faults.

those obtained by Cao et al. [16,17] and Chen et al. [8]. Compared to other HEAs, the CrCoNi samples have a relatively high hardness and wear parameters. Its values are near those of AlCoCrCuFeNi, which represents the highest values ever reported.

3.3. Deformation microstructure

The STEM images of the TEM sample deformed under a load of 400 mN reveal that there are no cracks in the coating, nor can any delamination between coating and substrate be observed. This is an extraordinary response for such an ultra-hard coating, suggesting a possibility to overcome the long-standing hardness-toughness trade-off [7]. There is a pile-up of material at the edge of the indent (Fig. 2(a)), manifesting a metal-like ductile behaviour. Post-mortem TEM shows a high extent of grain refinement under the indent site (Fig. 2(b & c)); grain diameters range between 10 nm and 60 nm, with some columnar grains remaining intact at the indent site at 200 mN (Fig. 2(c)). The microstructure when subject to a load of 200 mN (Fig. 2(e)) consists of twinned FCC region and some stacking faults, whereas at 400 mN (Fig. 2(d)), this twinning is not present, and the number of stacking faults has decreased. The absence of HCP in the nanograins indicates that HCP → FCC phase transformation has most likely occurred. The dislocations at one of the grain boundaries are annotated in Fig. 2(f). Under a load of 200 mN, the columnar grains above the grain refinement region exhibit an FCC structure at the surface, and further down grain refinement precursors are visible, in addition to a structure rich in defects.

At a load of 400 mN, a shear band is visible near the bottom of the coating towards the Ti wetting layer (Fig. 3(a)); the sharp edges distinguish it from the surrounding intact columnar grains, with a thickness of approximately 50 nm. The shear band is not observed at a load of 200 mN. On close examination of the newly formed nanograins and shear band regions, the phases are entirely FCC (Fig. 3(b & c)), whereas the adjacent un-sheared region (Fig. 3(b)) has an HCP crystal structure, indicating that HCP → FCC phase transformation has taken place within the shear band. In addition, the crystal structure within the shear band has a different orientation to the original structure, suggesting that crystallographic rotation has occurred.

The adhesion of the coatings is not consistent with results reported by Cao et al. [16], who asserted that thicker coatings would experience accumulated stress at the coating/substrate interface during deformation, causing adhesion failure. The non-delamination is further corroborated by observations from the TEM samples which were subject to out-of-plane bending during ion milling; damage would have been evident at the interface if delamination did occur.

4. Discussion

In bulk samples prepared *via* high temperature processes such as casting, the FCC phase is typically formed as it is more thermodynamically favoured than HCP at high temperatures [3,4,7,21]. Upon cooling, the FCC to HCP phase transformation is kinetically hindered
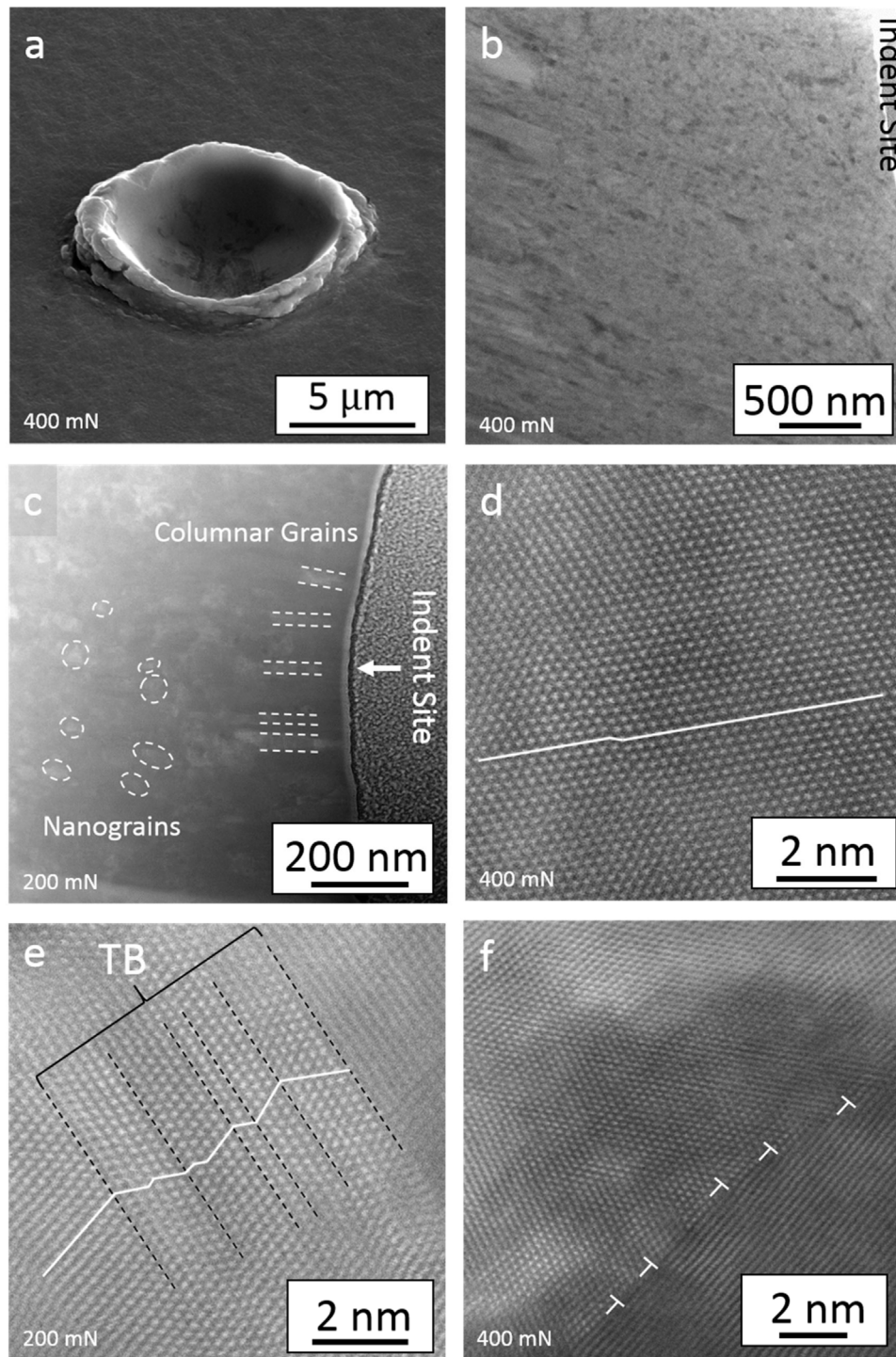
Fig. 2. Samples after deformation; (a) indent site showing pile-up; (b & c) microstructures after deformation of 400 mN (b) and 200 mN (c); (d & e) STEM image of nanograins obtained ~1 µm below the sample surface showing an equiaxed grain for 400 mN (d) and twin/matrix lamellae for 200 mN (e), and; (f) dislocations (marked by white ⊥ symbols) at the grain boundary of a nanograin.

due to a high energy barrier between FCC and HCP phase despite HCP having a lower Gibbs free energy at room temperature [8]. The HCP phase is observed in magnetron sputtered coatings [8,16] because it is a low temperature process, allowing for the formation of HCP phase. In addition, it has been suggested that innate planar defects could facilitate a phase transformation from FCC to HCP, via the formation of stacking faults on every second {111} plane [8]. Meanwhile, the variation in relative fraction of HCP from the

substrate to the surface can be explained by the temperature gradient which results during deposition. Cao et al. [16] confirmed the presence of both FCC and HCP phases in the CoCrNi coatings with XRD data, however they asserted that the HCP phases are cobalt-only. While STEM images do confirm the presence of HCP and FCC phases, EDX mapping (Fig. 1(b)) indicates all three elements Cr, Co and Ni are homogenously distributed. Given that Cr, Co, and Ni all have similar atomic radii of 0.125 nm (to three significant figures
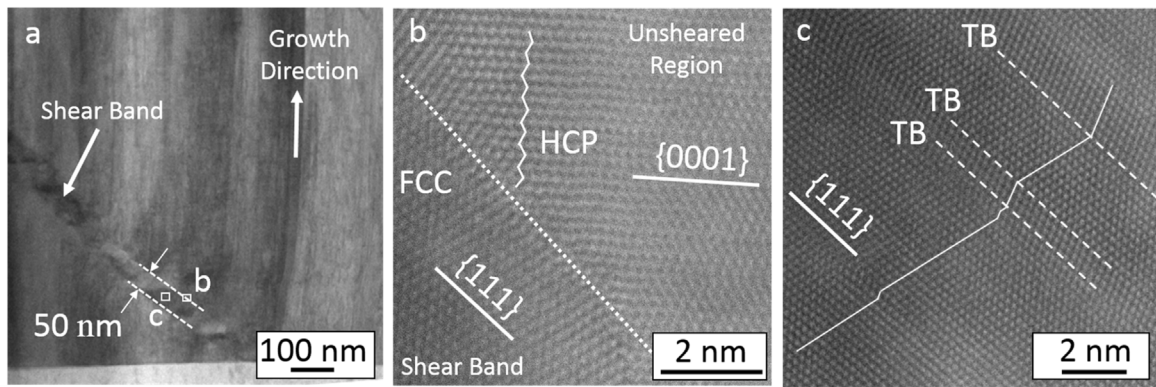
Fig. 3. (a) Shear band region, visible by its very distinguishable edges. STEM images (b) depict the edge of the shear band region and (c) reveal the structure inside the shear band as FCC, with twin/matrix lamellae.

[22]), and the fact that atomic spacings are used to index peaks, it is likely that a peak indexed as cobalt-only in fact has all three elements present.

As mentioned in Section 3.3, STEM images of the as-deposited samples possess regions of predominantly FCC single crystal and HCP/FCC lamellae, with multiple stacking faults and twinning (Fig. 4(a)) considered as growth planar defects of a sputtered film [23]. The high hardness of CrCoNi (~9.5 GPa) is attributable to the presence of these planar defects, dual-phase FCC/HCP regions, and nanocolumnar grain boundaries, all of which are known to serve as barriers to dislocation motion [24] thereby bringing about strengthening effects [25]. In addition, HCP has less slip systems present than FCC, therefore its incorporation in the coatings also leads to a higher hardness [8]. The combination of these distinctive structural elements results in a much higher hardness than that obtained for the purely FCC CrCoNi bulk sample [21].

Prior to the work of Tao et al. [26], it was understood that strain-induced grain refinement occurs solely via dislocation activity. Since the grain refinement mechanism is sensitive to crystal structure (FCC preferred) and the deformation conditions, the plastic deformation of FCC structured materials under certain conditions could lead to multiple deformation twinning and the formation of twin/matrix lamellae [27]. Upon further straining, twin/matrix lamellae are refined into equiaxed nanosized grains with dislocations accumulated into interconnecting bands, which eventually form grain boundaries [27]. Thus, the innate twin/matrix lamellae (Fig. 1(c)) in the as-deposited coatings with FCC as dominant phase provide a conducive environment for grain refinement to take place under applied stress. In addition to the elimination of twin boundaries via grain refinement, nanograins in the heavily deformed sample have a much lower concentration of twin boundaries (Fig. 4(c)). Therefore, detwinning within the FCC phase is another deformation mechanism present in this sample, likely achieved via glide of twin dislocations [28]. As the grains become further refined, detwinning occurs more readily than twinning, eventually leading to the annihilation of twins [29]. Lastly, the preservation of columnar nanograins under a load of 200 mN (Fig. 4(b)) might be due to the fact that the initial structure is nanofibre-like making it very strong, and is therefore prone to buckling when the indentation load was applied [30]. The crystal structure within these columns (described in Section 3.3) also changed under the compressive stress, producing perfect FCC crystal via HCP → FCC phase transformation (discussed below). Upon increased loading, this buckling zone expanded to meet the sample surface, which is why these columnar grains are no longer present at a force of 400 mN.

The extent of phase transformation in the shear band, observable only at load of 400 mN, is evident, wherein the crystal structure comprises exclusively FCC phase (Fig. 3(b)). Shear band formation requires obstacles to dislocation motion [31], which would preferentially form in HCP phase rather than FCC (as there are less slip systems in HCP structure) and also have a tendency to form in materials with a highly twinned structure [32]. In the present study, the grain refinement is dominant during the early stage of deformation, since the deformed region is primarily composed of FCC phase. Only when subjected to a heavy load (400 mN), HCP phase dominated regions (still well-preserved and rich in planar defects) near the substrate (Fig. 3(b)) experienced deformation, leading to shear band formation under high strain localisation (Fig. 4(c)).

Phase transformation is another deformation mechanism evident in the sample, a mechanism known to strongly affect the deformation capability of materials [33]. One example of this is the increase in ductility afforded by the HCP → FCC phase transformation, due to the increase in number of slip systems [34]. In one study of high-pressure torsion of cobalt in the form of powders [35], an FCC → HCP phase transformation dominated until the average grain size reached the sub-micrometre level, upon which the reverse HCP → FCC phase transformation occurred. The deformation at the later stage was controlled by partial dislocation slips, which resulted in an accumulation of stacking faults; the continuous accumulation of these staking faults led to the growth of FCC lamellae [35]. In another study, deformation-induced HCP → FCC phase transformation in a CoNi alloy was not attributed to the growth of individual stacking faults. Rather, innate stacking faults formed during the sample synthesis acted as embryos to grow the FCC phase [36]. Hence, the innate stacking faults formed during sputter deposition in the CrCoNi coatings are believed to act as precursors to enable the observed HCP → FCC phase transformation. The phase transformation is also facilitated by the rotation of crystals inside the refined region and within the shear band. Due to the strong texture of the as-deposited samples, the applied load was along the [111] direction in the FCC phase and along the [0001] direction in the HCP phase. According to Schmid's law [37], dislocation slip could occur on the {111} planes of the FCC phase, but plastic deformation was difficult to activate in the HCP phase due to the lack of resolved shear stress on the (0001) slip plane. Under the influence of grain refinement and subsequent crystal rotation, however, the resolved shear stress on the (0001) plane in the rotated HCP regions could cause phase transformation presumably via Shockley partial dislocations [36]. The work is under way, assisted by *in-situ* micropillar compression and first-principle calculations, to elucidate the mech-
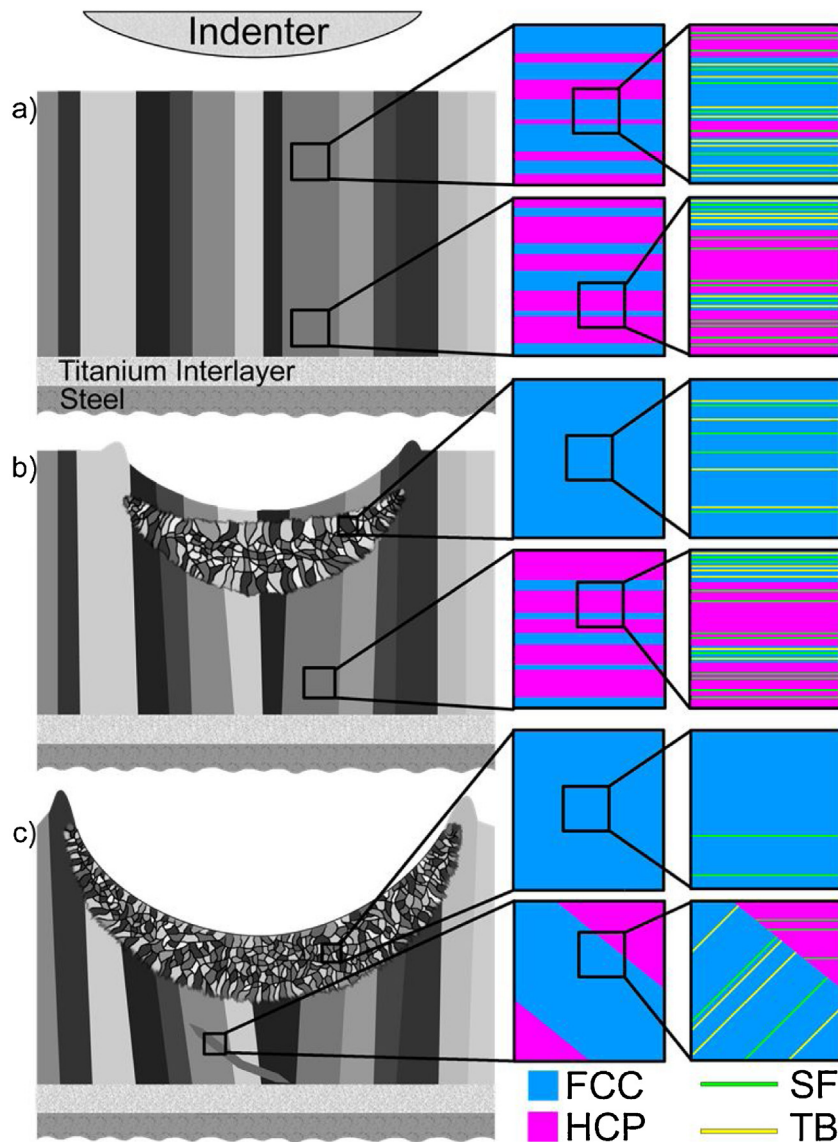
Fig. 4. Generalised deformation mechanism of the CrCoNi coating: (a) pristine columnar structure, HCP/FCC regions and presence of stacking faults and twin boundaries; (b) partial deformation caused by 200 mN showing grain refinement onset beneath the indent site with phase transformation and elimination of some planar defects in nanograins, and; (c) heavy deformation induced by 400 mN, showing further elimination of planar defects in nanograins, and shear band formation.

anism underlying the HCP to FCC transformation in this type of coating.

5. Conclusions

Under closed field unbalanced magnetron sputtering, a large number of growth defects, such as stacking faults and twin boundaries, were developed in the CrCoNi coatings, which consist primarily of FCC phase coexisting with small fractions of HCP phase and FCC/HCP lamellae. Under indentation, multiple deformation mechanisms were activated in a systematic manner, which were regulated by innate planar defects. The following conclusions can be drawn:

(1) Where FCC phase is dominant, the deformation process was governed by grain refinement, producing equiaxed nanoscale grains as a result of dislocation activities.
(2) In regions where a high fraction of HCP phase exists, high strain localisation was developed due to the lack of slip systems. As such, shear banding took place, facilitated by the presence of high density planar defects.

(3) Innate stacking faults, acting as embryos, are responsible for HCP → FCC phase transformation under mechanical loading. However, this phase transformation only proceeds after a change in orientation, via grain refinement or shear banding, both of which result in the realignment of the {111} planes.

Therefore, the marked plastic response of these ultra-hard coatings is due to the different deformation pathways incorporated over multiple length scales under indentation loading.

Acknowledgements

acknowledge Dr Zhifeng Zhou of City University of Hong Kong who prepared the coatings.

Appendix A. Supplementary data

Supplementary material related to this article can be found, in the online version, at doi:https://doi.org/10.1016/j.jmst.2019.07.055.

References

[1] A. Gali, E.P. George, Intermetallics 39 (2013) 74–78.
[2] Z. Wu, H. Bei, F. Otto, G.M. Pharr, E.P. George, Intermetallics 46 (2014) 131–140.
[3] B. Gludovatz, A. Hohenwarter, K.V.S. Thurston, H. Bei, Z. Wu, E.P. George, R.O. Ritchie, Nat. Commun. 7 (2016).
[4] G. Laplanche, A. Kostka, C. Reinhart, J. Hunfeld, G. Eggeler, E.P. George, Acta Mater. 128 (2017) 292–303.
[5] J. Miao, C.E. Slone, T.M. Smith, C. Niu, H. Bei, M. Ghazisaeidi, G.M. Pharr, M.J. Mills, Acta Mater. 132 (2017) 35–48.
[6] S. Yoshida, T. Bhattacharjee, Y. Bai, N. Tsuji, Scr. Mater. 134 (2017) 33–36.
[7] Z. Zhang, H. Sheng, Z. Wang, B. Gludovatz, Z. Zhang, E.P. George, Q. Yu, S.X. Mao, R.O. Ritchie, Nat. Commun. 8 (2017).
[8] Y. Chen, Z. Zhou, P. Munroe, Z. Xie, Appl. Phys. Lett. 113 (2018).
[9] X. Zhang, A. Misra, H. Wang, M. Nastasi, J.D. Embury, T.E. Mitchell, R.G. Hoagland, J.P. Hirth, Appl. Phys. Lett. 84 (2004) 1096–1098.
[10] W. Li, P. Liu, P.K. Liaw, Mater. Res. Lett. 6 (2018) 199–229.
[11] T.-K. Chen, M.-S. Wong, T.-T. Shun, J.-W. Yeh, Surf. Coat. Technol. 200 (2005) 1361–1365.
[12] C. Huang, Y. Zhang, J. Shen, R. Vilar, Surf. Coat. Technol. 206 (2011) 1389–1395.
[13] T.M. Yue, H. Xie, X. Lin, H. Yang, G. Meng, Entropy 15 (2013) 2833.
[14] H. Zhang, Y. Pan, Y. He, H. Jiao, Appl. Surf. Sci. 257 (2011) 2259–2263.
[15] H. Zhang, Y. Pan, Y.-Z. He, Mater. Des. 32 (2011) 1910–1915.
[16] F. Cao, P. Munroe, Z. Zhou, Z. Xie, Surf. Coat. Technol. 335 (2018) 257–264.
[17] F. Cao, P. Munroe, Z. Zhou, Z. Xie, Surf. Coat. Technol. 350 (2018) 596–602.
[18] S. Kim, C. In, S.K. Choi, S. Chun, Journal de Physique IV Colloque 2 (1991) 609–616.
[19] W.C. Oliver, J. Mater. Res. 7 (1992) 1564–1583.
[20] J.C. Weaver, Q. Wang, A. Miserez, A. Tantuccio, R. Stromberg, K.N. Bozhilov, P. Maxwell, R. Nay, S.T. Heier, E. DiMasi, D. Kisailus, Mater. Today 13 (2010) 42–52.
[21] J. Miao, T. Guo, J. Ren, A. Zhang, B. Su, J. Meng, Vacuum 149 (2018) 324–330.
[22] W. Callister, D. Rethwisch, Materials Science and Engineering an Introduction, 9th ed., Wiley, United States of America, 2014.
[23] X.G. Li, L.F. Cao, J.Y. Zhang, J. Li, J.T. Zhao, X.B. Feng, Y.Q. Wang, K. Wu, P. Zhang, G. Liu, J. Sun, Acta Mater. 151 (2018) 87–99.
[24] K. Lu, Nat. Rev. Mater. 1 (2016) 16019.
[25] X. Zhang, H. Wang, X.H. Chen, L. Lu, K. Lu, R.G. Hoagland, A. Misra, Appl. Phys. Lett. 88 (2006), 173116.
[26] N.R. Tao, X.L. Wu, M.L. Sui, J. Lu, K. Lu, J. Mater. Res. 19 (2011) 1623–1629.
[27] N.R. Tao, K. Lu, Scr. Mater. 60 (2009) 1039–1043.
[28] J. Wang, N. Li, O. Anderoglu, X. Zhang, A. Misra, J.Y. Huang, J.P. Hirth, Acta Mater. 58 (2010) 2262–2270.
[29] Y.T. Zhu, X.Z. Liao, X.L. Wu, J. Narayan, J. Mater. Sci. 48 (2013) 4467–4475.
[30] Y. Zou, H. Ma, R. Spolenak, Nat. Commun. 6 (2015) 7748.
[31] N. Jia, F. Eisenlohr, F. Roters, D. Raabe, X. Zhao, Acta Mater. 60 (2012) 3415–3434.
[32] C.S. Hong, N.R. Tao, X. Huang, K. Lu, Acta Mater. 58 (2010) 3103–3116.
[33] J. Li, Q. Fang, B. Liu, Y. Liu, Acta Mater. 147 (2018) 35–41.
[34] Z. Zhang, M. Li, D. Guo, Y. Shi, X. Zhang, H.-E. Schaefer, Mater. Sci. Eng. A 594 (2014) 321–323.
[35] K. Edalati, S. Toh, M. Arita, M. Watanabe, Z. Horita, Appl. Phys. Lett. 102 (2013), 181902.
[36] C. Hitzenberger, H.P. Karnthaler, A. Korner, Acta Metall. 36 (1988) 2719–2728.
[37] Y. Chen, X. An, X. Liao, Appl. Phys. Rev. 4 (2017).
[38] Y. Ma, Y.H. Feng, T.T. Debela, G.J. Peng, T.H. Zhang, Int. J. Refract. Metals Hard Mater. 54 (2016) 395–400.
[39] Z.-M. Jiao, S.-G. Ma, G.-Z. Yuan, Z.-H. Wang, H.-J. Yang, J.-W. Qiao, J. Mater. Eng. Perform. 24 (2015) 3077–3083.
[40] R.S. Ganji, P. Sai Karthik, K. Bhanu Sankara Rao, K.V. Rajulapati, Acta Mater. 125 (2017) 58–68.

Chapter 4

Self-toughened body-centred cubic structured high entropy alloy

Statement of Authorship

Title of Paper	Self-toughened HEA with BCC structure
Publication Status	☑ Published ☐ Accepted for Publication ☐ Submitted for Publication ☐ Unpublished and Unsubmitted work written in manuscript style
Publication Details	Tsianikas, S. J., Y. Chen, J. Jeong, S. Zhang, Z. Xie (2021). "Self-toughened body-centred cubic structured high entropy alloy", Nanoscale 13 (6), 3602-3612.

Principal Author

Name of Principal Author (Candidate)	Simon Tsianikas
Contribution to the Paper	Acquiring Data, Knowledge, Analysis, Drafting
Overall percentage (%)	70%
Certification:	This paper reports on original research I conducted during the period of my Higher Degree by Research candidature and is not subject to any obligations or contractual agreements with a third party that would constrain its inclusion in this thesis. I am the primary author of this paper.
Signature	Date 24/02/2022

Co-Author Contributions

By signing the Statement of Authorship, each author certifies that:

i. the candidate's stated contribution to the publication is accurate (as detailed above);

ii. permission is granted for the candidate in include the publication in the thesis; and

iii. the sum of all co-author contributions is equal to 100% less the candidate's stated contribution.

Name of Co-Author	Yujie Chen
Contribution to the Paper	Knowledge, Analysis, Drafting
Signature	Date 24/02/2022

Name of Co-Author	Jiwon Jeong
Contribution to the Paper	Acquiring Data, Knowledge, Analysis
Signature	Date 13.11.2021

Name of Co-Author	Siyuan Zhang
Contribution to the Paper	Acquiring Data, Knowledge, Analysis
Signature		Date	12. 11. 2021

Name of Co-Author	Zonghan Xie
Contribution to the Paper	Conception, Knowledge, Analysis, Drafting
Signature		Date	18/2/ 2022

Check for updates

Self-toughened high entropy alloy with a body-centred cubic structure†

Simon Tsianikas, [ID] *[a] Yujie Chen, [ID] *[a,b] Jiwon Jeong, [ID] [c] Siyuan Zhang [ID] [c] and Zonghan Xie [ID] [a]

Multiple interstitial elements (B, C and O), were incorporated into a body-centred cubic (BCC) FeMnCoCr-based interstitial high entropy alloy (iHEA). While achieving an impressive yield strength of 2.55 GPa, the new alloy also possesses appreciable ductility under mechanical loading. The unusual combination of hardening effects brought about by interstitial atoms, compositional fluctuations, and fine grain size greatly strengthened the alloy by inhibiting dislocation motion. Moreover, interstitial elements helped reinforce the grain boundaries through segregation and also assisted in tuning the phase stability. The new alloy transformed from the BCC to hexagonal closed-packed (HCP) phase initially. With increasing load the HCP phase was gradually converted into face-centred cubic (FCC); the resultant HCP/FCC nanolaminates enhanced plasticity *via* strain partitioning. Under higher loads, the FCC phase became dominant, giving rise to deformation twinning. Taken together, the newly developed BCC structured iHEA affords not only high strength, but also confers remarkable ductility through multiple deformation pathways.

1. Introduction

High entropy alloys (HEAs) are a new class of materials defying conventional alloy design[1,2] and displaying a wide range of exceptional physical and mechanical properties.[3–9] The HEAs are single-phase solid solutions of generally equiatomic mixtures of metallic elements that maximize the configurational entropy.[10] Recently, the HEA design restrictions surrounding single-phase stability and near equiatomic compositions have been relaxed,[11] as entropy stabilised single-phase HEAs do not necessarily possess superior properties to other multi-principal-element alloy systems.[7,8,12–16] This move opens up the compositional space available to HEAs, and rekindles a new stage of HEA development. By tuning the ratios of the multiple principal elements, the metastability-engineering approach has ushered in a new variety of HEAs through tailoring stacking fault energy (SFE) that triggers transformation-induced plasticity (TRIP) and/or twinning-induced plasticity (TWIP).[17] For example, TRIP effect was introduced into the non-equiatomic $Fe_{50}Mn_{30}Co_{10}Cr_{10}$ alloy with a metastable Face-Centred Cubic (FCC)/Hexagonal Close-Packed (HCP) dual phase to simultaneously increase the strength and ductility.[17–19] This design strategy was also utilised to enhance the ductility of Body-Centred Cubic (BCC) structured TaHfZrTi HEA *via* tailoring phase stability and promoting the BCC to HCP phase transformation.[20]

However, tuning the atomic ratio of principal elements alone has limitations in further enhancing mechanical properties.[21] To fill the design gap, smaller atoms (*e.g.*, carbon, oxygen and boron) have been incorporated to form interstitial HEAs (iHEAs).[22] Interstitial atoms can induce lattice distortions and increase lattice friction stress, which hampers dislocation motion.[22] The success of this approach was demonstrated in the development of $Fe_{49.5}Mn_{30}Co_{10}Cr_{10}C_{0.5}$ alloy,[22] which exhibits an excellent strength-ductility combination. This is due to an improvement in the alloy's strain hardening capacity *via* instigating and uniting TWIP and TRIP effects. The attractiveness of this approach has also been shown when 2 at% oxygen was added to a refractory HEA TiZrHfNb; ordered O–Zr–Ti-rich complexes formed, which pinned dislocations and promoted cross slip, resulting in an increase in the tensile strength by 48% and tensile ductility by 95%.[23] The interstitials can also enhance grain boundary stability, regulate phase equilibrium and deformation mechanisms.[24] For example, low concentrations of boron have also been utilised to develop high strength iHEAs, as boron drives grain refinement and enhances the bonding strength of grain boundaries.[21] However, previous studies have focussed on the effect of adding only one interstitial element (O, B or C). Thus, it is

*[a]School of Mechanical Engineering, The University of Adelaide, SA 5005, Australia.
E-mail: simon.tsianikas@adelaide.edu.au, yujie.chen@adelaide.edu.au*
[b]Centre for Advanced Thin Film Materials and Devices, Faculty of Materials and Energy, Southwest University, Chongqing 400715, China
[c]Max-Planck-Institut für Eisenforschung, Max-Planck-Straße 1, 40237 Düsseldorf, Germany
†Electronic supplementary information (ESI) available. See DOI: 10.1039/d0nr06798a

tempting to explore the effects of combining different types of interstitials simultaneously to reap multiple benefits.

Metals with a BCC crystal structure generally have a higher strength than FCC metals, but are less ductile at room temperature,[25] making them difficult to process and limiting their industrial applications.[26] In contrast, BCC HEAs have been shown to have superior high-temperature performance and also maintain good room-temperature plasticity.[27] This has been attributed to additional dislocation pathways due to atomic-scale chemical fluctuations along the core of the dislocations.[27] Thus, recent attention has shifted to refractory HEAs (which commonly possess a BCC structure[26]), in an effort to produce materials with thermally stable microstructures and temperature-insensitive mechanical properties. Their high melting points and excellent softening resistance[28] surpassing those of the most superior superalloys[29] make them ideal for high temperature applications in aerospace, petrochemical, nuclear, and power generation sectors.[27,29] For example, it is desirable to circumvent the need to use costly, brittle ceramic thermal barrier coatings on aircraft parts subject to high temperatures.[27] It is thus logical to exploit the integration of metastability engineering and interstitial effects among others to improve the room temperature ductility of BCC HEAs while maintaining their high strength.

Motivated by these considerations, an iHEA with a BCC structure was prepared using solid-state synthesis. Nanoindentation, *in situ* micropillar compression testing, atom probe tomography (APT), along with a range of complementary electron microscopy techniques (*e.g.*, scanning transition electron microscopy (STEM), electron backscatter diffraction (EBSD), transmission Kikuchi diffraction (TKD), precession electron diffraction (PED) mapping), were employed to determine the mechanical properties and ascertain the structural characteristics and deformation mechanisms of the alloy. The roles of TRIP and TWIP effects, compositional fluctuations, grain boundary engineering, grain refinement, and nanolaminate strain partitioning were revealed in simultaneously enhancing the strength and ductility of this alloy.

2. Experimental

The FeMnCoCr-based alloy was prepared by closed field unbalanced magnetron sputtering ion plating onto AISI M2 high speed steel substrates (UDP650 magnetron sputtering system, Teer Coatings Ltd, UK). Tool steel of HRC 60 was used as substrates, which were finely polished to an average roughness of 0.03 μm, degreased, ultrasonically cleaned, and subsequently blown dry in flowing nitrogen gas. One $Fe_{53}Mn_{25}Co_{10}Cr_{10}B_{1.4}O_{0.3}C_{0.3}$ alloy target (China Material Technology Co. Ltd) with purity of >99.9% and dimensions of $345 \times 145 \times 5\ mm^3$ was used for the deposition. The substrates were stationary during deposition, and the target-to-substrate distance was fixed at 170 mm. The substrate holder was biased with pulsed DC at a frequency of 250 kHz. The vacuum chamber was pumped down to a background pressure of $<2 \times$

10^{-6} Torr by controlling the flow rate of Ar (50 sccm). The DC current applied to the alloy target was fixed at 4.0 A (sputtering power 1.5 kW). The sample preparation comprises two major steps: plasma ion cleaning (−450 V bias, 30 min), and thin film deposition (−20 V bias, 14 min). Ion etching of the steel substrates at the first stage was used to remove the oxide layer and contaminants on the substrate surface. No external heating was used during thin film deposition.

A nanoindentation system (Fischer-Cripps Laboratories IBIS Nanoindenter, Australia) equipped with a Berkovich indenter was used to measure mechanical properties, *viz.* hardness (H) and modulus of elasticity (E) in a direction parallel to the thin film growth. Calibration of this instrument was routinely performed with a standard fused quartz specimen (with a reduced elastic modulus of 69 GPa). The load function consisted of loading up to 50 mN, and then unloading. The penetration depth corresponded to about 10% of the total film thickness to minimise the effect of the substrates. The hardness and modulus were calculated using the Oliver–Pharr method.[30] The reported mean values and standard deviations are from twenty indentation measurements. In order to prepare deformed samples for STEM analysis, a spherical indenter of 5 μm in radius (Synton-MDP, Switzerland) was used for indentation at loads of 200 and 400 mN. Micro-pillars with a diameter of 2 μm and an aspect ratio of 2.5 were fabricated using a dual beam focussed ion beam (FIB)/scanning electron microscope (SEM) (Thermo Fisher Scientific Helios Nanolab 600, USA). The beam current was reduced to 28 pA at the final milling step to minimize FIB damage. The micropillar compression tests were conducted inside a SEM chamber using the Hysitron PI 88 SEM PicoIndenter (Bruker, USA) with a 5 μm diameter flat-tip indenter. The load-displacement curves were corrected for instrument and substrate compliances,[31] before being converted into engineering stress–strain curves. The data was subsequently converted into true-stress strain curves using the equations and methodology outlined by Greer *et al.*[32] Ten micro-pillars were tested to ensure the reliability and reproducibility of the results.

To prepare lamellae for transmission electron microscopy (TEM) and STEM analysis, cross-sections of iHEA thin films before and after loading were lifted out by FIB and milled down to a thickness of ~50 nm. PED assisted orientation mapping analysis was performed on a TEM (JEM-2200FS, JEOL) equipped with ASTAR (Nanomegas). A probe of less than 1 nm in diameter was used in the nano-beam diffraction mode with a condenser aperture size of 20 μm. The precession frequency of 100 Hz and the precession angle of 0.5° were applied during the nanobeam scanning. A camera length of 15 cm was applied with a scanning step size of 1 nm. All diffraction patterns were recorded by a high-speed stingray CCD camera. The diffraction pattern indexing was performed by template matching method using the ASTAR software package. Diffraction templates of BCC, FCC and HCP phases were generated for template matching using lattice parameters of $a = 0.289$ nm for BCC, $a = 0.353$ nm for FCC, and $a = 0.250$ nm; $c =$

0.408 nm for HCP. Angular difference between adjacent diffraction templates was ~1°. The orientation data volumes were then exported and converted to the format compatible to the orientation imaging analysis software (TSL OIM™, EDAX Inc.). A grain dilation clean up procedure (3° tolerance angle, minimum 5 pixels) was performed three times carefully for noise reduction. Tolerance angle was set as 3° for grain size measurement and phase indexing.

STEM imaging and spectroscopy were performed on Titan Themis microscopes (Thermo Fisher Scientific, USA) operated at 200 kV. Aberration correction of the condenser lenses defines a STEM probe size of <0.1 nm. Atomic number contrast images were collected using the high angle annular dark field (HAADF) detectors. Energy dispersive X-ray spectroscopy (EDS) mapping was performed at 200 kV. Electron energy loss spectroscopy (EELS) spectrum imaging was performed at 300 kV using a GIF Quantum spectrometer (Gatan, USA). Multivariate statistical analysis highlights the spatial variation of different EELS ionisation edges.[34]

APT tips were also prepared using FIB, in which the final stages of sharpening and polishing were conducted at low currents to remove any damaged layers. The chemical composition through the grain boundary in the tip was investigated using APT analysis software (LEAP 5096XR, Cameca Inc.). All measurements were performed in the voltage-pulsing mode at a detection rate of 0.50%, pulse fraction of 15%, pulse repetition rate of 200 kHz, temperature of 70 K, and at a pressure below 10^{-8} Pa.
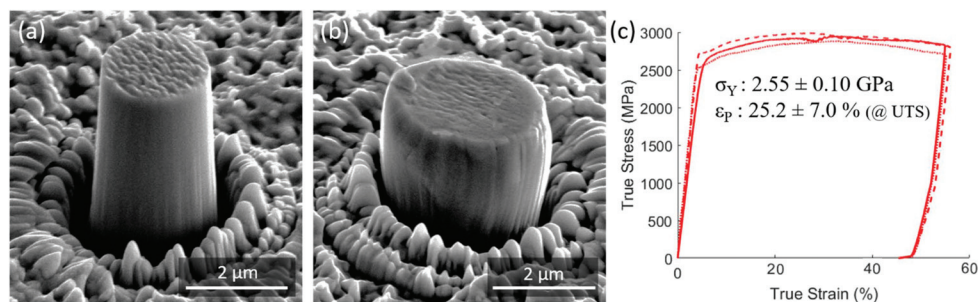
3. Results

The as-deposited alloy has a columnar structure with an average grain width of about 75 nm (Fig. 1a). The microstructure is homogenous and free of porosity or discontinuous regions. The alloy composition was determined by APT as $Fe_{51.2}Mn_{24.3}Co_{11.9}Cr_{10.1}O_{1.4}C_{0.3}B_{0.2}$, with the remaining balance as trace amounts of Al, Si, Ni, P and V. The EDS data (Fig. 1f–j) reveals compositional fluctuations throughout the thin film, further corroborated by APT, which provides three-dimensional compositional mapping via the concentration profile in Fig. 1c (for the region of interest as depicted in Fig. 1b). The APT data shows an inverse relationship between iron and manganese (as seen more prominently in Fig. S2†), and interstitial elements of oxygen, boron, and carbon, segregating to the grain boundaries, and reaching compositions above 4 at%, 0.7 at% and 1.2 at%, respectively. TKD was used for phase characterisation, indicating that the crystal structure is dominated by BCC (space group $Im\bar{3}m$) (Fig. 1d) and the inverse pole figure reveals the orientation of the grains (Fig. 1e). The EBSD results and diffraction pattern analysis in Fig. S1d† further confirm that the as-deposited sample exhibits a BCC structure, with no planar defects such as stacking faults or twin boundaries detected.

Micropillar compression testing (Fig. 2) reveals a high yield strength of 2.55 ± 0.10 GPa, with an appreciable ductility; the pillar was compressed until the pre-set displacement value was reached, and thus, a compressive strain at failure value is not
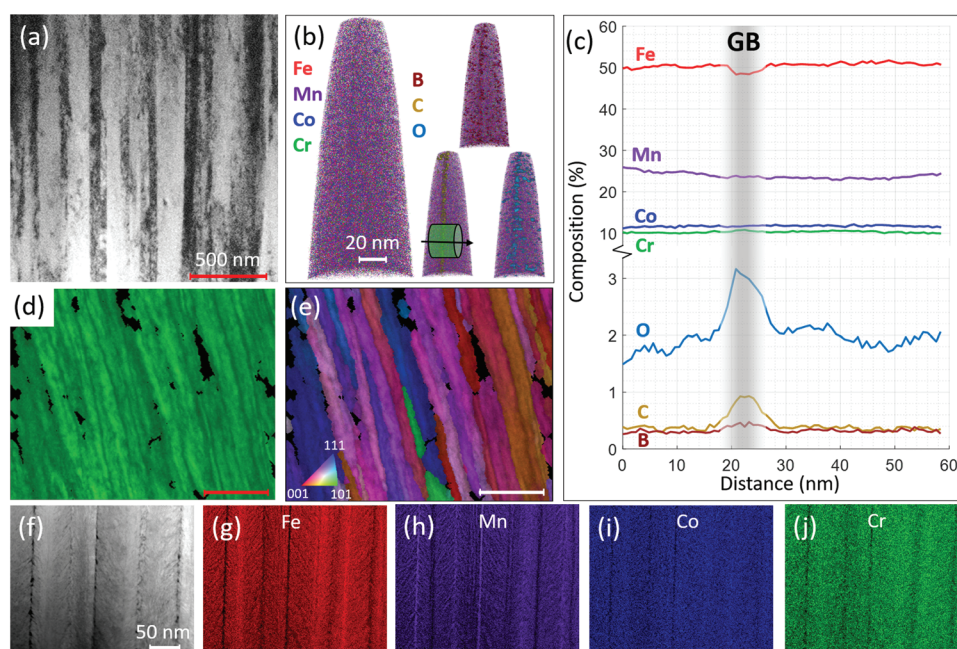
Fig. 1 Microstructural and compositional analysis of as-synthesised iHEA; (a) bright-field transmission electron microscope image showing a columnar structure with the grain width varying between 30 nm and 90 nm, (b) atom probe tomography reconstruction (left) showing Fe, Mn, Co and Cr, with B (0.7% threshold), C (1.2% threshold) and O (4.0% threshold) isosurfaces (right), (c) 1D concentration line profiles displaying elemental segregation around the grain boundary (GB) along the arrow integrating over the cylinder cross section shown in (b), (d) transmission Kikuchi diffraction data showing phase map (where green indicates the BCC phase), with (e) corresponding inverse pole figure showing grain orientations, and (f) energy-dispersive spectroscopy mapping of (g) Fe, (h) Mn, (i) Co and (j) Cr.

Fig. 2 Micropillar compression testing results. The pillar in a pre- and post-mortem state are respectively shown in (a) and (b), with corresponding true stress−strain curves and measured mechanical properties shown in (c). Failure did not occur under compressive load in the present study, and thus, here the ductility is conservatively reported as the plastic strain at the highest compressive stress.

available. Instead, a plastic strain value of 25.2 ± 7.0% was obtained at the highest compressive stress and was later used for comparison purposes. Nanoindentation tests produce a hardness value of 6.2 ± 0.3 GPa and elastic modulus of 205 ± 7 GPa at a load of 50 mN to satisfy the so-called '10% coating thickness rule'.[33] The load-displacement curves are shown in Fig. S3a,† with the deformation impression shown in Fig. S3b (surface), and Fig. S3c† (cross-section). To understand the micro-mechanisms underlying the superior mechanical properties, PED mapping and STEM analysis was conducted of the samples deformed by nanoindentation under two different loads, 200 and 400 mN. The mapping of crystal structure *via* PED mapping in regions of interest (indicated in Fig. 3a and d) located just below the indent are shown in Fig. 3b and f, for loads of 200 and 400 mN, respectively, indicating that deformation induced phase transformation from BCC into HCP, and then HCP to FCC phases occurs. Grain refinement and

rotation, a grain boundary-mediated deformation process,[24] is also evident from the varying orientations shown in the IPFs in Fig. 3c and g. Even under a moderate load of 200 mN, the columnar structure is no longer intact (Fig. 3c), and most of the BCC phase has transformed into HCP, with some FCC emerging (Fig. 3b). When subjected to a higher load of 400 mN, the extent of grain refinement deepens, and the fraction of HCP decreases, with a corresponding increase in FCC (Fig. 3d). The fraction of BCC has also increased, although this is an anomaly stemming primarily from the positioning of the region of interest; PED mapping was conducted further below the indent site in the case of the 400 mN load due to minor milling damage near the platinum–alloy interface, and the fraction of BCC indeed increases further from the indent site.

STEM imaging in the PED mapping region for the heavily deformed sample (shown in Fig. 3d) reveal distinct regions of HCP-dominant (Fig. 4a), dual-phase FCC/HCP (Fig. 4b), and
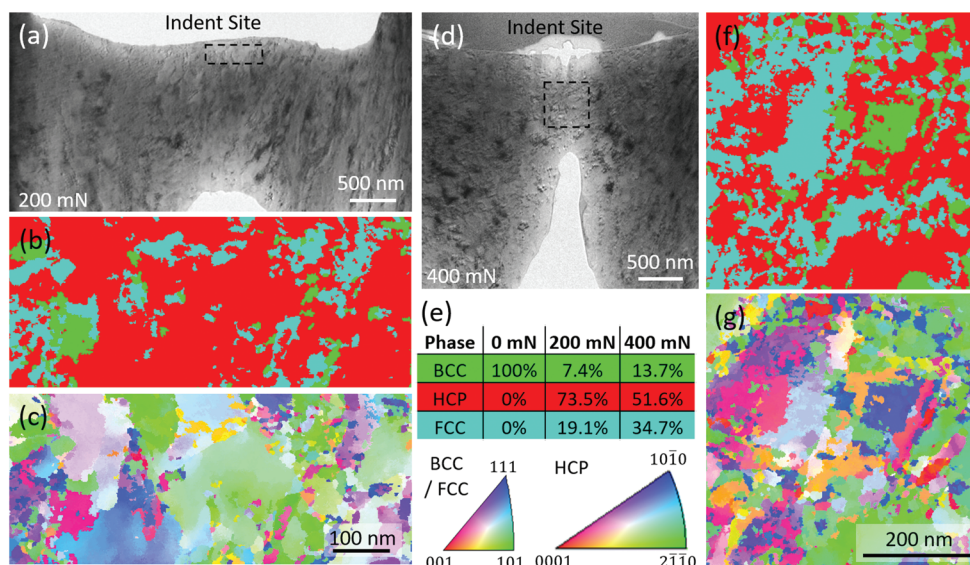
Fig. 3 PED orientation and phase mapping results for the regions analysed indicated by dashed boxes in (a) and (d), corresponding to 200 and 400 mN, respectively. (b) and (f) phase maps showing BCC (green), HCP (red) and FCC (blue) phases, respectively, indicating the evolution of phase transformation during deformation. (e) The fraction transformed at each state, with the phases highlighted in their respective colours per the corresponding diffraction maps (b) and (f). (c) and (g) are inverse pole figure (IPF-Z) orientation maps revealing orientation and distribution of grains within the regions of interest.
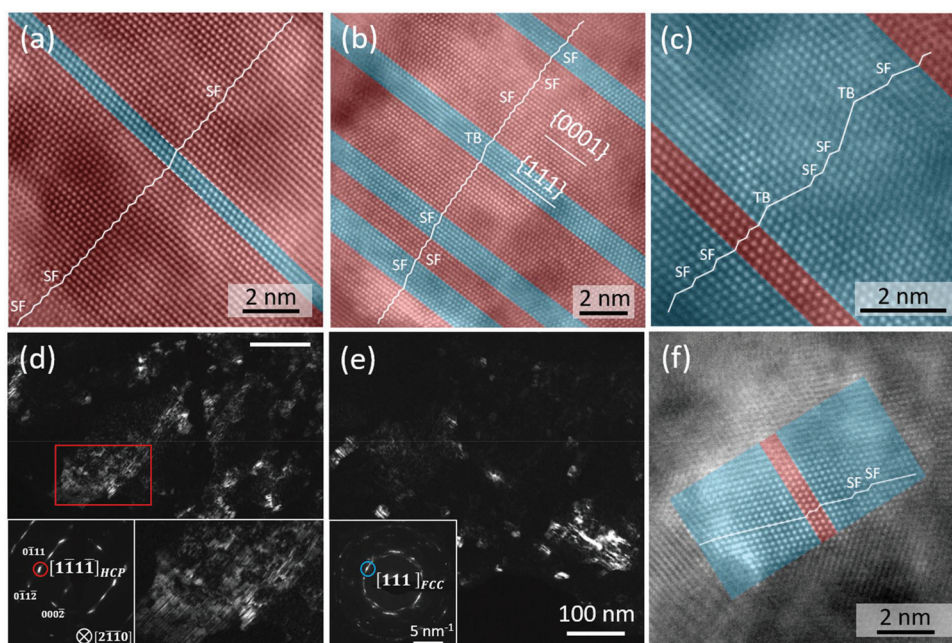
Fig. 4 TEM and STEM data from the 400 mN sample, which was obtained from the same region of analysis shown in Fig. 3d. FCC/HCP lamellae are shown in (a), (b) and (c), where red indicates HCP phase, and blue indicates FCC phase. (a) and (c) Contain HCP and FCC dominant regions, respectively, whereas (b) has relatively high fractions of both. Dark field images are shown in (d) and (e), with the circles in the insets in the bottom-left indicating the selected reflections. A nanograin, predominantly FCC, is shown in (f). Deformation twins are indicated in (b) and (c), indicating that the density of twins increases with higher FCC fractions. The phase transformation from HCP to FCC appears to be mediated *via* stacking faults, manifested by an increase in the density of stacking faults with deformation.

FCC-dominant regions (Fig. 4b). Dark field TEM (Fig. 4d and e) highlights nanograins, and the inset in Fig. 4d shows a close-up of one grain, where parallel stripes can be seen; these stripes are likely the HCP/FCC lamellae as seen in STEM (Fig. 4b). A STEM image of one of the nanograins, after experiencing extensive refinement, is shown in (Fig. 4f). EELS spectral mapping (Fig. 5) is used to characterise the stoichiometry post-deformation in the selected region indicated in Fig. 5a. The alloy matrix (Fig. 5b) is separated from small (<5 nm) segregates of B and O (Fig. 5c), where an enrichment in Mn and Cr, and a depletion in Fe and Co are also identified (Fig. 5d and e).

4. Discussion

4.1. Microstructural development

The iHEA system developed in this study (representation shown in Fig. 7a) exhibits a BCC structure. In comparison, the $Fe_{50}Mn_{30}Co_{10}Cr_{10}$ alloy cast in a vacuum induction furnace exhibits a dual FCC/HCP phase,[17] and B-doped (30 to 300 ppm) $Fe_{50}Mn_{30}Co_{10}Cr_{10}$ possesses an FCC structure.[21] The formation of BCC is likely due to typical processing conditions encountered during magnetron sputtering, such as the lower temperature and pressure, which are drastically different from those experienced during casting.[35] If subjected to a higher temperature and pressure, it is possible that the innate phase would contain some combination of FCC and HCP.[36]
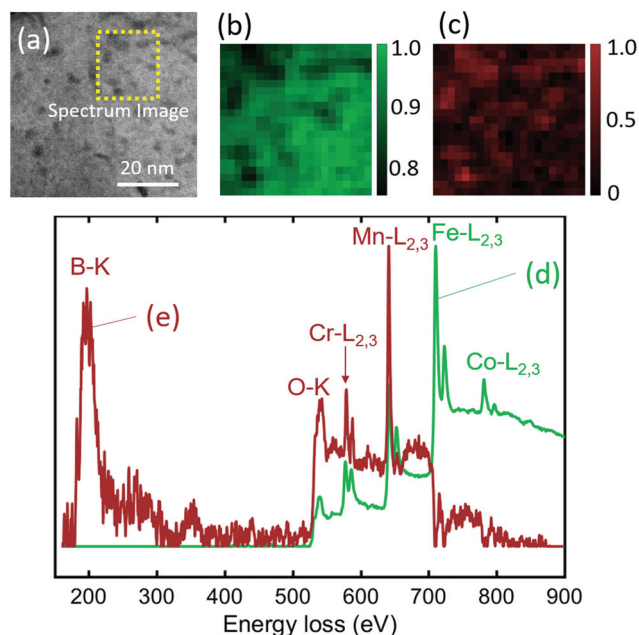
Fig. 5 The EELS spectrum image dataset (shown in (a)) was decomposed by non-negative matrix factorization[34] into two major spectral components: (d) and (e), with their corresponding weighting maps in (b) and (c). The component in green (b, d) corresponds spatially to the matrix alloy CrMnFeCo. The component in mahogany (c, e) corresponds spatially to the small regions with dark HAADF contrast. They are enriched in B, O, Cr, and Mn, and more depleted in Fe and Co. A further component characterising C signal from surface hydrocarbon contaminant is not shown.

Notably, Li *et al.*[17] induced the formation of metal carbides (in the form of $M_{23}C_6$) with a nominal composition of $Fe_{49.63}Mn_{27.27}Co_{11.65}Cr_{10.86}C_{0.59}$, where approximately 0.39 at% of carbon is in the matrix, and 19.46 at% within the carbides, and the interface of the nanocarbide and matrix is on the order of 5 nm. In the present study, the GB region is of a similar scale, and also exhibits an increase in carbon concentration, though no carbides were formed, as the maximum composition of C does not exceed 1.2 at%, *cf.* 19.46 at%.[17] Furthermore, the amount of boron in the new alloy sample (0.2 at%) is much higher than that used by Seol *et al.*,[21] who found that at 100 ppm (by weight) and above, secondary boron-rich phases would form. The formation of such brittle compounds is undesirable, due to the associated reduction in ductility and propensity for crack initiation. Surprisingly, no secondary phases were formed despite having boron concentrations well above 300 ppm (by weight). This might be due to the fact that the atoms are deposited more uniformly during magnetron sputtering,[37] and despite segregating at the GB, boron is distributed evenly in other regions. Boron GB decoration of this polycrystalline material might be driven by the Gibbsian reduction in grain boundary energy.[21]

4.2. Mechanical properties

The yield strength of 2.55 GPa is more than double that reported for as-cast HEAs with or without boron doping,[21] and indeed for other iHEAs such as as-cast C-doped iHEA.[22] Compared to other HEA and medium entropy alloy (MEA) coatings,[38,39] the new alloy also shows a decent hardness value of 6.2 GPa. The appreciable deformability is evidenced by a relatively high true plastic strain value (determined at the highest compressive stress) of 25.2%, and visually by the high degree of plastic flow (barrelling) demonstrated by micropillar

compression (Fig. 2b), and also manifested in the indentation impression (Fig. S3b and c†).[40] This is a particularly impressive result, considering BCC-structured HEAs generally have poor room temperature compressibility.[26] As per Fig. 6, the alloy displays an excellent combination of strength and ductility. The yield strength of a material is directly related to the moveability of dislocations.[41] In addition to the fine grain size which impedes dislocation motion, the presence of interstitial atoms are also responsible for the high yield strength.[42] Specifically, boron addition is used to promote grain refinement and grain boundary strength, thereby enhancing the load-bearing capacity of the alloy without altering the deformation mode.[21] Oxygen has been used to improve the mechanical properties of materials by increasing lattice distortion in the matrix and through concentrating in grain boundary regions.[43] By segregating to GBs, oxygen enrichment is believed to promote grain refinement *via* reducing the GB energy,[43] giving rise to enhanced strength in this work. Lastly, carbon has a propensity to accumulate at grain boundaries,[44,45] and was found responsible for the increase of the Hall-Petch coefficient of a ferritic steel[46] and doubling the yield strength of a FCC FeNiMnAlCr HEA.[47] In this work, carbon concentration was also found to increase at the grain boundaries, thereby contributing to grain boundary strengthening.

4.3. Deformation mechanisms

The deformability observed in the new alloy is surprising and can be attributed to a cascade of events that include grain refinement, phase transformation and deformation twinning, by which the number of physical barriers that impede dislocation motion are markedly increased and subsequently increase the flow stress.[48] Recently, TRIP assisted deformation of HEAs with FCC and BCC structures have been studied.[49]
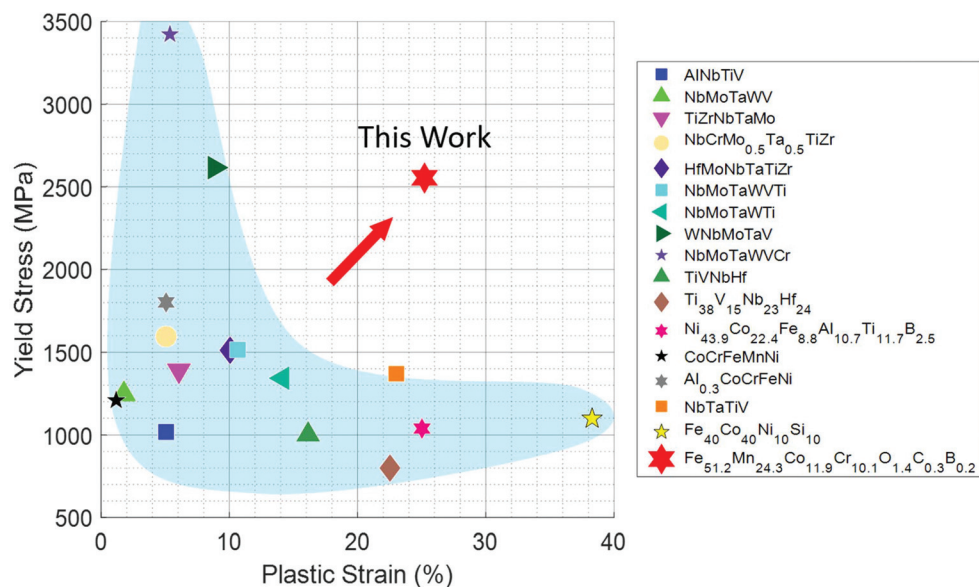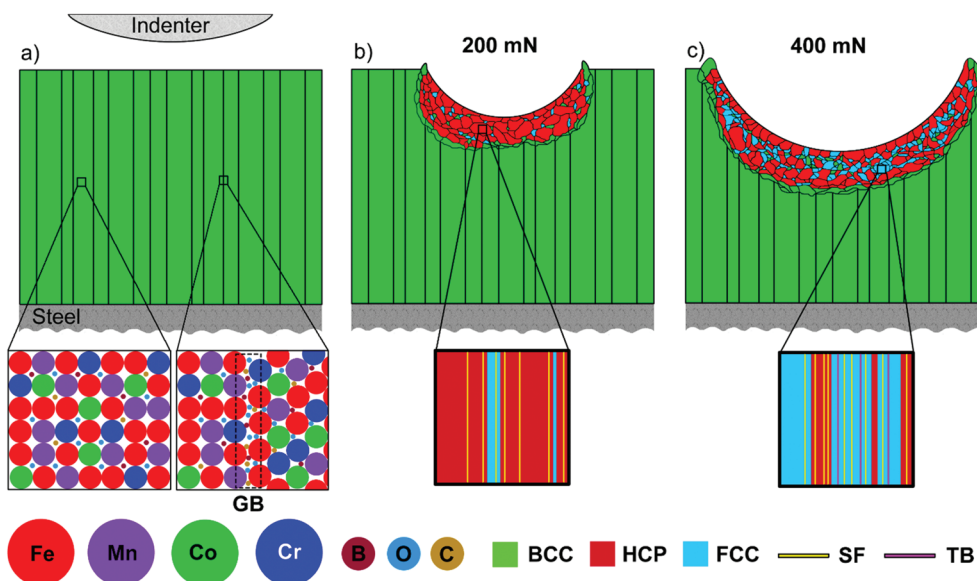

Fig. 6 The yield strength and plastic strain at failure obtained for a range of high-strength HEAs at room temperature. Data and references are provided in Table 1 (see ESI†).

Fig. 7 Generalised deformation mechanism of the alloy thin film: (a) pristine columnar BCC structure, with atomic structure representations shown below from inside a grain (left), and through a grain boundary decorated with interstitial atoms (right); (b) partial deformation caused by 200 mN showing the onset of grain refinement, deformation induced phase transformation from BCC to HCP and some ensuing FCC, with a nanoscale representation below showing some FCC lamellae being nucleated *via* deformation induced stacking faults (SF), and, (c) heavy deformation at 400 mN, showing a higher fraction of FCC, and the formation of twin boundaries (TB) due to deformation twinning within the FCC phase at the nanoscale.

The exceptionally high strain hardening rate in the TaHfZrTi HEA was attributed to the phase transformation from BCC to HCP.[20] However, the two-step phase transformation (*i.e.*, BCC to HCP to FCC shown in Fig. 7a–c) revealed in this study and its effect on plasticity has never been reported in HEAs, and there is limited discussion surrounding this mechanism in literature.[50,51] Metals undergoing phase transformations can be described in terms of crystallographic orientation relations between dilations and contractions to the lattice of the original and newly formed phases.[52] Wang *et al.*[53] conducted molecular dynamics (MD) simulations of BCC iron under compression. According to the MD simulations,[53] the HCP nucleation planes belong to $\{110\}_{BCC}$ and are parallel to the [100], [010], and [001] directions, and proceeds first *via* atoms shearing in the $(\bar{1}12)$ planes in the $[\bar{1}1\bar{1}]$ direction and compressing in the $[1\bar{1}\bar{2}]$ direction to produce a hexagon, followed by alternate (110) planes shuffling relatively along the $[\bar{1}10]$ direction to create the HCP structure. This is consistent with the orientation relationship in the present study, which observes a Pitsch-Schrader orientation relationship[54] between the BCC and HCP phases evidenced in STEM imaging and FFT analysis shown in Fig. S4,† *viz.* $[2\bar{1}\bar{1}0]_{HCP}\|[001]_{BCC}$.

The phase transformation from HCP to FCC is understood to take place *via* the gliding of Shockley partial dislocations on the alternative basal planes.[55] Therefore, once the phase transformation from BCC to HCP has occurred, a low SFE is necessary in mediating this process.[36] The SFE was found to decrease by lowering Mn content in the non-equiatomic $Cr_{10}Mn_xFe_{70-x}Co_{10}Ni_{10}$ HEAs.[56] The presence of ~25% Mn is a critical threshold in regulating the TRIP behaviour,[17] since at higher compositions of Mn the resultant higher SFE would

block the HCP to FCC pathway. In addition to contributing to increased lattice distortion, the addition of oxygen[43] and carbon[17] also served to lower the SFE which in turn affected the phase stability of the HCP phase. Therefore, the presence of C and O contributes towards the HCP to FCC phase transformation activation.

In addition, following the transformation from BCC to HCP, deformation-induced stacking faults appear in the HCP structure (Fig. 7b), which have been found to act as embryos for the nucleation of FCC phase.[55] Induced planar defects can facilitate a phase transformation from HCP to FCC *via* the formation of stacking faults on the (0001) basal planes. The fraction of FCC increases steadily accompanied by a corresponding decrease of HCP under further loading, creating regions of distinct micro-constituents (Fig. 7c), ranging from untransformed BCC (Fig. S1c†), FCC (Fig. 4c), HCP (Fig. 4a), and some mixed (Fig. 4b), with the nucleation of FCC occurring *via* stacking fault formation.[53]

The two-step phase transformation observed here not only imparts significant plasticity, but also generates numerous phase boundaries. A phase boundary is analogous to a grain boundary in terms of hardening *via* impeding dislocation motions. Consequently, phase transformation dynamically refines the microstructure (Fig. 7c) and reduces the mean free path for dislocation slip, one of the primary carriers of plastic deformation, inducing the so-called "dynamic Hall-Petch" effect[57] and at the same time prolonging the extent of work hardening.[58] As the atomic packing factor of BCC is lower than that of HCP, the decrease in volume neutralises some residual compressive strain, leading to structural dissipation and strain relaxation,[59] thereby contributing to ductility. It

should be noted, high stress concentration in a local region induced by accumulation of the transformed HCP phase could lead to mechanical instability. To avoid this, the stress concentration is relaxed through the second step of phase transformation from HCP to FCC, which accounts for additional plasticity. Having both HCP and FCC present enhances the strength and ductility of the new alloy simultaneously, as the softer FCC phase serves as an agent to increase ductility, whereas the harder HCP phase acts as structural support and also to impede dislocation motion.[36] Moreover, the presence of multiple phases induces a composite effect due to the interleaved phases,[20] as well as strain partitioning,[60] whereby the combination of phase transformation from BCC to HCP and size confinement (due to the nanolaminate structure) work to increase the strain-hardening capacity. Softening also occurs concurrently as a result of FCC formation, resulting in a net near-zero hardening rate. Lastly, deformation twinning is also observed in the FCC phase (Fig. 4c). The extra strength induced by twinning is due to ensuing dislocation pileups at the twin boundaries, and is typically activated when higher stress states are achieved.[58] Deformation twinning results in a continuously self-refining structure that provides a high work hardening capacity,[36] thereby contributing to the material's excellent mechanical properties. A simplified deformation process, highlighting phase and planar defects at each stage of deformation, is shown in Fig. 7.

HEAs are known to possess severe lattice distortion and therefore high strength,[61] and further strengthening has been induced here *via* the incorporation of interstitial atoms B, O and C, but local fluctuations in chemistry and short-range ordering has been introduced in the post-deformed state to further strengthen the iHEA during deformation. Locally enriched regions of B, O, Cr and Mn, yet depleted in Fe and Co (and *vice versa*) exist, are expected to offer strengthening on shorter length scales than in the undeformed state (as per Fig. 5). These small discrete clusters of elements reinforce the sample during deformation by causing fluctuations in the lattice strain that impede dislocation glide.[62]

5. Conclusion

FeMnCoCr-based iHEA with BCC structure was prepared by closed field unbalanced magnetron sputtering ion plating. An exceptional combination of high yield strength ($\sigma_Y \sim 2.55$ GPa) and ductility ($\varepsilon_P \sim 25.2\%$) was achieved by uniting multiple design strategies. The key findings can be summarised as follows:

1. The unique abilities of three interstitial atoms (B, C and O) were harnessed to enhance the phase stability and facilitate the grain refinement process during deformation.

2. The deformed structure contains highly refined grains, and short-range compositional fluctuations giving rise to appreciable lattice distortions that contribute to strain hardening.

3. The alloy exhibits appreciable ductile behaviour *via* undergoing a two-step phase transformation upon deformation; first from BCC to HCP phase governed by a plane shearing and shuffling mechanism observing a Pitch-Schrader orientation relationship, and then from HCP to FCC phase catalysed by stacking fault formation.

4. The resultant HCP/FCC nanolamellar structure with a high density of planar defects (*i.e.*, stacking faults, twin boundaries and phase boundaries), triggers self-hardening by impeding dislocation motion.

Conflicts of interest

There are no conflicts to declare.

Acknowledgements

References

1 B. Cantor, Multicomponent and High Entropy Alloys, *Entropy*, 2014, **16**, 4749–4768.
2 J. W. Yeh, S. K. Chen, S. J. Lin, J. Y. Gan, T. S. Chin, T. T. Shun, C. H. Tsau and S. Y. Chang, Nanostructured high-entropy alloys with multiple principal elements: Novel alloy design concepts and outcomes, *Adv. Eng. Mater.*, 2004, **6**, 299–303.

3 A. Garzon-Manjon, H. Meyer, D. Grochla, T. Loffler, W. Schuhmann, A. Ludwig and C. Scheu, Controlling the Amorphous and Crystalline State of Multinary Alloy Nanoparticles in An Ionic Liquid, *Nanomaterials*, 2018, **8**(11), 903.

4 B. Gludovatz, A. Hohenwarter, D. Catoor, E. H. Chang, E. P. George and R. O. Ritchie, A fracture-resistant high-entropy alloy for cryogenic applications, *Science*, 2014, **345**, 1153.

5 P. Kozelj, S. Vrtnik, A. Jelen, S. Jazbec, Z. Jaglicic, S. Maiti, M. Feuerbacher, W. Steurer and J. Dolinsek, Discovery of a superconducting high-entropy alloy, *Phys. Rev. Lett.*, 2014, **113**, 107001.

6 F. Otto, A. Dlouhy, C. Somsen, H. Bei, G. Eggeler and E. P. George, The influences of temperature and microstructure on the tensile properties of a CoCrFeMnNi high-entropy alloy, *Acta Mater.*, 2013, **61**(15), 5743–5755.

7 C. Tasan, Y. Deng, K. Pradeep, M. Yao, H. Springer and D. Raabe, Composition Dependence of Phase Stability, Deformation Mechanisms, and Mechanical Properties of the CoCrFeMnNi High-Entropy Alloy System, *JOM*, 2014, **66**, 1993–2001.

8 M. J. Yao, K. G. Pradeep, C. C. Tasan and D. Raabe, A novel, single phase, non-equiatomic FeMnNiCoCr high-entropy alloy with exceptional phase stability and tensile ductility, *Scr. Mater.*, 2014, **72–73**, 5–8.

9 Y. Zhang, T. T. Zuo, Z. Tang, M. C. Gao, K. A. Dahmen, P. K. Liaw and Z. P. Lu, Microstructures and properties of high-entropy alloys, *Prog. Mater. Sci.*, 2014, **61**, 1–93.

10 B. Cantor, I. T. H. Chang, P. Knight and A. J. B. Vincent, Microstructural development in equiatomic multi-component alloys, *Mater. Sci. Eng., A*, 2004, **375–377**, 213–218.

11 E. P. George, D. Raabe and R. O. Ritchie, High-entropy alloys, *Nat. Rev. Mater.*, 2019, **4**, 515–534.

12 Y. Deng, C. C. Tasan, K. G. Pradeep, H. Springer, A. Kostka and D. Raabe, Design of a twinning-induced plasticity high entropy alloy, *Acta Mater.*, 2015, **94**, 124–133.

13 G. Laplanche, A. Kostka, C. Reinhart, J. Hunfeld, G. Eggeler and E. P. George, Reasons for the superior mechanical properties of medium-entropy CrCoNi compared to high-entropy CrMnFeCoNi, *Acta Mater.*, 2017, **128**, 292–303.

14 F. Otto, A. Dlouhy, K. G. Pradeep, M. Kubenova, D. Raabe, G. Eggeler and E. P. George, Decomposition of the single-phase high-entropy alloy CrMnFeCoNi after prolonged anneals at intermediate temperatures, *Acta Mater.*, 2016, **112**, 40–52.

15 K. G. Pradeep, C. C. Tasan, M. J. Yao, Y. Deng, H. Springer and D. Raabe, Non-equiatomic high entropy alloys: Approach towards rapid alloy screening and property-oriented design, *Mater. Sci. Eng., A*, 2015, **648**, 183–192.

16 Y. P. Wang, B. S. Li and H. Z. Fu, Solid Solution or Intermetallics in a High-Entropy Alloy, *Adv. Eng. Mater.*, 2009, **11**, 641–644.

17 Z. Li, K. G. Pradeep, Y. Deng, D. Raabe and C. C. Tasan, Metastable high-entropy dual-phase alloys overcome the strength-ductility trade-off, *Nature*, 2016, **534**, 227–230.

18 E. Ma and X. Wu, Tailoring heterogeneities in high-entropy alloys to promote strength–ductility synergy, *Nat. Commun.*, 2019, **10**, 5623.

19 R. O. Ritchie, The conflicts between strength and toughness, *Nat. Mater.*, 2011, **10**, 817–822.

20 H. Huang, Y. Wu, J. He, H. Wang, X. Liu, K. An, W. Wu and Z. Lu, Phase-Transformation Ductilization of Brittle High-Entropy Alloys via Metastability Engineering, *Adv. Mater.*, 2017, **29**, 1701678.

21 J. B. Seol, J. W. Bae, Z. Li, J. Chan Han, J. G. Kim, D. Raabe and H. S. Kim, Boron doped ultrastrong and ductile high-entropy alloys, *Acta Mater.*, 2018, **151**, 366–376.

22 L. Zhiming, T. Cemal Cem, S. Hauke, G. Baptiste and R. Dierk, Interstitial atoms enable joint twinning and transformation induced plasticity in strong and ductile high-entropy alloys, *Sci. Rep.*, 2017, **7**, 40704.

23 Z. Lei, X. Liu, Y. Wu, H. Wang, S. Jiang, S. Wang, X. Hui, Y. Wu, B. Gault, P. Kontis, D. Raabe, L. Gu, Q. Zhang, H. Chen, H. Wang, J. Liu, K. An, Q. Zeng, T.-G. Nieh and Z. Lu, Enhanced strength and ductility in a high-entropy alloy via ordered oxygen complexes, *Nature*, 2018, **563**, 546–550.

24 J. Hu, Y. N. Shi, X. Sauvage, G. Sha and K. Lu, Grain boundary stability governs hardening and softening in extremely fine nanograined metals, *Science*, 2017, **355**, 1292–1296.

25 S. Guo, C. Ng, J. Lu and C. T. Liu, Effect of valence electron concentration on stability of fcc or bcc phase in high entropy alloys, *J. Appl. Phys.*, 2011, **109**, 103505.

26 V. Soni, O. N. Senkov, B. Gwalani, D. B. Miracle and R. Banerjee, Microstructural Design for Improving Ductility of An Initially Brittle Refractory High Entropy Alloy, *Sci. Rep.*, 2018, **8**, 8816.

27 J. Cairney, A rival to superalloys at high temperatures, *Science*, 2020, **370**, 37–38.

28 S. Wei, S. Kim, J. Y. Kang, Y. Zhang, T. Furuhara, E. S. Park and C. C. Tasan, Natural-mixing guided design of refractory high-entropy alloys with as-cast tensile ductility, *Nat. Mater.*, 2020, 1–7.

29 F. Wang, G. H. Balbus, S. Xu, Y. Su, J. Shin, P. F. Rottmann, K. E. Knipling, J.-C. Stinville, L. H. Mills, O. N. Senkov, I. J. Beyerlein, T. M. Pollock and D. S. Gianola, Multiplicity of dislocation pathways in a refractory multiprincipal element alloy, *Science*, 2020, **370**, 95–101.

30 W. C. Oliver, An improved technique for determining hardness and elastic modulus using load and displacement sensing indentation experiments, *J. Mater. Res.*, 1992, **7**, 1564–1583.

31 H. Zhang, B. E. Schuster, Q. Wei and K. T. Ramesh, The design of accurate micro-compression experiments, *Scr. Mater.*, 2006, **54**, 181–186.

32 J. R. Greer, W. C. Oliver and W. D. Nix, Size dependence of mechanical properties of gold at the micron scale in the absence of strain gradients, *Acta Mater.*, 2005, **53**, 1821–1830.

33 A. C. Fischer-Cripps, *Nanoindentation*, Springer, 2013.

34 S. Zhang and C. Scheu, Evaluation of EELS spectrum imaging data by spectral components and factors from multivariate analysis, *Microscopy*, 2018, **67**(Suppl. 1), i133–i141.

35 L. R. Shaginyan, J. G. Han, V. R. Shaginyan and J. Musil, Evolution of film temperature during magnetron sputtering, *J. Vac. Sci. Technol., A*, 2006, **24**, 1083–1090.

36 W. Lu, C. H. Liebscher, G. Dehm, D. Raabe and Z. Li, Bidirectional Transformation Enables Hierarchical Nanolaminate Dual-Phase High-Entropy Alloys, *Adv. Mater.*, 2018, **30**, 1804727.

37 B. R. Braeckman, F. Boydens, H. Hidalgo, P. Dutheil, M. Jullien, A. L. Thomann and D. Depla, High entropy alloy thin films deposited by magnetron sputtering of powder targets, *Thin Solid Films*, 2015, **580**, 71–76.

38 Y. Chen, Z. Zhou, P. Munroe and Z. Xie, Hierarchical nanostructure of CrCoNi film underlying its remarkable mechanical strength, *Appl. Phys. Lett.*, 2018, **113**, 8.

39 S. J. Tsianikas, Y. Chen and Z. Xie, Deciphering deformation mechanisms of hierarchical dual-phase CrCoNi coatings, *J. Mater. Sci. Technol.*, 2020, **39**, 7–13.

40 J. R. Trelewicz and C. Schuh, The Hall-Petch breakdown in nanocrystalline metals: A crossover to glass-like deformation, *Acta Mater.*, 2007, **55**(17), 5948–5958.

41 K. Lu, Stabilizing nanostructures in metals using grain and twin boundary architectures, *Nat. Rev. Mater.*, 2016, **1**, 16019.

42 D. Raabe, M. Herbig, S. Sandlöbes, Y. Li, D. Tytko, M. Kuzmina, D. Ponge and P. P. Choi, Grain boundary segregation engineering in metallic alloys: A pathway to the design of interfaces, *Curr. Opin. Solid State Mater. Sci.*, 2014, **18**, 253–261.

43 J. Guo, M. J. Duarte, Y. Zhang, A. Bachmaier, C. Gammer, G. Dehm, R. Pippan and Z. Zhang, Oxygen-mediated deformation and grain refinement in Cu-Fe nanocrystalline alloys, *Acta Mater.*, 2019, **166**, 281–293.

44 J. Chen, Z. Yao, X. Wang, Y. Lu, X. Wang, Y. Liu and X. Fan, Effect of C content on microstructure and tensile properties of as-cast CoCrFeMnNi high entropy alloy, *Mater. Chem. Phys.*, 2018, **210**, 136–145.

45 L. Li, Z. Li, A. Kwiatkowski da Silva, Z. Peng, H. Zhao, B. Gault and D. Raabe, Segregation-driven grain boundary spinodal decomposition as a pathway for phase nucleation in a high-entropy alloy, *Acta Mater.*, 2019, **178**, 1–9.

46 S. Araki, K. Mashima, T. Masumura, T. Tsuchiyama, S. Takaki and T. Ohmura, Effect of grain boundary segregation of carbon on critical grain boundary strength of ferritic steel, *Scr. Mater.*, 2019, **169**, 38–41.

47 Z. Wang and I. Baker, Interstitial strengthening of a f.c.c. FeNiMnAlCr high entropy alloy, *Mater. Lett.*, 2016, **180**, 153–156.

48 K. Lu, L. Lu and S. Suresh, Strengthening Materials by Engineering Coherent Internal Boundaries at the Nanoscale, *Science*, 2009, **324**, 349.

49 Y. H. Jo, W. M. Choi, D. G. Kim, A. Zargaran, S. S. Sohn, H. S. Kim, B. J. Lee, N. J. Kim and S. Lee, FCC to BCC transformation-induced plasticity based on thermodynamic phase stability in novel V10Cr10Fe45CoxNi35−x medium-entropy alloys, *Sci. Rep.*, 2019, **9**, 2948.

50 Y. Ivanisenko, I. Maclaren, R. Z. Valiev and H.-J. Fecht, The First Observation of a Shear-Induced bcc -> fcc Transformation in Nanocrystalline Ferrite, *Adv. Eng. Mater.*, 2005, **7**, 1011–1014.

51 S. J. Wang, H. Wang, K. Du, W. Zhang, M. L. Sui and S. X. Mao, Deformation-induced structural transition in body-centred cubic molybdenum, *Nat. Commun.*, 2014, **5**, 3433.

52 W. G. Burgers, On the process of transition of the cubic-body-centered modification into the hexagonal-close-packed modification of zirconium, *Physica*, 1934, **1**, 561–586.

53 B. T. Wang, J. L. Shao, G. C. Zhang, W. D. Li and P. Zhang, Nucleation of hcp and fcc phases in bcc iron under uniform compression: classical molecular dynamics simulations, *J. Phys.: Condens. Matter*, 2010, **22**, 435404.

54 P. Wang, Y. Bu, J. Liu, Q. Li, H. Wang and W. Yang, Atomic deformation mechanism and interface toughening in metastable high entropy alloy, *Mater. Today*, 2020, **37**, 64–73.

55 C. Hitzenberger, H. P. Karnthaler and A. Korner, In situ tem study of the h.c.p. to f.c.c. martensitic phase transformation in CoNi single crystals, *Acta Metall.*, 1988, **36**, 2719–2728.

56 W. Guo, J. Su, W. Lu, C. H. Liebscher, C. Kirchlechner, Y. Ikeda, F. Körmann, X. Liu, Y. Xue and G. Dehm, Dislocation-induced breakthrough of strength and ductility trade-off in a non-equiatomic high-entropy alloy, *Acta Mater.*, 2020, **185**, 45–54.

57 H. Idrissi, K. Renard, D. Schryvers and P. J. Jacques, On the relationship between the twin internal structure and the work-hardening rate of TWIP steels, *Scr. Mater.*, 2010, **63**, 961–964.

58 Y. Wang, M. Chen, F. Zhou and E. Ma, High tensile ductility in a nanostructured metal, *Nature*, 2002, **419**, 912–915.

59 J. Li, Q. Fang, B. Liu and Y. Liu, Transformation induced softening and plasticity in high entropy alloys, *Acta Mater.*, 2018, **147**, 35–41.

60 M. M. Wang, C. C. Tasan, D. Ponge, A. C. Dippel and D. Raabe, Nanolaminate transformation-induced plas-

ticity–twinning-induced plasticity steel with dynamic strain partitioning and enhanced damage resistance, *Acta Mater.*, 2015, **85**, 216–228.

61 J. W. Yeh, Recent progress in high-entropy alloys, *Ann. Chim.: Sci. Mater.*, 2006, **31**, 633–648.

62 Q. Ding, Y. Zhang, X. Chen, X. Fu, D. Chen, S. Chen, L. Gu, F. Wei, H. Bei, Y. Gao, M. Wen, J. Li, Z. Zhang, T. Zhu, R. O. Ritchie and Q. Yu, Tuning element distribution, structure and properties by composition in high-entropy alloys, *Nature*, 2019, **574**, 223–227.

Chapter 5

Forging strength-ductility unity in a high entropy steel

Statement of Authorship

Title of Paper	Forging strength-ductility unity in a high entropy steel
Publication Status	☑ Published ☐ Accepted for Publication ☐ Submitted for Publication ☐ Unpublished and Unsubmitted work written in manuscript style
Publication Details	S. J. Tsianikas, Y. Chen, J. Jeong, S. Zhang, Z. Xie (2022). "Forging strength-ductility unity in a high entropy steel", Journal of Materials Science & Technology 113, 158-165.

Principal Author

Name of Principal Author (Candidate)	Simon Tsianikas
Contribution to the Paper	Acquiring Data, Knowledge, Analysis, Drafting
Overall percentage (%)	70%
Certification:	This paper reports on original research I conducted during the period of my Higher Degree by Research candidature and is not subject to any obligations or contractual agreements with a third party that would constrain its inclusion in this thesis. I am the primary author of this paper.
Signature	Date 24/02/2022

Co-Author Contributions

By signing the Statement of Authorship, each author certifies that:

 i. the candidate's stated contribution to the publication is accurate (as detailed above);

 ii. permission is granted for the candidate in include the publication in the thesis; and

 iii. the sum of all co-author contributions is equal to 100% less the candidate's stated contribution.

Name of Co-Author	Yujie Chen
Contribution to the Paper	Knowledge, Analysis, Drafting
Signature	Date 24/02/2022

Name of Co-Author	Jiwon Jeong
Contribution to the Paper	Knowledge, Analysis
Signature	Date 13.11.2021

Name of Co-Author	Siyuan Zhang		
Contribution to the Paper	Knowledge, Analysis		
Signature		Date	12.11. 2021

Name of Co-Author	Zonghan Xie		
Contribution to the Paper	Conception, Knowledge, Analysis, Drafting		
Signature		Date	18/2/2022

Forging strength–ductility unity in a high entropy steel

S.J. Tsianikas [a,*], Y. Chen [a,b,**], J. Jeong [c], S. Zhang [c], Z. Xie [a]

[a] *School of Mechanical Engineering, The University of Adelaide, SA 5005, Australia*
[b] *Centre for Advanced Thin Film Materials and Devices, Faculty of Materials and Energy, Southwest University, Chongqing 400715, China*
[c] *Max-Planck-Institut für Eisenforschung, Max-Planck-Straße 1, Düsseldorf 40237, Germany*

ARTICLE INFO

ABSTRACT

$Fe_{72.4}Co_{13.9}Cr_{10.4}Mn_{2.7}B_{0.34}$ high entropy steel was prepared by magnetron sputtering. The alloy exhibits a high yield strength of 2.92 ± 0.36 GPa while achieving appreciable plasticity of $13.7 \pm 1.9\%$ at the ultimate compressive strength (3.37 ± 0.36 GPa). The distribution of iron and chromium shows an unusual, characteristic spinodal-like pattern at the nanometer scale, where compositions of Fe and Cr show strong anticorrelation and vary by as much as 20 at.%. The high strength is largely attributable to the compositional modulations, combined with fine grains with body-centered cubic (BCC) crystal structure, as well as grain boundary segregation of interstitial boron. The impressive plasticity is accommodated by the formation and operation of multiplanar, multicharacter dislocation slips, mediated by coherent interfaces, and controlled by shear bandings. The excellent strength–ductility combination is thus enabled by a range of distinctive strengthening mechanisms, rendering the new alloy a potential candidate for safety-critical, load-bearing structural applications.

© 2022 Published by Elsevier Ltd on behalf of The editorial office of Journal of Materials Science & Technology.

1. Introduction

Since 2014, high- and medium-entropy alloys (HEAs and MEAs, respectively) including high entropy steels (a compositionally complex alloy (CCA) based on Fe [1]) have received increased attention for their outstanding mechanical properties [2–4]. These alloys defy conventional design philosophy, and thus, present the opportunity to tackle previously unsolved challenges in the development of materials [5,6], such as creating high-strength materials without sacrificing ductility [7,8]. Interestingly, BCC HEAs have been shown to have superior high-temperature strength and also maintain good room-temperature plasticity [9]. This has been attributed to additional dislocation pathways due to atomic-scale chemical fluctuations along the core of dislocations [9]. In light of this breakthrough, it is possible to design BCC alloys for load-bearing applications in aerospace and power generation [9]. Recently, a good combination of strength and ductility was achieved in MoNbTi by controlling dislocation motion, via the dominance of non-screw character dislocations and numerous slip planes for dislocation glide [10]. Meanwhile, high entropy steels have achieved

10% weight reduction and possess improved strength and ductility compared to conventional steels [1]. Thus, BCC CCAs have the potential to overcome the limitations of conventional BCC alloys, such as the strength–ductility trade-off.

One of the key features of high entropy alloys is the high extent of lattice distortion resulting from using multiple principal elements with varied atomic radii [2], yielding an enhanced solid solution strengthening effect through restricting dislocation glide [11]. This effect was demonstrated well in a study of the VCoNi alloy [12], through comparison to the already impressive CrCoNi alloy [13–19]; when chromium was replaced with vanadium, an alloy of even higher strength was created, with little sacrifice to ductility. This caused an increase in lattice strain due to the dissimilar atomic radius of vanadium, resulting in a friction stress (quantified by the Peierl's stress) of 383 MPa, three times higher than that of other HEAs [12]. In another study, Mn in the Cantor alloy, i.e., CrMnFeCoNi [20], was substituted with a second-row transition metal element (viz., palladium), which induced pronounced periodic compositional fluctuations [21]. This resulted in the formation of alternating tensile and compressive strain fields at the nanoscale which further improved the yield strength by inhibiting dislocation glide.

Interestingly, compositional fluctuations have been also noted during spinodal decomposition, i.e., the emerging of two phases in a metastable region, which takes place in the central region of the miscibility gap and is driven by the minimization of free energy

---

* Corresponding author.
** Corresponding author at: School of Mechanical Engineering, The University of Adelaide, SA 5005, Australia.
E-mail addresses: simon.tsianikas@adelaide.edu.au (S.J. Tsianikas), yujie.chen@adelaide.edu.au (Y. Chen).

via uphill diffusion [22]. This term is derived from the 'spinodal', which marks the apex of the phase boundary whereby a system transitions from a homogenous supersaturated matrix phase into a heterogeneous mixture of two or more phases, with different stoichiometry [23]. Spinodal decomposition was found to improve work-hardening capacity by providing strong diffuse obstacles and introducing antiphase boundaries [24]. The coherency of the different regions helps minimize strain accumulation, meaning that local crack initiation is suppressed [24]. Moreover, it causes a restraining effect on dislocation motion, and thus, enhances strength, with the resistance to dislocation motion being proportional to the intensity of the concentration gradients in the spinodal microstructure [25].

Grain boundaries are ubiquitous in polycrystalline materials and influence the mechanical strength exhibited by materials [26]. Thus, a lot of attention has been given to regulating the grain boundaries as a way of improving the strength of materials. One example of this is grain boundary segregation engineering, where interstitial elements 'decorate' the grain boundaries [27]. This has multiple benefits, such as strengthening interfaces, reducing the probability of catastrophic failure events [28], improving cohesion, and lowering interface energy to stabilize nanocrystals [26]. Grain boundary segregation engineering has been used to simultaneously improve strength and ductility via the addition of boron to a $Fe_{40}Mn_{40}Cr_{10}Co_{10}$ alloy; the yield strength was increased by ~40% at comparable or even better ductility [28]. Further ductilization of alloys can be achieved from improved interfacial cohesion, for example, adding small amounts of boron (typically 0.1 to 0.5 at.%) to polycrystal Ni_3Al substantially improves its ductility [29,59]. This approach is considered to be an efficient and cost-effective way of improving alloy strength without making changes to the bulk composition [28].

In this paper, a BCC high entropy steel with a spinodal-like structure was prepared via magnetron sputtering, and its mechanical properties were evaluated. Iron-enriched regions, which are depleted of chromium, and vice versa, are notable structural features, in addition to boron-enriched grain boundaries. The distribution of iron and chromium follows a characteristic nanoscale-wave pattern, where compositions of Fe and Cr vary by as much as 20 at.%. The combination of high strength and ductility was identified, for which the underlying mechanisms are unlocked.

2. Experimental

The FeMnCoCr-based alloy was prepared by closed field unbalanced magnetron sputtering ion plating (UDP650 magnetron sputtering system, Teer Coatings Ltd, UK). Tool steel of 60 HRC was used as substrates, which were polished to an average roughness of 0.01 μm, degreased, ultrasonically cleaned, and subsequently blown dry in flowing nitrogen gas. A $Fe_{49.5}Mn_{30}Co_{10}Cr_{10}B_{0.5}$ alloy target (China Material Technology Co. Ltd) with a purity of approximately 99.9% and dimensions of 345 mm× 145 mm× 5 mm was used for the deposition. The substrates were stationary during deposition, and the target-to-substrate distance was fixed at 170 mm. The substrate holder was biased with pulsed DC at a frequency of 250 kHz. The vacuum chamber was pumped down to a background pressure of < 400 μPa by controlling the flow rate of Ar (50 sccm, 200 mPa Torr working gas pressure). The DC current applied to the FeMnCoCrB target was fixed at 4.0 A (sputtering power 1.5 kW). Prior to the FeMnCoCrB deposition (–100 V bias, 100 min), plasma ion etching (–450 V bias, 30 min) was conducted to remove the oxide layer and contaminants on the substrate surface. No external heating was used during the deposition.

To ascertain the phase types in the alloy, X-ray diffraction (XRD) was carried out using a Seifert Type ID3003 X-ray diffractometer with Co $K\alpha$ radiation (λ = 0.179 nm), operating at 40 kV and 30 mA. The spectrum was collected in grazing incidence mode ($\alpha = 2°$) to minimize any interference from the substrate.

A nanoindentation system (Fischer-Cripps Laboratories IBIS Nanoindenter, Australia) equipped with a Berkovich indenter was used to measure mechanical properties, viz., hardness (H) and modulus of elasticity (E) in a direction parallel to the thin film growth. Calibration of this instrument was routinely performed with a standard fused quartz specimen (with a reduced elastic modulus of 69 GPa). The test consisted of loading up to 50 mN, and then unloading. The penetration depth corresponded to about 10% of the total film thickness to minimize the effect of the substrates. The hardness and modulus were calculated using the Oliver–Pharr method [30]. The reported mean values and standard deviations are from twenty indentations. To prepare deformed samples for scanning transmission electron microscopy (STEM) analysis, a spherical indenter of 5 μm in radius (Synton-MDP, Switzerland) was used for indentation up to loads of 200 mN and 400 mN.

A focused ion beam (FIB) (Thermo Fisher Scientific Helios Nanolab 600, USA) was used to machine micro-pillars with a diameter of 2 μm and an aspect ratio of 2.5, using currents ranging between 6.5 nA and 93 pA, and final polishing was conducted at 28 pA to achieve the desired surface quality and overall dimensions and mitigate beam-induced dislocations. The micropillar compression tests were conducted inside a scanning electron microscope (SEM) chamber using the Hysitron PI 88 SEM PicoIndenter (Bruker, USA) with a 5 μm diameter flat-tip indenter. The load–displacement curves were corrected for instrument and substrate compliances [31], before being converted into engineering stress–strain curves. Fifteen micro-pillars were tested to ensure the reliability and reproducibility of the results.

To prepare thin sections for transmission electron microscopy (TEM), Transmission Kikuchi Diffraction (TKD), and STEM analysis, cross-sections of alloy thin films before and after loading were lifted out by FIB and milled down to a thickness of ~50 nm. STEM imaging and spectroscopy were performed on a Titan Themis microscope (Thermo Fisher Scientific, USA) operating at 200 kV. Aberration correction of the condenser lenses defines a STEM probe size of < 0.1 nm. Atomic number contrast images were collected using the high-angle annular dark-field (HAADF) detectors. Energy-dispersive X-ray spectroscopy (EDS) mapping was performed at 200 kV. Electron energy loss spectroscopy (EELS) imaging was carried out at 200 kV using a GIF Quantum spectrometer (Gatan, USA). Multivariate statistical analysis was used to highlight the spatial variation of different EELS ionization edges [32]. The TKD data were collected using a Zeiss Merlin field-emission SEM equipped with a Bruker Optimus TKD detector. The data were acquired at 30 kV, and indexation was conducted using the Bruker-ESPIRIT software with pre-defined crystal structure inputs of possible phases at a lateral spatial resolution in the order of 2 nm. Post-processing was undertaken using TSL-OIM (Orientation Image Microscopy) software, which was used for confidence index-based cleaning-up, phase fraction quantification, and to obtain inverse pole figures (IPFs). Atom probe tomography (APT) tips were also prepared using FIB, in which the final stages of sharpening and polishing were conducted at low currents to remove any damaged layers. All measurements were performed in an APT in a CAMECA LEAP 5000 XR in voltage-pulsing mode at a detection rate of 50%, pulse fraction of 15%, pulse repetition rate of 200 kHz, operating at 70 K, and at a pressure below 10^{-8} Pa. The data processing and reconstruction were conducted using commercial APT analysis software package IVAS 3.8.2.
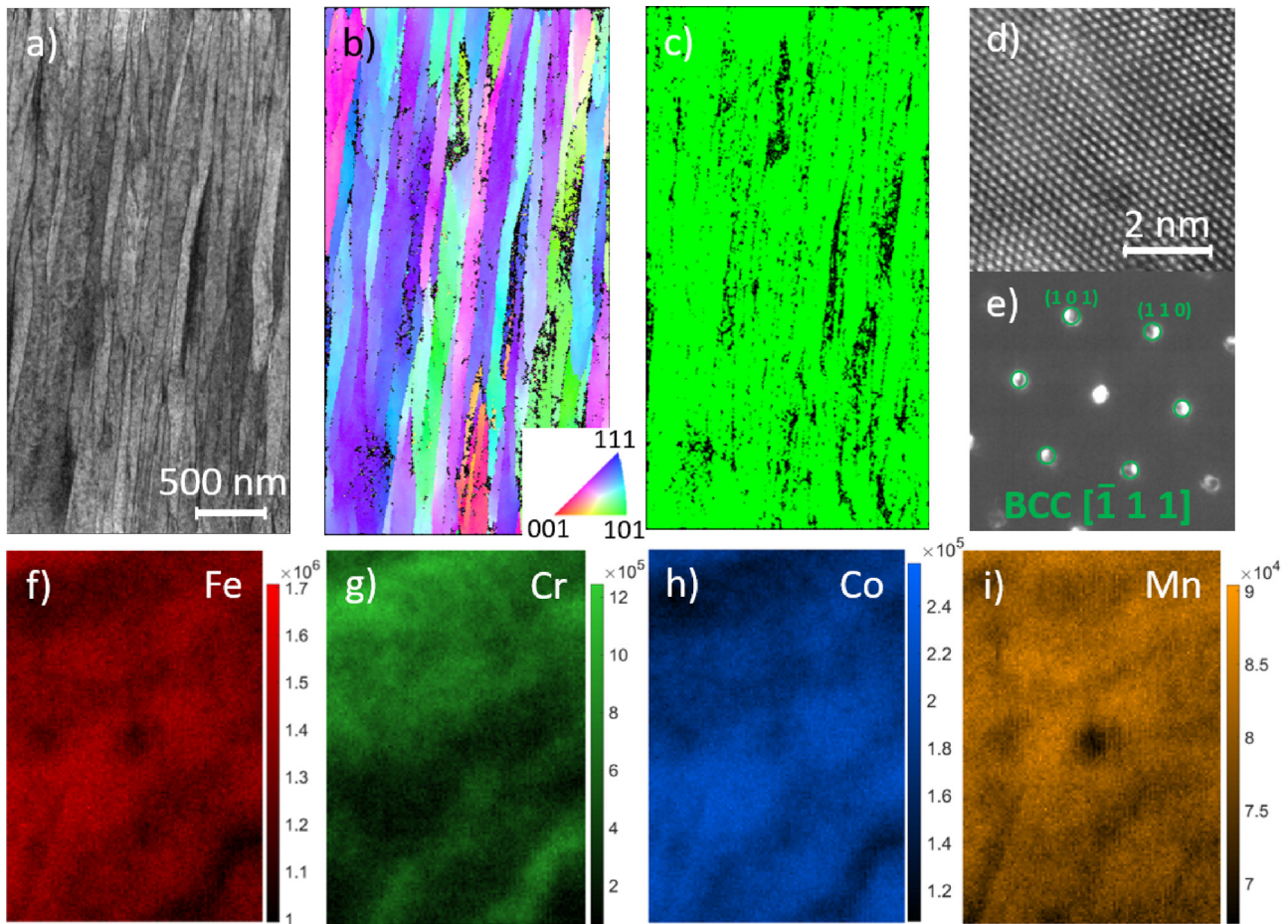
Fig. 1. Microstructural and compositional profiles of the high entropy steel: (a) image quality (IQ) map constructed from Transmission Kikuchi Diffraction (TKD) data, (b) corresponding TKD inverse pole figure (IPF) showing the distinctive columnar structure, (c) corresponding TKD phase map (where green indicates the BCC phase), (d) STEM image showing pristine BCC crystal structure, (e) indexed diffraction pattern, and (f–i) Fe, Cr, Co, and Mn count maps from STEM-EELS spectrum imaging, respectively. STEM-HAADF where EELS spectrum imaging was captured is provided in the supplementary material.

3. Results

The alloy has a columnar structure (Fig. 1(a,b)) with an average grain width of approximately 100 nm, and is free of planar defects (Fig. 1(d)). In addition, the alloy is homogenous and free of porosity or discontinuous regions. The crystal structure was determined to be BCC, as shown by the TKD data ($> 98\%$) (Fig. 1(c)), XRD analysis (Fig. S1 in Supplementary Materials), and indexed selected area diffraction patterns (Fig. 1(e)). The alloy composition measured by APT (Fig. 2(a,b)) in atomic percent was found to be $Fe_{72.40}Co_{13.90}Cr_{10.41}Mn_{2.74}B_{0.34}$, with the remaining balance (< 0.3 at.%) as trace amounts of impurities. This varies greatly from the target composition (viz., $Fe_{49.5}Mn_{30}Co_{10}Cr_{10}B_{0.5}$), likely due to differential atomic mobility and ion bombardment effects typically seen during magnetron sputtering under the influence of bias voltage applied [33]. For example, at a lower biasing voltage of –20 V (c.f. –100 V), the coating composition is much closer to the target composition [34]. APT is particularly important in identifying and measuring the amount of boron (Fig. 3(d,e)), as it is a light element. Large, periodic fluctuations in Fe and Cr content at a wavelength of $\sim$7 nm were observed by EDS (Fig. S2), EELS (Fig. 1(f–i) and Fig. S3), and APT, both in the matrix (Fig. 2(a,b)), and in the GB regions (Fig. 3(b)) with Fe varying between 63.2 at.% and 78.4 at.%, and Cr varying between 1.6 at.% and 22.2 at.%. There is also a minor Co correlation with Fe, and anticorrelation with Cr. The Fe-rich and Cr-rich regions both possess the same crystal structure,

and are coherent, i.e., neither a discrete interface nor a structural discontinuity is apparent between the two regions (Fig. S4(a)). The grain boundary regions are found to be rich in Cr and B, and deficient in Fe (Fig. 3(a–c)). The lattice misfit between the Cr-rich and Fe-rich regions was determined from FFT measurements via correlation of EDS and drift corrected frame integration (DCFI) HR-STEM data (Fig. S4) to be approximately 0.5%, using the standard equation for lattice misfit [35].

Compression of fifteen micropillar specimens (one representative deformed pillar is shown in Fig. 4(b)) produced a yield stress of 2.92 ± 0.36 GPa (measured at a plastic strain offset of 0.2% [11]), and a plastic strain value of $13.7 \pm 1.9\%$ at the ultimate compressive strength (UCS) of 3.37 ± 0.36 GPa. While it is acknowledged that the size effect often exists in small-volume materials, the diameter of the micropillars prepared is much larger than the grain width of the alloy, and thus the dependence of the yield strength on the pillar diameter is considered to be negligible in this work [17,36]. The supplementary material contains a video of micropillar compression testing accompanied by live engineering stress–strain data. Two representative engineering stress–strain curves are shown in Fig. 4(a). Compared to an alloy sputter-deposited using the same target but at a lower bias voltage (viz., –20 V) [34] with very competitive mechanical properties, the yield strength of the new alloy is 0.37 GPa higher, while its plastic strain at the UCS is 11.7% lower. Nanoindentation yielded a hardness of 9.3 ± 0.4 GPa and Young's modulus of 293 ± 12 GPa. The nanoindentation tests
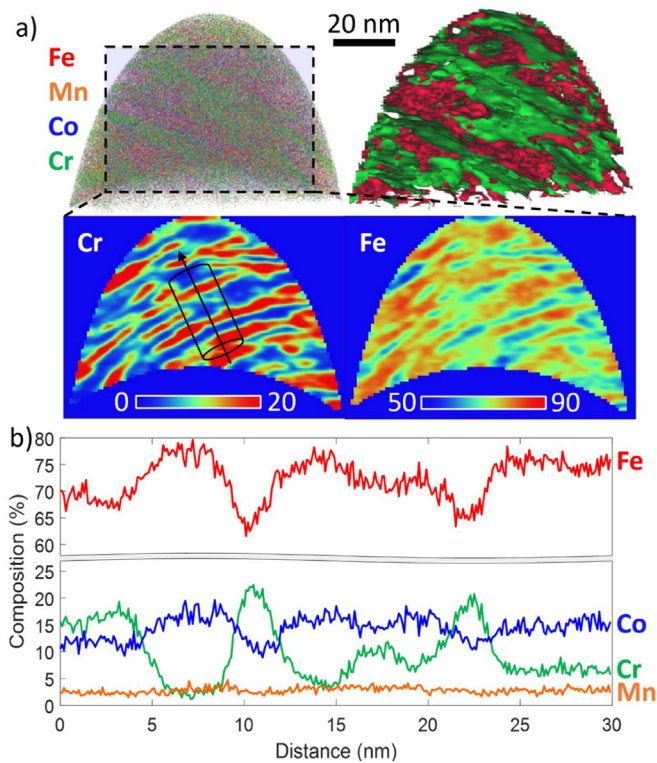
Fig. 2. (a) Atom probe tomography reconstruction showing Fe, Mn, Co, and Cr in the alloy sample, with a 2D compositional map through the dashed cross-section depicting the distribution of Cr and Fe in atomic percent, (b) 1D atomic composition line profile through the region of interest indicated by the cylinder in the 2D compositional profile in (a).

were performed at 50 mN to satisfy the '10% of coating thickness' rule [37], and load–displacement curves are shown in Fig. S5.

After deformation, the alloy maintains its predominantly BCC crystal structure ($>$ 98%) (Fig. 5(c,d)), with neither amorphization [38] nor planar defects observed in STEM imaging (inset Fig. 5(b)). The alloy also exhibits a marked reconfiguration of grain morphology; directly under the indent, regular and more equiaxed grains are present, whereas towards the edges, the columnar grains become narrower (Fig. 5(a,b)). The deformation substructure is shown in Fig. S6. Micropillar compression reveals that under high stress, the material deforms via shear (Fig. 4(b)), and an analysis of the post-mortem structure (Fig. 6(a–d)) demonstrates that this is a highly dislocation-dominated process. In particular, there is a large amount of perfect pure edge dislocations and mixed dislocations that have both edge and screw components in the post-mortem sample within the highly deformed region. Typical examples of dislocations with edge components observed from the [110] zone axis are identified using the methodology outlined in [39], as shown in Fig. 6. Based on the Burgers circuit marked by the white line in Fig. 6(b), the Burgers vector for the perfect pure edge dislocation shown in Fig. 6(a) is $\frac{1}{2}[\bar{1}11]$, and the slip plane is $(\bar{1}1\bar{2})$. Fig. 6(c,d) shows $\frac{1}{2}[1\bar{1}0]$ edge components observed from the [110] zone axis. A dislocation with Burgers vector of [001] appears to have an edge component of $\frac{1}{2}[1\bar{1}0]$ in the HR-STEM image, which is the projection of the [100] onto the (110) plane. Therefore, it can be deduced that the dislocations shown in Fig. 6(c,d) are [100] mixed dislocations with a $\frac{1}{2}[1\bar{1}0]$ edge component and a $\frac{1}{2}[110]$ screw component. Neither deformation twins nor cracks are discernible in these heavily deformed regions, thus asserting good room temperature plasticity in the alloy.

4. Discussion

4.1. Microstructural characteristics

In this study, the observed inverse Fe-Cr compositional fluctuations exist as long-range periodic composition changes in a manner reminiscent of the known spinodal decomposition phenomenon. The maximum concentration of chromium in the present alloy is within the miscibility gap of the Fe-Cr system per the phase diagram shown in [40], i.e., $10 < C_{Cr} < 30$ (at.%), though it should be noted that this diagram does not take the compositions of Co, Mn, and B, into consideration. The inclusion of Cr is known to stabilize the high-density coherent interfaces by tuning the phase separation mode to spinodal decomposition [24]. Solutions undergo spinodal decomposition during temperature changes, i.e., during heating or cooling, and are stable at higher temperatures due to the high entropy of mixing and metastable at lower temperatures [41]. Thus, the spinodal-like nature of the alloy could be due to the use of sputter deposition, as it is a relatively low-temperature technique. The decomposition of FeMnCoCrNi has been studied by Schuh et al. [42], where after annealing, this system separated into Fe + Co, Mn + Ni, and Cr-rich phases. As the present sample has a similar composition, albeit as a non-equiatomic variant with Ni excluded, the inverse relationship between Fe and Cr is expected. Lastly, unlike substitutional alloying, the addition of interstitial elements accelerates the precipitation of the chromium-rich phase (α') [40], and < 2.5 at.% quantities of the interstitial element has been used to induce notable co-enrichment of Fe and Co to grain boundary interfaces [29]. Thus, the inclusion of boron might also contribute to the formation of the spinodal-like structure.

4.2. Strengthening mechanisms

The yield strength of a metallic material is critically related to the mobility of dislocations [43], and thus the fine grain size, interstitial atoms, and grain boundary segregation, all contribute towards the high yield strength of conventional metals. The discontinuity of slip plane and grain orientation from one grain to another makes the motion of dislocations more difficult, and hence, metals with a fine grain size have a higher strength than those with coarse grains [11]. Interstitial atoms increase lattice friction stress via lattice distortion, which restricts dislocation motion [44], and increases yield strength, as demonstrated in the case of soluble boron [45]. Lastly, the grain boundaries were strengthened via boron decoration (Fig. 3(d)). This segregation effect improves the load-bearing capacity of the alloy while reducing the propensity for grain coarsening, which contributes to the enhanced strength of the alloy [28].

The phase separation of Fe and Cr in the present alloy bears resemblance to the formation of Fe-rich α zones, and Cr-rich α' zones in ferritic stainless steels resulting from ferrite decomposition. The presence of α and α' coherent zones inhibits dislocation motion and hardens the steel [25]. This is achieved via the lattice mismatch, which produces a periodic distribution of coherency strain, yielding a corresponding periodic internal stress distribution in the alloy [46]. Such strengthening effects are not limited to ferritic steels, in a study of an $Al_{0.5}Cr_{0.9}FeNi_{2.5}V_{0.2}$ alloy [24], the strengthening contribution from the spinodal structure was calculated to be approximately 1158 MPa [47]. The lattice misfit in the present study of approximately 0.5% (Fig. S4) would contribute significantly to the increase of strength, for example, a lattice misfit of 0.37% in $Fe_{15}Co_{15}Ni_{20}Mn_{20}Cu_{30}$ HEA contributed 375.9 MPa to the alloy strength [35]. While determining individual strengthening contributions for the present alloy is outside of the scope of this paper, it is understood that a significant portion of the present alloy's strength could be attributed to this phenomenon.
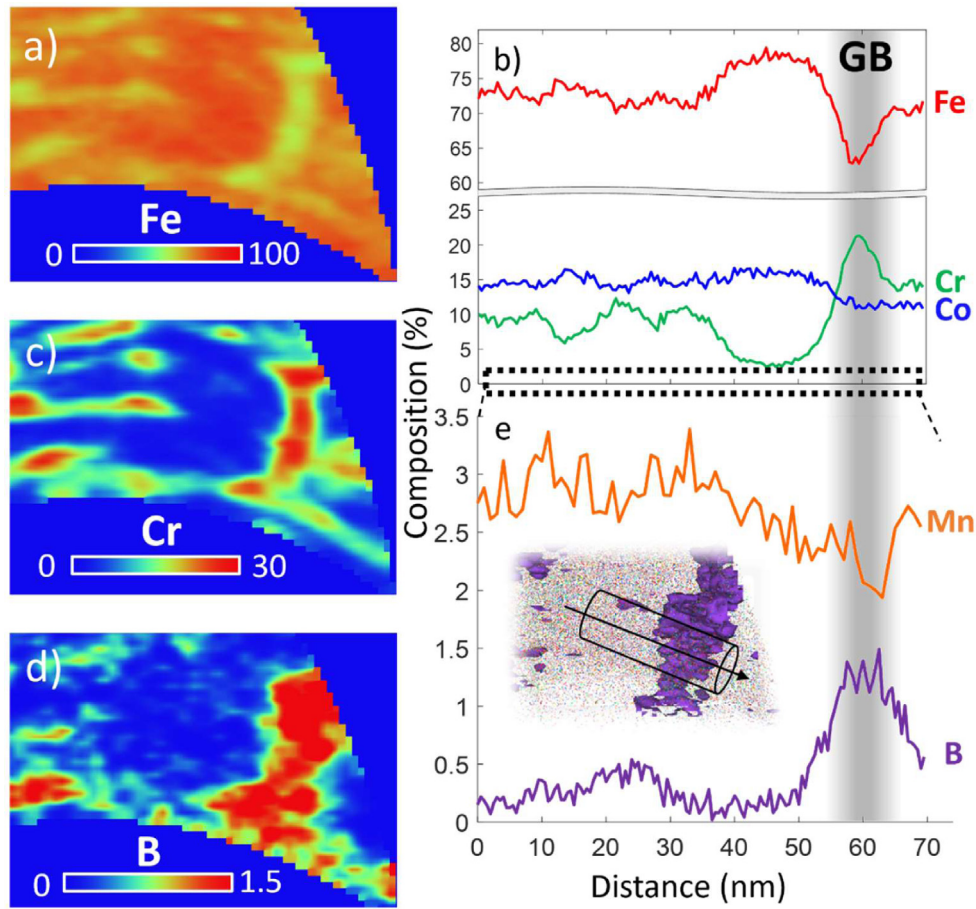
Fig. 3. Atom probe tomography 2D compositional maps through the grain boundary region of (a) Fe, (c) Cr, and (d) B. (b) and (e) provide the 1D compositional profiles of constituent elements, with B iso-concentration surfaces (1.5% threshold) through which the 1D profile is taken shown in (e). The Fe-Cr modulation is also apparent here, with Cr selectively segregating to the GB in tandem with B, with corresponding Fe depletion.
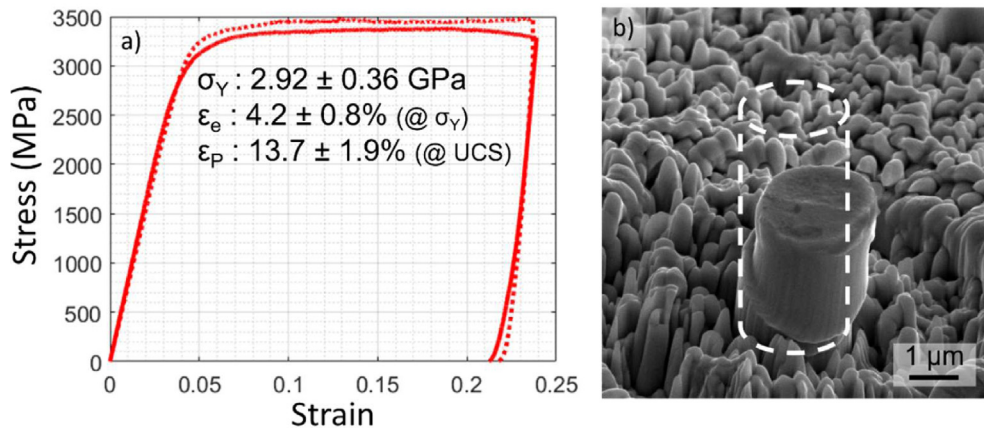

Fig. 4. (a) Two typical engineering stress–strain curves obtained during *in situ* micropillar compression, (b) SEM image of post-mortem micropillar used for subsequent TEM analysis (original dimensions are indicated by the dashed line) showing excellent room temperature plasticity enabled by controlled shear deformation.

4.3. Deformation pathways

The strong-yet-ductile nature of the alloy arises due to the facility of multiple dislocation characters on distinct slip planes and most likely extensive cross-slip. This is evidenced by the relatively high abundance of $\frac{1}{2}[\bar{1}11]$ pure edge dislocations with a slip plane of $(\bar{1}1\bar{2})$, and [100] mixed dislocations with a $\frac{1}{2}[1\bar{1}0]$ edge component and a $\frac{1}{2}[110]$ screw component. In conventional BCC metals, the velocity of pure screw dislocations is orders of magnitude

slower than that of edge dislocations at room temperature, because the glide of screw dislocations needs to overcome a sizable energy barrier [48]. It has been revealed that pure edge dislocations can glide away easily, making them hard to retain and be observed after deformation [49]. Therefore, dislocations are often present in a pure screw orientation as they migrate in conventional BCC metals. However, we observed the presence of multiplanar, multi-character dislocation slip, including abundant edge and mixed dislocations in the experimental alloy. This observation agrees with
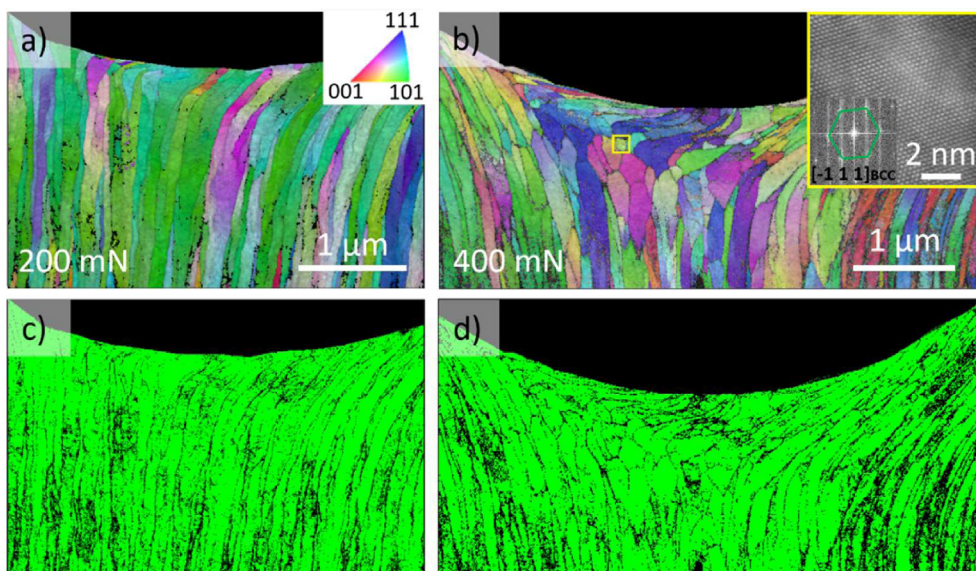
Fig. 5. Post-mortem analysis of the indentation deformation in the alloy sample: (a) IPF of sample deformed at a maximum load of 200 mN, and (b) 400 mN, with corresponding phase maps (c) and (d), where BCC structure is indicated by green. BCC structure is shown in the STEM image in the inset in (b), obtained in the vicinity marked by the yellow rectangle.
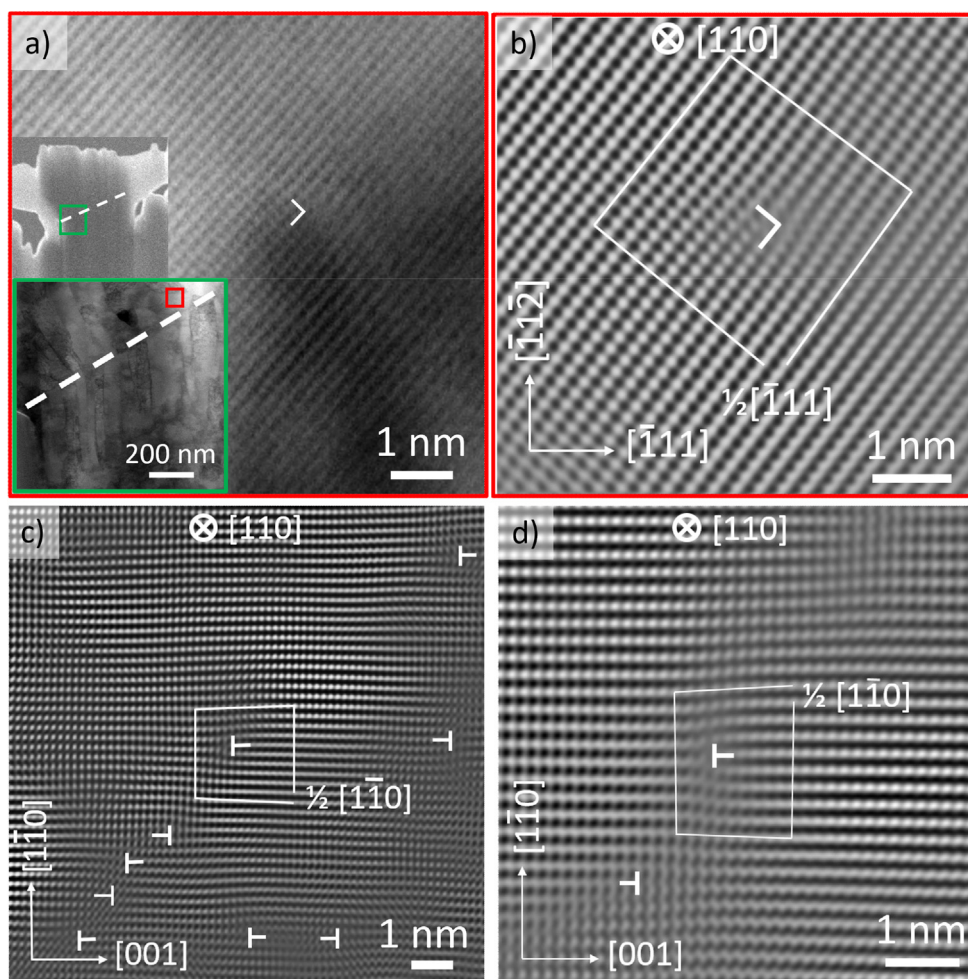
Fig. 6. Dislocation analysis in the shear region of the post-mortem pillar sample showing dislocations with edge components along the [110] zone axis: (a) STEM image along the [110] zone axis showing the presence of $\frac{1}{2}[\bar{1}11]$ pure edge dislocation, with the region of interest used for TEM analysis marked by the red square in the inset, (b) corresponding FFT filtered image showing the unclosed Burgers circuit, and (c) and (d) STEM images presenting $\frac{1}{2}[1\bar{1}0]$ edge component from [100] dislocations observed nearby.

the deformation in the BCC HEA MoNbTi, which is also accommodated by multiple dislocation pathways and activation of multiple slip planes [10]. The distinctive dislocation activities in BCC HEAs could be attributed to the diminished distinctions in the mobility or slip resistance between edge dislocations and screw dislocations on various slip planes [[10,50]], presumably rooted in their atomic-scale chemical fluctuations. As one of the most important deformation modes in metallic materials, dislocation activities are frequently found to cause shear localization and contribute to poor ductility [51,52]. In contrast, relatively uniform plasticity may be obtained if the dislocation activities can be stimulated on multiple slip systems [51,52]. Therefore, the formation and operation of multiple dislocations pathways enable excellent plastic deformability and damage tolerance of the current BCC HEA.

It is also anticipated that cross-slip is an active mechanism in this alloy, given that fluctuations in composition in CCAs were found to promote cross-slip [21,53,54]. It was reported that the inhomogeneous element distribution facilitates dislocation cross-slip in the CrFeCoNiPd HEA, by elevating the intensity of lattice friction, resulting in stronger resistance to dislocation motion [21]. Because dislocations on the primary slip plane experienced high resistance to their motion, many dislocations in the pile-up are expected to cross-slip. Therefore, dislocation cross-slips would be observed due to fluctuations in composition [21]. In Fe-Cr BCC alloys, cross slip prevents local stress concentrations, as frequently observed in ductile alloy specimens [55]. Frequent cross-slip and ensuing dislocation interactions promote strain hardening, which is considered to be a reliable source of enhanced tensile ductility and toughness. The occurrence of dislocation pile-up, cross-slips, and multiple shearing events is considered to be a dynamic process that produced simultaneous sources of hardening and softening, leading to the relatively flat stress–strain curve observed during plastic deformation (see supplementary video). However, it is worth noting that cross-slips are difficult to identify in nanostructured metals.

Another important factor to take into account is the coherency of Fe- and Cr-rich regions. When spinodal decomposition results in coherent regions between opposing phases, the strength and hardness can be enhanced without sacrificing much ductility [24]. The coherency can ensure that dislocations can pass the coherent interface regions upon reaching higher stress levels to avoid local stress concentrations, meaning that elastic strain accumulation resulting from dislocation shear is effectively regulated, and crack initiation is prevented [24]. Meanwhile, the sample undergoes several shear events in tandem with the dislocation-dominated behavior, effectively circumventing catastrophic failure modes. This may explain why the hardening effect is not particularly significant during plastic deformation, resulting in a UCS of 3.37 ± 0.36 GPa. While this is comparable to many high-entropy alloys with excellent strain-hardening capabilities [56–58], the yield strength of the present alloy is superior (2.92 ± 0.36 GPa, c.f. approx. 1– 2 GPa).

5. Conclusion

Nanoscale compositional fluctuations were exploited in conjunction with interstitial element additions and grain boundary segregation to create a strong and yet ductile BCC structured high entropy steel. An inverse relationship exists in spatial distribution between Fe and Cr contents, with the composition of each element fluctuating by up to 20%. The yield strength was determined using *in-situ* micropillar compression tests to be 2.92 ± 0.36 GPa, with a plasticity value of $13.7 \pm 1.9\%$ obtained at the ultimate compressive strength. Multiple slip systems were found to be active, evidenced by a high abundance of $\frac{1}{2}[\bar{1}11]$ pure edge dislocations with a slip plane of $(\bar{1}1\bar{2})$ co-operating with $[100]$ mixed dislocations with a $\frac{1}{2}[1\bar{1}0]$ edge component and a $\frac{1}{2}[110]$ screw compo-

nent. Meanwhile, multiple shear events occurred steadily. The results shed light on the extent of compositional/structural control that can be exploited to achieve strength–ductility unity in BCC-based high entropy steel.

Supplementary materials

Supplementary material associated with this article can be found, in the online version, at doi:10.1016/j.jmst.2021.10.019.

References

[1] D. Raabe, C.C. Tasan, H. Springer, M. Bausch, Steel Res. Int. 86 (2015) 1127–1138.
[2] J.W. Yeh, Ann. Chim. Sci. Mater. 31 (2006) 633–648.
[3] J.W. Yeh, S.K. Chen, S.J. Lin, J.Y. Gan, T.S. Chin, T.T. Shun, C.H. Tsau, S.Y. Chang, Adv. Eng. Mater. 6 (2004) 299–303.
[4] B. Gludovatz, A. Hohenwarter, D. Catoor, E.H. Chang, E.P. George, R.O. Ritchie, Science 345 (2014) 1153–1158.
[5] B. Cantor, Entropy 16 (2014) 4749–4768.
[6] D.B. Miracle, O.N. Senkov, Acta Mater. 122 (2017) 448–511.
[7] Z. Li, K.G. Pradeep, Y. Deng, D. Raabe, C.C. Tasan, Nature 534 (2016) 227–230.
[8] X. An, Science 373 (2021) 857–858.
[9] J. Cairney, Science 370 (2020) 37–38.
[10] F. Wang, G.H. Balbus, S. Xu, Y. Su, J. Shin, P.F. Rottmann, K.E. Knipling, J.C. Stinville, L.H. Mills, O.N. Senkov, I.J. Beyerlein, T.M. Pollock, D.S. Gianola, Science 370 (2020) 95–101.
[11] W. Callister, D. Rethwisch, Materials Science and Engineering an Introduction, 9th ed., Wiley, New Jersey, 2014.
[12] S.S. Sohn, A. Kwiatkowski da Silva, Y. Ikeda, F. Körmann, W. Lu, W.S. Choi, B. Gault, D. Ponge, J. Neugebauer, D. Raabe, Adv. Mater. 31 (2019) 1807142.
[13] B. Gludovatz, A. Hohenwarter, K.V.S. Thurston, H. Bei, Z. Wu, E.P. George, R.O. Ritchie, Nat. Commun. 7 (2016) 1–8 10602.
[14] G. Laplanche, A. Kostka, C. Reinhart, J. Hunfeld, G. Eggeler, E.P. George, Acta Mater. 128 (2017) 292–303.
[15] J. Miao, C.E. Slone, T.M. Smith, C. Niu, H. Bei, M. Ghazisaeidi, G.M. Pharr, M.J. Mills, Acta Mater. 132 (2017) 35–48.
[16] S.J. Tsianikas, Y. Chen, Z. Xie, J. Mater. Sci. Technol. 39 (2020) 7–13.
[17] Y.J. Chen, X.H. An, Z.F. Zhou, P. Munroe, S. Zhang, X.Z. Liao, Z.H. Xie, Sci. China Mater. 64 (2021) 209–222.
[18] Y.J. Chen, Z.F. Zhou, P. Munroe, Z.H. Xie, Appl. Phys. Lett. 113 (2018) 081905.
[19] R. Zhang, S. Zhao, J. Ding, Y. Chong, T. Jia, C. Ophus, M. Asta, R.O. Ritchie, A.M. Minor, Nature 581 (2020) 283–287.
[20] B. Cantor, I.T.H. Chang, P. Knight, A.J.B. Vincent, Mater. Sci. Eng. A 375–377 (2004) 213–218.

[21] Q.Q. Ding, Y. Zhang, X. Chen, X.Q. Fu, D.K. Chen, S.J. Chen, L. Gu, F. Wei, H.B. Bei, Y.F. Gao, M.R. Wen, J.X. Li, Z. Zhang, T. Zhu, R.O. Ritchie, Q. Yu, Nature 574 (2019) 223–227.
[22] J.W. Cahn, Acta Metall. 9 (1961) 795–801.
[23] J.W. Gibbs, Collected Works, Yale University Press, New Haven, CT, 1948.
[24] Y.J. Liang, L.J. Wang, Y.R. Wen, B.Y. Cheng, Q.L. Wu, T.Q. Cao, Q. Xiao, Y.F. Xue, G. Sha, Y.D. Wang, Y. Ren, X.Y. Li, L. Wang, F.C. Wang, H.N. Cai, Nat. Commun. 9 (2018) 4063.
[25] M.B. Cortie, H. Pollak, Mater. Sci. Eng. A 199 (1995) 153–163.
[26] L.L. Li, Z.M. Li, A. Kwiatkowski da Silva, Z.R. Peng, H. Zhao, B. Gault, D. Raabe, Acta Mater. 178 (2019) 1–9.
[27] D. Raabe, M. Herbig, S. Sandlöbes, Y. Li, D. Tytko, M. Kuzmina, D. Ponge, P.P. Choi, Curr. Opin. Solid State Mater. Sci. 18 (2014) 253–261.
[28] J.B. Seol, J.W. Bae, Z. Li, J.Chan Han, J.G. Kim, D. Raabe, H.S. Kim, Acta Mater. 151 (2018) 366–376.
[29] T. Yang, Y.L. Zhao, W.P. Li, C.Y. Yu, J.H. Luan, D.Y. Lin, L. Fan, Z.B. Jiao, W.H. Liu, X.J. Liu, J.J. Kai, J.C. Huang, Science 369 (2020) 427.
[30] W.C. Oliver, G.M. Pharr, J. Mater. Res. 7 (2011) 1564–1583.
[31] H. Zhang, B.E. Schuster, Q. Wei, K.T. Ramesh, Scr. Mater. 54 (2006) 181–186.
[32] S.Y. Zhang, C. Scheu, Microscopy 67 (2017) 1–9.
[33] F.Y. Cao, P. Munroe, Z.F. Zhou, Z.H. Xie, Thin Solid Films 639 (2017) 137–144.
[34] S. Tsianikas, Y. Chen, J. Jeong, S. Zhang, Z. Xie, Nanoscale 13 (2021) 3602–3612.
[35] Z.Y. Rao, B. Dutta, F. Körmann, W.J. Lu, X.Y. Zhou, C. Liu, A.K. da Silva, U. Wiedwald, M. Spasova, M. Farle, D. Ponge, B. Gault, J. Neugebauer, D. Raabe, Z. Li, Adv. Funct. Mater. 31 (2021) 2007668.
[36] Y.J. Chen, X.H. An, X.Z. Liao, Appl. Phys. Rev. 4 (3) (2017) 031104.
[37] A.C. Fischer-Cripps, Nanoindentation, Springer, New York, 2013.
[38] H. Wang, D. Chen, X.H. An, Y. Zhang, S.J. Sun, Y.Z. Tian, Z.F. Zhang, A.G. Wang, J.Q. Liu, M. Song, S.P. Ringer, T. Zhu, X.Z. Liao, Sci. Adv. 7 (14) (2021), doi:10.1126/sciadv.abe3105.
[39] G.M. Cheng, W.Z. Xu, W.W. Jian, H. Yuan, M.H. Tsai, Y.T. Zhu, Y.F. Zhang, P.C. Millett, J. Mater. Res. 28 (2013) 1820–1826.
[40] J.K. Sahu, U. Krupp, R.N. Ghosh, H.J. Christ, Mater. Sci. Eng. A 508 (2009) 1–14.
[41] A. Kwiatkowski da Silva, D. Ponge, Z. Peng, G. Inden, Y. Lu, A. Breen, B. Gault, D. Raabe, Nat. Commun. 9 (2018) 1137.
[42] B. Schuh, F. Mendez-Martin, B. Völker, E.P. George, H. Clemens, R. Pippan, A. Hohenwarter, Acta Mater. 96 (2015) 258–268.
[43] K. Lu, Nat. Rev. Mater. 1 (2016) 16019.
[44] Z.M. Li, C.C. Tasan, H. Springer, B. Gault, D. Raabe, Sci. Rep. 7 (2017) 40704.
[45] J.B. Seol, J.W. Bae, J.G. Kim, H. Sung, Z. Li, H.H. Lee, S.H. Shim, J.H. Jang, W.S. Ko, S.I. Hong, H.S. Kim, Acta Mater. 194 (2020) 366–377.
[46] A. Takahashi, T. Suzuki, A. Nomoto, T. Kumagai, Acta Mater. 146 (2018) 160–170.
[47] A.J. Ardell, Metall. Trans. A 16 (1985) 2131–2165.
[48] J. Chaussidon, M. Fivel, D. Rodney, Acta Mater. 54 (2006) 3407–3416.
[49] G. Monnet, D. Terentyev, Acta Mater. 57 (2009) 1416–1426.
[50] B. Chen, S. Li, H. Zong, X. Ding, J. Sun, E. Ma, Proc. Natl. Acad. Sci. U. S. A. 117 (2020) 16199–16206.
[51] G. Cao, J.W. Wang, K. Du, X.L. Wang, J.X. Li, Z. Zhang, S.X. Mao, Adv. Funct. Mater. 28 (2018) 1805258.
[52] J.W. Wang, F. Sansoz, J.Y. Huang, Y. Liu, S.H. Sun, Z. Zhang, S.X. Mao, Nat. Commun. 4 (2013) 1742.
[53] Q.Q. Ding, Y. Zhang, X. Chen, X.Q. Fu, D.K. Chen, S.J. Chen, L. Gu, F. Wei, H.B. Bei, Y.F. Gao, M.R. Wen, J.X. Li, Z. Zhang, T. Zhu, R.O. Ritchie, Q. Yu, Nature 574 (2019) 223–227.
[54] Z. Lei, X. Liu, Y. Wu, H. Wang, S. Jiang, S. Wang, X. Hui, Y. Wu, B. Gault, P. Kontis, D. Raabe, L. Gu, Q. Zhang, H. Chen, H. Wang, J. Liu, K. An, Q. Zeng, T.G. Nieh, Z. Lu, Nature 563 (2018) 546–550.
[55] G. Mima, M. Yamaguchi, J. Jpn. Inst. Met. Mater. 29 (1965) 1182–1189.
[56] Y. Dong, Y.P. Lu, J.R. Kong, J.J. Zhang, T.J. Li, J. Alloy. Compd. 573 (2013) 96–101.
[57] Y. Dong, K.Y. Zhou, Y.P. Lu, X.X. Gao, T.M. Wang, T.J. Li, Mater. Des. 57 (2014) 67–72.
[58] S. Wu, D. Qiao, H. Zhao, J. Wang, Y. Lu, J. Alloy. Compd. 889 (2022) 161800.
[59] K. Aoki, Ductilization of L1$_2$ Intermetallic Compound Ni$_3$Al by Microalloying with Boron, Materials Transactions, JIM 31 (6) (1993) 443–448.

Chapter 6

Adaptive attenuation of hierarchical composition fluctuations extends the plasticity of a high entropy steel

Statement of Authorship

Title of Paper	Deformation-Induced Attenuation of Hierarchical Compositional Fluctuations Mediates Plasticity in a High Entropy Steel
Publication Status	☐ Published ☐ Accepted for Publication ☐ Submitted for Publication ☑ Unpublished and Unsubmitted work written in manuscript style
Publication Details	S. J. Tsianikas, Y. Chen, A. Slattery, J. Peters, Z. Xie (2022). "Deformation-Induced Attenuation of Hierarchical Compositional Fluctuations Mediates Plasticity in a High Entropy Steel".

Principal Author

Name of Principal Author (Candidate)	Simon Tsianikas		
Contribution to the Paper	Acquiring Data, Knowledge, Analysis, Drafting		
Overall percentage (%)	70%		
Certification:	This paper reports on original research I conducted during the period of my Higher Degree by Research candidature and is not subject to any obligations or contractual agreements with a third party that would constrain its inclusion in this thesis. I am the primary author of this paper.		
Signature		Date	24/02/2022

Co-Author Contributions

By signing the Statement of Authorship, each author certifies that:

    i.   the candidate's stated contribution to the publication is accurate (as detailed above);

    ii.   permission is granted for the candidate in include the publication in the thesis; and

    iii.   the sum of all co-author contributions is equal to 100% less the candidate's stated contribution.

Name of Co-Author	Yujie Chen
Contribution to the Paper	Knowledge, Analysis, Drafting
Signature	Date 24/02/2022

Name of Co-Author	Jonathan Peters
Contribution to the Paper	Knowledge, Analysis
Signature	Date 24/02/2022

Name of Co-Author	Ashley Slattery
Contribution to the Paper	Acquiring Data, Knowledge
Signature	Date 18/2/2022

Name of Co-Author	Zonghan Xie
Contribution to the Paper	Conception, Knowledge, Analysis, Drafting
Signature	Date 18/2/2022

Adaptive attenuation of hierarchical composition fluctuations augments the plastic strain of a high entropy steel

Simon Tsianikas[1], Yujie Chen[1], Ashley Slattery[2], Jonathan Peters[3], and Zonghan Xie[1]

[1] School of Mechanical Engineering, The University of Adelaide, Adelaide, SA, 5005, Australia

[2] Adelaide Microscopy, The University of Adelaide, Adelaide, SA, 5005, Australia

[3] School of Physics, Trinity College Dublin, Dublin, Ireland

Abstract

A body-centred cubic (BCC) high entropy steel with a spinodal-like nanopattern and atomic-scale local chemical fluctuations exhibits controlled attenuation of its chemical complexity with deformation. Changes in the chemical composition of the spinodal structure measured using energy dispersive X-ray spectroscopy reveal that the average composition peak-to-peak amplitude decreases by 67% from 4.9 at.% to 1.6 at.% with increasing strain. On the other hand, the short-range chemical fluctuations, assessed with atomic strain mapping, displays a 48% decrease in the average strain peak-to-peak amplitude from 3.03 at.% to 1.59 at.% under mechanical loading. The reduction in local strain brought about by increased chemical homogeneity at both levels enables more uniform, steady deformation leading to extended ductility (13.7 $\pm$ 1.9%), all the while maintaining ultrahigh strength (2.92 $\pm$ 0.36 GPa, placing it among the highest values reported). The interactions between dislocations and concentration waves are identified and found to be responsible for this compelling effect on the newly created steel.

Introduction

In addition to the enhanced solid solution strengthening effect [1] commonly seen in compositionally complex alloys (CCAs), including high-entropy steel (HES) [2], short-

range chemical fluctuations (typically in the range of 1 to 3 nm) arising due to chemical pair correlations, so-called 'short range ordering' (SRO) or 'local chemical ordering' (LCO), has entered the spotlight in recent times. Multiple factors, such as the bonding strength, and electronic and magnetic interactions, can serve as the driving force for SRO [3]. Typical examples include replacing Mn with Pd in the Cantor alloy to increase the difference in atomic size and electronegativity [4], and doping of oxygen in TiZrHfNb HEA to form numerous nanoscale SRO complexes with Ti and Zr by taking advantage of oxygen's chemical affinity [5]. The extent of SRO can also be tweaked through thermal treatments, demonstrated via atomic strain mapping results of water-quenched, aged and slow furnace cooled CrCoNi [6].

The effect that SRO has on the mechanical properties of CCAs is well documented. The rugged chemical environment induces stick-slip dislocation forward glide, meaning that dislocations must undergo nanoscale segment detrapping (NSD) when traversing local chemical heterogeneities [7]. The increased energy cost associated with NSD results in an elevated resistance to dislocation motion [8]. Further, chemical inhomogeneities are able to facilitate the distribution of dislocation activities over multiple lattice planes [9]. Another implication of SRO specifically applies to BCC metals; whereas screw dislocation motion is ordinarily orders of magnitude slower than edge dislocation glide, both gain similar mobility in BCC CCAs due to the SRO impacting the dislocation core configuration and dislocation mobility [8, 10, 11]. Consequently, multicharacter, multiplanar slips have been observed in BCC CCAs [12], including HES [13], where edge and mixed dislocations are identified through post-mortem examination, revealing their substantial contribution towards additional strength and plasticity via strain hardening [14].

On the other hand, 'spinodal decomposition' [15] has been used to describe increased *nanoscale* chemical complexity manifested by medium- or long-range composition fluctuations in materials, prior to the emergence of two or more distinct phases. This process is also known to help enhance the mechanical properties of metals by creating extensive dislocation roadblocks leading to strengthening from frequent jamming of dislocations, while promoting cross-slip routes that enhance ductility [16]. Meanwhile, innate structural coherency alleviates elastic strain accumulation and hence helps prevent crack initiation to retain decent ductility and work-hardening capacity in these alloys [17].

While the benefits to the mechanical properties of compositional fluctuations due to SRO and spinodal structuring are well established, less reported are observations of the effect that deformation has on these chemical heterogeneities and its impact on the plastic strain of CCAs. Moreover, the integration these two powerful features in a BCC metal for enhanced strength-ductility synergy has not been reported so far. Here, we report the unique observation of nanoscale SRO in a BCC HES in-tandem with larger-scale spinodal-like fluctuations in its Fe and Cr concentrations. The dynamic attenuation of compositional fluctuations under mechanical loading, over multiple length scales, and its impact upon the alloy strength and plasticity, is discussed in detail.

Experimental

The FeMnCoCr-based alloy was prepared as a thin film following a process described elsewhere [13]. A Helios Nanolab 600 focused ion beam (FIB) (Thermo Fisher Scientific, USA) was used to fashion micro-pillars with a diameter of 2 µm and an aspect ratio of 2.5, using currents ranging from 6.5 nA to 93 pA, and final polishing was conducted at 28 pA to achieve the desired surface quality and overall dimensions, and mitigate beam-induced dislocations. The micropillar compression tests were carried out inside a scanning electron microscope (SEM) chamber using the Hysitron PI 88 SEM PicoIndenter (Bruker, USA) with a 5 µm diameter flat-tip indenter. The load-displacement curves were corrected for instrument and substrate compliances [18], before being converted into engineering stress–strain curves. Ten micro-pillars were tested to ensure the reliability and reproducibility of the results.

To prepare samples for scanning transmission electron microscopy (STEM) analysis, the cross-sections of the alloy thin films before and after deformation were lifted out by FIB and milled down to a thickness of ~50 nm for electron transparency. STEM imaging was performed on a Titan Themis microscope (Thermo Fisher Scientific, USA) operating at 200 kV. Aberration correction of the condenser lenses defines a STEM probe size of < 0.1 nm. Atomic number contrast images were collected using the high angle annular dark field (HAADF) detectors. Energy dispersive X-ray spectroscopy (EDS) mapping was executed at 200 kV. Data averaging was accomplished by applying an average prefilter of five pixels, drawing a profile with a width of twenty pixels, and then exporting the extracted profile.

Atomic strain mapping was conducted using drift corrected frame integration (DCFI) high resolution (HR)-STEM images and the Strain++ software developed by Dr J. Peters [19], an open-source program using the geometric phase analysis (GPA) algorithm [20]. To remove imaging distortions, images were formed from multi-frame averages after non-rigid registration using SmartAlign [21]. Each image consists of 30 frames with dimensions of 1024 x 1024 pixels and a dwell time of 0.5 µs.

Results

Mechanical Property	Value
σ_Y	2.92 ± 0.36 GPa
σ_{UTS}	3.37 ± 0.36 GPa
$\varepsilon_{e\ @\ UTS}$	4.20 ± 0.78 %
$\varepsilon_{P\ @\ UTS}$	13.7 ± 1.9 %
H	9.29 ± 0.38 GPa
E	293 ± 12 GPa

Table 1: Summary of Mechanical Properties of the high entropy steel prepared in this work.
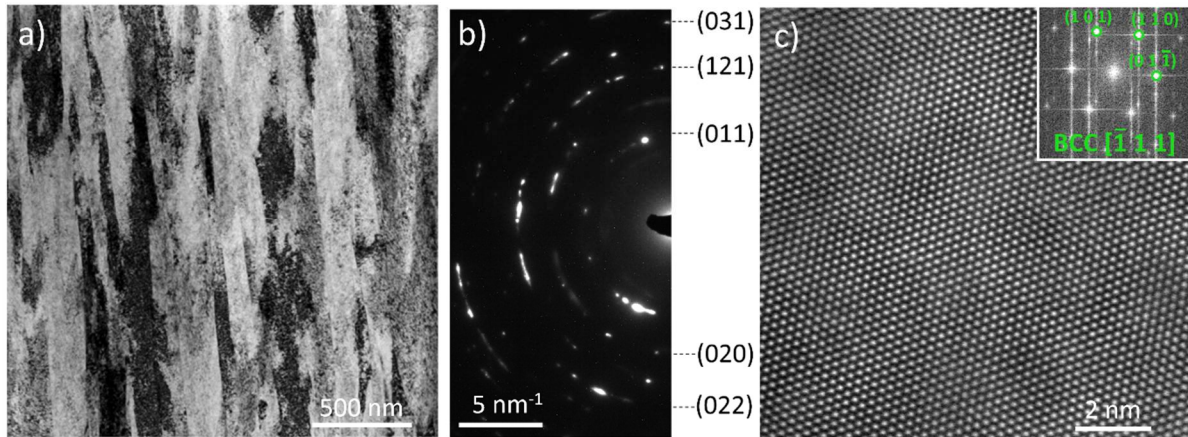
Figure 1: (a) High-Angle Annular Dark-Field Transmission Electron Microscope image of the vertically aligned nanocolumnar structure, (b) selected area electron diffraction pattern of polycrystalline region solely indexed to body-centred cubic (BCC) structure, and (c) DCFI HR-STEM image of BCC crystal structure imaged along the $[\bar{1}\ 1\ 1]$ zone axis.
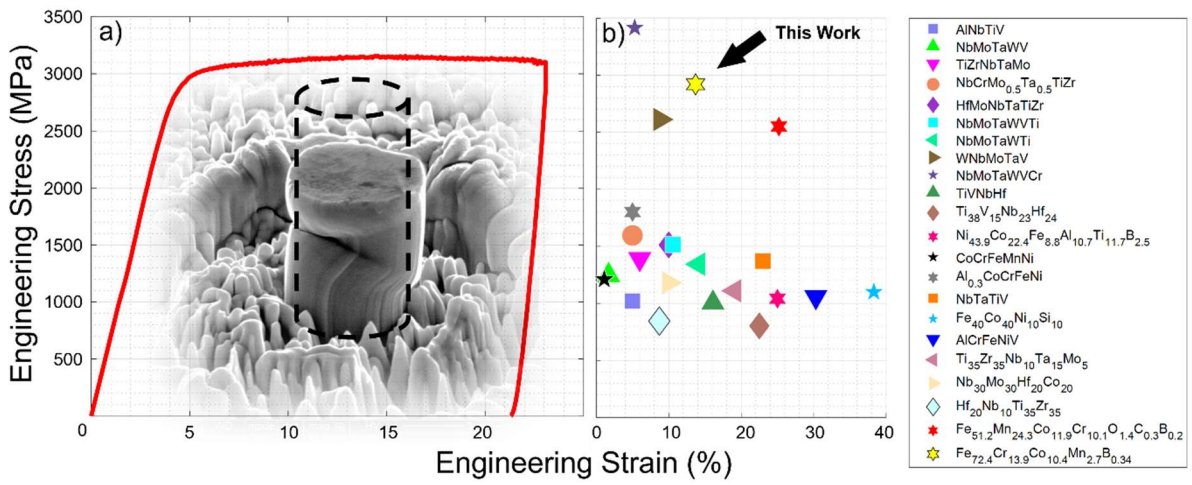
Figure 2: (a) Representative engineering stress – engineering strain curve and post-mortem pillar. The shape of the original pillar (dashed profile) is superimposed over the compressed one for comparison purpose; (b) yield strength and plastic strain at failure obtained for a range of high-strength HEAs at room temperature. Data references are available in the supplementary material.
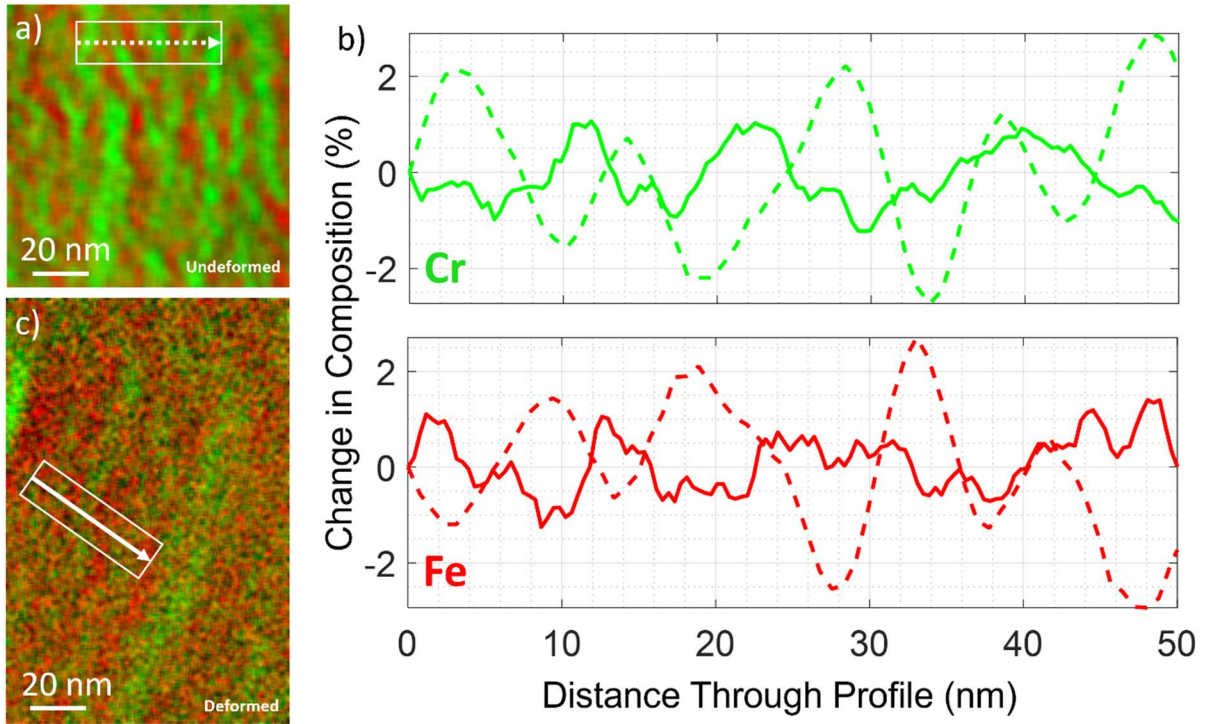
Figure 3: EDS spectra of (a) as-deposited sample and (c) deformed sample, with (b) corresponding 2D compositional profiles of Fe and Cr for regions indicated in (a) (dashed) and (c) (solid line).
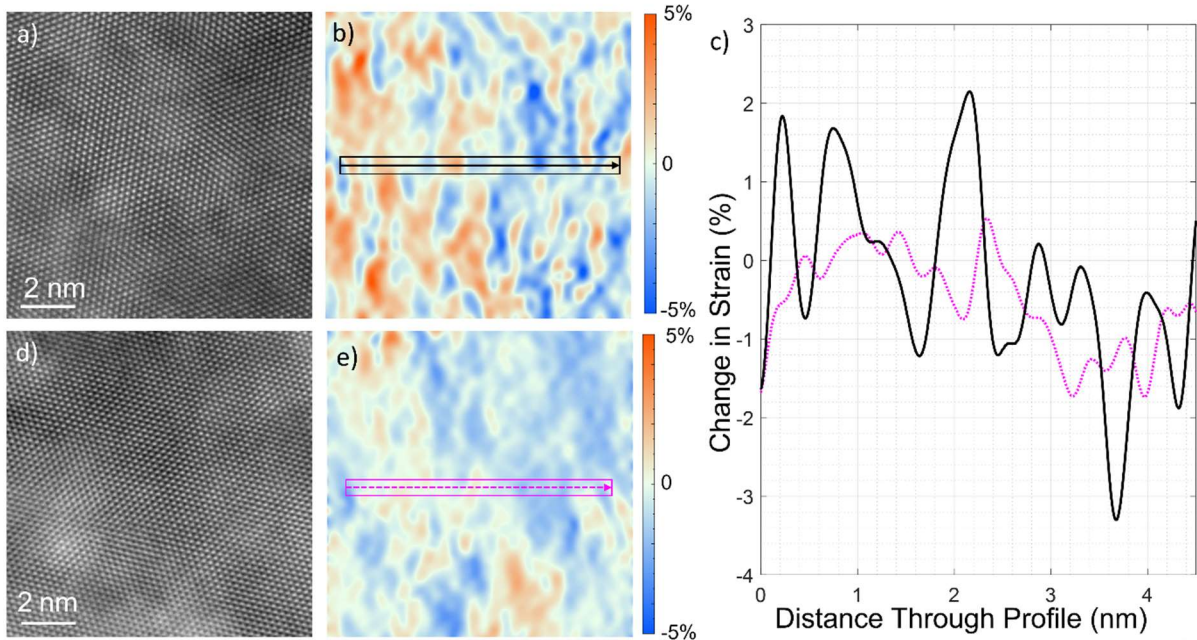
Figure 4: Strain mapping analysis; (a) DCFI HR-STEM image of as-deposited sample, (b) corresponding ε_{xx} strain map, (d) DCFI HR-STEM image of deformed sample, (e) corresponding ε_{xx} strain map, (c) corresponding 2D strain profile for the boxed regions indicated in (b) and (e).
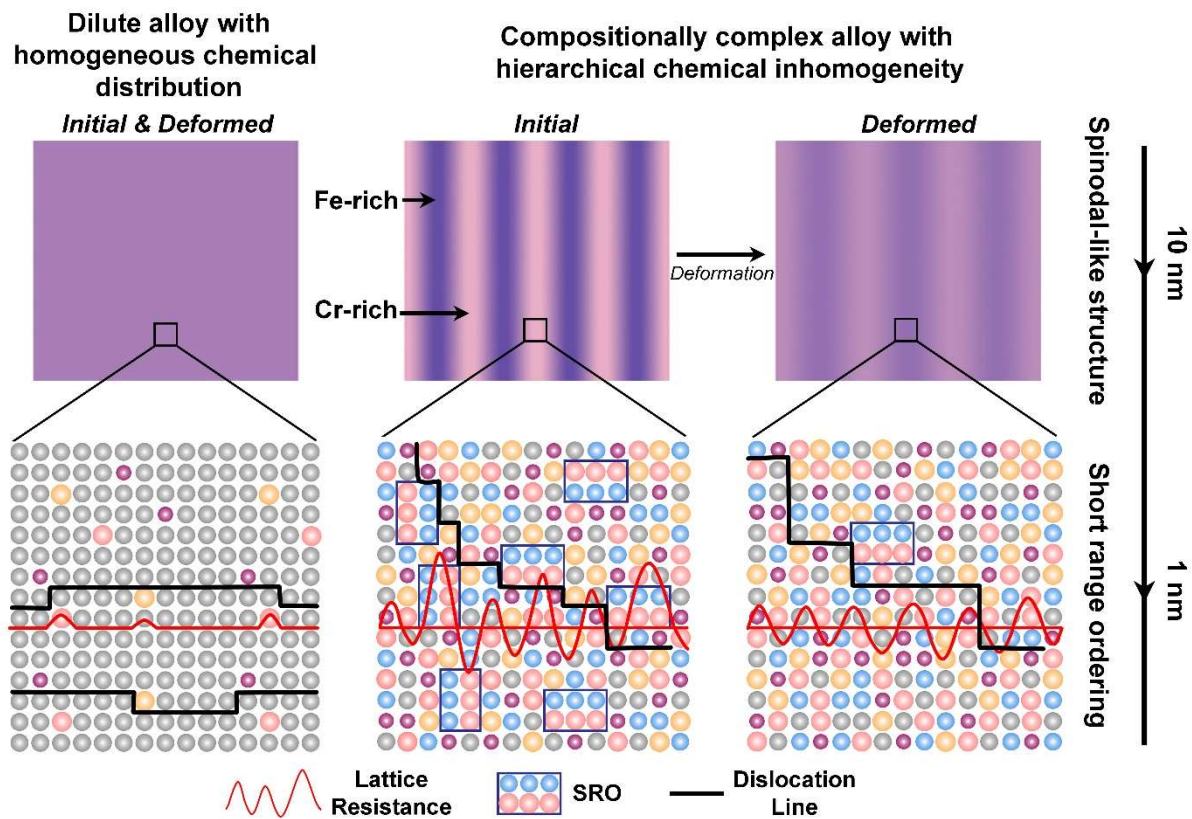
Figure 5: Conceptual infographic showing the difference in chemical heterogeneity between a conventional alloy and a compositionally complex alloy, and the effect that deformation has on the hierarchical chemical inhomogeneity of the latter.

A typical cross-sectional microstructure of the as-deposited $Fe_{72.4}Co_{13.9}Cr_{10.4}Mn_{2.7}B_{0.34}$ alloy is presented in Figure 1(a), showing a columnar nanograined structure with a grain width of ~100 nm. The as-deposited sample comprises single BCC phase, as evidenced by the selected area electron diffraction pattern (Figure 1(b)) and the high-resolution HAADF-STEM image (Figure 1(c)). The alloy sample is free from pre-existing planar defects (Figure 1(c)). The mechanical properties of the $Fe_{72.4}Co_{13.9}Cr_{10.4}Mn_{2.7}B_{0.34}$ alloy are provided in Table 1 [13], and one representative engineering stress-strain curve along with an image of a compressed micropillar is shown in Figure 2(a). The alloy has a high strength (2.92 ± 0.36 GPa), and reasonable plasticity ($13.7 \pm 1.9\%$), as evidenced by the extended engineering stress-strain curve under mechanical loading, and is among the highest values reported (Figure 2(b)). Further microstructural and mechanical characterisation details are available elsewhere [13].

EDS analysis was performed to examine the distribution of the chemical compositions in the pristine and deformed states of the CCA sample. As shown in Figure 3(a), the distribution of Fe and Cr in the pristine sample exhibits a characteristic spinodal-like pattern at the nanometre scale, where compositions of Fe and Cr show strong anticorrelation. Upon deformation, the compositional fluctuation is attenuated, as shown in Figure 3(c). To obtain reliable statistics, five profiles were drawn (one is shown as an example in Figure 3(a) and one in Figure 3(c) for the pristine and deformed states, respectively, and values for maxima/minima were recorded and averaged. To normalise the data such that absolute changes in composition with respect to distance through the profile are given, the initial value in each dataset was subtracted. The average wavelength in the pristine state is approximately 7.1 ± 2.8 nm, and the average peak-to-peak amplitude (i.e. change between peak and trough) is 4.9 ± 2.5 at.%. Upon compression, the average wavelength increases slightly to 7.8 ± 3.5 nm, while the average peak-to-peak amplitude decreases by 67% to 1.6 ± 0.6 at.%. The large standard deviations arise due to peculiarities in the distribution induced by the spinodal effect; profiles were drawn in directions that maximises peaks/troughs in all datasets, though given EDS is a 2D technique, more striking patterns in chemical distribution may be found in out-of-plane directions.

In addition to spinodal fluctuations, the BCC alloy also exhibits SRO as expected, which is manifested in the form of atomic strain. Dislocation-free HR STEM images in pre- and post- deformed states are shown in Figure 4(a) and (d), respectively, and the corresponding atomic strain maps are presented in Figure 4(b) and Figure 4(e), respectively, showing a maximum strain peak-to-peak amplitude of 5.5% and 2.1%, respectively (Figure 4(c)). This indicates that the atomic strain decreases after deformation. The average peak-to-peak strain amplitude is 3.03%, which decreases by 48% to 1.59%, determined by measuring and averaging maxima and minima using five profiles in each dataset (one example drawn in Figure 4(b), another in Figure 4(e)). Strain mapping was also applied in regions containing $\frac{1}{2}[\bar{1}11]$ pure edge dislocations and $\frac{1}{2}[1\bar{1}0]$ edge components from $[100]$ mixed dislocations (Figure S 1(a), (c)), revealing corresponding high strains in their respective positions in the strain maps (Figure S 1(b), (d)).

Discussion

Correlating the SRO with strain variations is a well-established technique applied in previous studies. For example, minimal chemical fluctuations are revealed through the atomic strain mapping of the water-quenched CrCoNi alloy with no obvious SRO. In contrast, a higher degree of SRO in the 1000℃ aged CrCoNi alloy leads to enhanced strain fluctuations, suggesting that SRO may be directly associated with changes in the atomic displacements or rearrangements [6]. Similarly, substantial strain fluctuations exist in the CrFeCoNiPd alloy due to presence of the SROs with large composition fluctuation, whereas more uniform atomic strain was observed in CrMnFeCoNi alloy with weak elemental aggregation [4]. In addition to SRO, atomic strain distributions would have dramatic changes in the presence of dislocations or interfaces, which cause additional interruptions to the lattice structure, and therefore to the average atomic positions [14]. Regions free from defects (Figure 4(a) and (d)) were therefore selected to ensure that the strain mapping yields a faithful comparison of the SRO effect. Therefore, the strain fluctuation shown in Figure 4b is a credible indication of the SRO effect. The decreased atomic strain fluctuations in the deformed sample (Figure 4e) show that deformation reduces the degree of SRO.

SRO has been attributed to the increase of yield strength by 25% in a CrCoNi alloy [6]. Unlike the dominance of screw dislocations in dilute BCC alloys, it has been recently observed that the plastic deformation in the BCC CCA can be accommodated by multiple pathways that include operation of non-screw (i.e., edge and mixed) dislocations and activation of multiple slip planes, enabling decent plasticity at room temperature [13]. Meanwhile, the spinodal effect evident on a larger scale also contributes to extra strength in the alloy, whose unique role in alloy strengthening is well known [22]. Combined with SRO, in this work they conceivably pave a more treacherous route promoting wavy dislocations than that offered solely by SRO [16, 17].

As outlined above, the BCC CCA alloy in this work has developed a) larger-scale spinodal-like concentration fluctuations (Figure 3), and b) atomic-scale fluctuations in strain (Figure 4) arising from SRO. Taken together, the alloy possesses a compelling hierarchy of chemical distribution. The first level comes from chemical heterogeneity at the atomic level, including SRO, whereas spinodal decomposition would be

categorised under a higher level; as a complex or precursor emerging on the nanometre scale prior to a second phase becoming identifiable [23]. Hierarchical CCAs are well-documented [24-29]; though these typically feature structural hierarchy [30]. Chemical hierarchies are less documented, though an analysis of the mechanical properties of HfNbTiV alloy with a spinodal structure [16] reported non-uniformities in its atomic strain, and stated that its modulations are larger than those associated with local atomic size and chemical misfit typical of the first level of the chemical heterogeneity [23]. However, the spinodal structure in the HfNbTiV alloy is different to the present alloy, because large variations of strain exist between the two decomposed BCC structures (β and β^*) prior to loading. The secondary β^* phase is enriched in Hf and V, which have dissimilar atomic radii, leading to a much higher internal strain than the β phase ($\pm5\%$, c.f. $\pm1\%$, respectively). Non-uniformity in the strain mapping was also reported, which implies the existence of SRO in-tandem within its spinodal structure. Hierarchies, whether they are structural or chemical in nature, are a vital part of the strategy used to achieve strength-ductility synergy beyond current benchmark ranges [23]. The present CCA achieves a chemical hierarchy by coupling a spinodal structure with innate SRO, allowing a synergy of strengthening effects to occur at multiple length scales.

It was proposed about one hundred years ago by Griffith that a glide plane movement of just one atomic position would alter structuring in the neighbourhood [31]. Later, it was established by different authors that disordering occurs during deformation [32, 33], and can be described mathematically [34]. Under mechanical loading, the first dislocation faces a relatively high energy barrier to slip [35]. When the threshold for the first dislocation to glide is met, the second dislocation requires only a fraction of the original stress (e.g., 10% in a Cu-14.5 at.% Al alloy), and the third dislocation would then glide spontaneously as it releases energy [35]. The subsequent creation of up to one hundred dislocations, all pushed by the trailing dislocation, thus interrupt the SRO structure due to the change in distribution of nearest neighbours [35]. Trailing dislocations following the leading one are not able to restore this order because it exists only over a short range [36]. The resultant change of internal stress distribution would then activate the next sources, and lead to localised and inhomogeneous deformation [36]. The mechanism for the disruption of the spinodal structure could simply be the result of the sum of multiple SRO disruptions over a larger range.

Alternatively, it could be due to severe plastic deformation facilitating high diffusion, and progressing the sample to its equilibrium structure [37, 38]. Overall, the chemical composition in deformed regions tends towards increased randomness (i.e., canonical or ideal high entropy alloy solid solution structure) represented by the sample average composition upon repeated stress-driven dislocation shears on a given slip plane [8].

Plastic deformation has resulted in a 'lattice relaxation' mechanism, whereby fluctuations in composition at both short- and long-range length scales are attenuated (Figure 5). This manifests as a decrease in composition and associated strain amplitudes. By reducing the ruggedness of the dislocation-operating terrain, this mechanism eases the extent of strain hardening in the later stages of deformation (Figure 2(a)). This is consistent with previous observations of SRO disruption leading to glide plane softening [36], correlated to localised planar slip and leading dislocation pairs [6]. Counteracting the decrease in flow stress, the strain hardening response and ductility can be enhanced via cross-slips. Local trapping effects arising due to wavy slip caused by local heterogeneities in CCAs can lead to sustained dislocation pile-up, which are eventually forced to cross-slip [8]. Therefore, the abundance of cross-slips in-tandem with the lattice relaxation mechanism compete against each other to give rise to sustained ductility and circumvent strain localisations and initiation of failure modes, thus generating the relatively flat stress-strain curve observed post high yield point.

Conclusion

A BCC structured $Fe_{72.4}Co_{13.9}Cr_{10.4}Mn_{2.7}B_{0.34}$ alloy possesses a hierarchical chemical structure, featuring SRO at the atomic scale, and a spinodal-like structure of alternating Fe- and Cr- rich regions at the nanoscale. The hierarchical chemical structure allows a synergy of strengthening effects at multiple length scales, improving the alloy's strength and ductility. Upon deformation, the chemical fluctuations on both levels are gradually attenuated. At the atomic scale, this is attributable to the glide plane softening effect, whereby repeated movements of dislocations alter the local atomic ordering and drive it towards a solid solution with more random distribution of alloying species. At the nanoscale, this could be attributed to increased diffusion in the presence of severe plastic deformation driving towards an equilibrium structure. The

attenuated chemical inhomogeneities result in a decreased strain hardening response, evidenced by the relatively flat engineering stress-strain curve. The decrease in strain hardening is nonetheless offset by the competing dislocation behaviour enabled by compositionally complex alloys. Taken together, the new alloy is able to exhibit prolonged ductility by circumventing deleterious strain localisations, all the while maintaining high strength. In so doing this work offers a fresh insight to designing strong, yet tough, alloys for safety-critical load-bearing applications.

Acknowledgements

References

[1] J.W. Yeh, S.K. Chen, S.J. Lin, J.Y. Gan, T.S. Chin, T.T. Shun, C.H. Tsau, S.Y. Chang, Nanostructured high-entropy alloys with multiple principal elements: Novel alloy design concepts and outcomes, Advanced Engineering Materials 6(5) (2004) 299-303+274.
[2] D. Raabe, C.C. Tasan, H. Springer, M. Bausch, From High-Entropy Alloys to High-Entropy Steels, steel research international 86(10) (2015) 1127-1138.
[3] Y. Wu, F. Zhang, X. Yuan, H. Huang, X. Wen, Y. Wang, M. Zhang, H. Wu, X. Liu, H. Wang, S. Jiang, Z. Lu, Short-range ordering and its effects on mechanical properties of high-entropy alloys, Journal of Materials Science & Technology 62 (2021) 214-220.
[4] Q. Ding, Y. Zhang, X. Chen, X. Fu, D. Chen, S. Chen, L. Gu, F. Wei, H. Bei, Y. Gao, M. Wen, J. Li, Z. Zhang, T. Zhu, R.O. Ritchie, Q. Yu, Tuning element distribution, structure and properties by composition in high-entropy alloys, Nature 574(7777) (2019) 223-227.
[5] Z. Lei, X. Liu, Y. Wu, H. Wang, S. Jiang, S. Wang, X. Hui, Y. Wu, B. Gault, P. Kontis, D. Raabe, L. Gu, Q. Zhang, H. Chen, H. Wang, J. Liu, K. An, Q. Zeng, T.G. Nieh, Z. Lu,

Enhanced strength and ductility in a high-entropy alloy via ordered oxygen complexes, Nature 563(7732) (2018) 546-550.

[6] R. Zhang, S. Zhao, J. Ding, Y. Chong, T. Jia, C. Ophus, M. Asta, R.O. Ritchie, A.M. Minor, Short-range order and its impact on the CrCoNi medium-entropy alloy, Nature 581(7808) (2020) 283-287.

[7] Q.-J. Li, H. Sheng, E. Ma, Strengthening in multi-principal element alloys with local-chemical-order roughened dislocation pathways, Nat. Commun. 10(1) (2019) 3563.

[8] E. Ma, Unusual dislocation behavior in high-entropy alloys, Scripta Materialia 181 (2020) 127-133.

[9] H. Li, H. Zong, S. Li, S. Jin, Y. Chen, M.J. Cabral, B. Chen, Q. Huang, Y. Chen, Y. Ren, K. Yu, S. Han, X. Ding, G. Sha, J. Lian, X. Liao, E. Ma, J. Sun, Uniting tensile ductility with ultrahigh strength via composition undulation, Nature 604(7905) (2022) 273-279.

[10] S.I. Rao, C. Varvenne, C. Woodward, T.A. Parthasarathy, D. Miracle, O.N. Senkov, W.A. Curtin, Atomistic simulations of dislocations in a model BCC multicomponent concentrated solid solution alloy, Acta Materialia 125 (2017) 311-320.

[11] L. Lilensten, J.P. Couzinié, L. Perrière, A. Hocini, C. Keller, G. Dirras, I. Guillot, Study of a bcc multi-principal element alloy: Tensile and simple shear properties and underlying deformation mechanisms, Acta Materialia 142 (2018) 131-141.

[12] J. Cairney, A rival to superalloys at high temperatures, Science 370(6512) (2020) 37-38.

[13] S.J. Tsianikas, Y. Chen, J. Jeong, S. Zhang, Z. Xie, Forging strength–ductility unity in a high entropy steel, Journal of Materials Science & Technology 113 (2022) 158-165.

[14] X. Chen, Q. Wang, Z. Cheng, M. Zhu, H. Zhou, P. Jiang, L. Zhou, Q. Xue, F. Yuan, J. Zhu, X. Wu, E. Ma, Direct observation of chemical short-range order in a medium-entropy alloy, Nature 592(7856) (2021) 712-716.

[15] A. Kwiatkowski da Silva, D. Ponge, Z. Peng, G. Inden, Y. Lu, A. Breen, B. Gault, D. Raabe, Phase nucleation through confined spinodal fluctuations at crystal defects evidenced in Fe-Mn alloys, Nature Communications 9(1) (2018) 1137.

[16] Z. An, S. Mao, T. Yang, C.T. Liu, B. Zhang, E. Ma, H. Zhou, Z. Zhang, L. Wang, X. Han, Spinodal-modulated solid solution delivers a strong and ductile refractory high-entropy alloy, Materials Horizons 8(3) (2021) 948-955.

[17] Y.-J. Liang, L. Wang, Y. Wen, B. Cheng, Q. Wu, T. Cao, Q. Xiao, Y. Xue, G. Sha, Y. Wang, Y. Ren, X. Li, L. Wang, F. Wang, H. Cai, High-content ductile coherent nanoprecipitates achieve ultrastrong high-entropy alloys, Nature Communications 9(1) (2018) 4063.

[18] H. Zhang, B.E. Schuster, Q. Wei, K.T. Ramesh, The design of accurate micro-compression experiments, Scripta Materialia 54(2) (2006) 181-186.

[19] J. Peters, JJPPeters/Strainpp: v1.7: Fixed FFT bug, Zenodo (2021).

[20] M.J. Hÿtch, E. Snoeck, R. Kilaas, Quantitative measurement of displacement and strain fields from HREM micrographs, Ultramicroscopy 74(3) (1998) 131-146.

[21] L. Jones, H. Yang, T.J. Pennycook, M.S.J. Marshall, S. Van Aert, N.D. Browning, M.R. Castell, P.D. Nellist, Smart Align—a new tool for robust non-rigid registration of scanning microscope data, Advanced Structural and Chemical Imaging 1(1) (2015) 8.

[22] S. Tsianikas, Y. Chen, J. Jeong, S. Zhang, Z. Xie, Self-toughened high entropy alloy with a body-centred cubic structure, Nanoscale 13(6) (2021) 3602-3612.

[23] E. Ma, X. Wu, Tailoring heterogeneities in high-entropy alloys to promote strength–ductility synergy, Nature Communications 10(1) (2019) 5623.

[24] W. Lu, C.H. Liebscher, G. Dehm, D. Raabe, Z. Li, Bidirectional Transformation Enables Hierarchical Nanolaminate Dual-Phase High-Entropy Alloys, Advanced Materials 30(44) (2018) 1804727.

[25] X. An, Structural hierarchy defeats alloy cracking, Science 373(6557) (2021) 857-858.

[26] Y. Chen, Z. Zhou, P. Munroe, Z. Xie, Hierarchical nanostructure of CrCoNi film underlying its remarkable mechanical strength, Applied Physics Letters 113(8) (2018).

[27] Z. Fu, L. Jiang, J.L. Wardini, B.E. MacDonald, H. Wen, W. Xiong, D. Zhang, Y. Zhou, T.J. Rupert, W. Chen, E.J. Lavernia, A high-entropy alloy with hierarchical nanoprecipitates and ultrahigh strength, Science Advances 4(10) (2018) eaat8712.

[28] S.J. Tsianikas, Y. Chen, Z. Xie, Deciphering deformation mechanisms of hierarchical dual-phase CrCoNi coatings, Journal of Materials Science & Technology 39 (2020) 7-13.
[29] S.H. Albedwawi, A. AlJaberi, G.N. Haidemenopoulos, K. Polychronopoulou, High entropy oxides-exploring a paradigm of promising catalysts: A review, Materials & Design 202 (2021) 109534.
[30] R. Lakes, Materials with structural hierarchy, Nature 361(6412) (1993) 511-515.
[31] A.A. Griffith, The phenomena of rupture and flow in solids, Philosophical Transactions of the Royal Society of London 221 (1921) 163-198.
[32] B.L. Averbach, M.B. Bever, M.F. Comerford, J.S.L. Leach, X-ray and calorimetric investigations of cold working and annealing of a gold-silver alloy, Acta metallurgica 4(5) (1956) 477-484.
[33] P.S. Rudman, B.L. Averbach, The effect of cold work on local order, Acta metallurgica 4(4) (1956) 382-384.
[34] J. Waldman, M. Schwartz, The change of the nearest neighbor short-range order parameter with cold work, Scripta Metallurgica 5(2) (1971) 155-158.
[35] J.B. Cohen, M.E. Fine, Some aspects of short-range order, J. Phys. Radium 23 (1962) 749-762.
[36] V. Gerold, H.P. Karnthaler, On the origin of planar slip in f.c.c. alloys, Acta Metallurgica 37(8) (1989) 2177-2183.
[37] B.B. Straumal, S.G. Protasova, A.A. Mazilkin, E. Rabkin, D. Goll, G. Schütz, B. Baretzky, R.Z. Valiev, Deformation-driven formation of equilibrium phases in the Cu–Ni alloys, Journal of Materials Science 47(1) (2012) 360-367.
[38] A. Alhamidi, K. Edalati, Z. Horita, S. Hirosawa, K. Matsuda, D. Terada, Softening by severe plastic deformation and hardening by annealing of aluminum–zinc alloy: Significance of elemental and spinodal decompositions, Materials Science and Engineering: A 610 (2014) 17-27.
[39] N.D. Stepanov, D.G. Shaysultanov, G.A. Salishchev, M.A. Tikhonovsky, Structure and mechanical properties of a light-weight AlNbTiV high entropy alloy, Materials Letters 142 (2015) 153-155.
[40] O.N. Senkov, G.B. Wilks, J.M. Scott, D.B. Miracle, Mechanical properties of Nb25Mo25Ta25W25 and V20Nb20Mo20Ta20W20 refractory high entropy alloys, Intermetallics 19(5) (2011) 698-706.
[41] S.-P. Wang, J. Xu, TiZrNbTaMo high-entropy alloy designed for orthopedic implants: As-cast microstructure and mechanical properties, Materials Science and Engineering: C 73 (2017) 80-89.
[42] O.N. Senkov, C.F. Woodward, Microstructure and properties of a refractory NbCrMo0.5Ta0.5TiZr alloy, Materials Science and Engineering: A 529 (2011) 311-320.
[43] C.-C. Juan, M.-H. Tsai, C.-W. Tsai, C.-M. Lin, W.-R. Wang, C.-C. Yang, S.-K. Chen, S.-J. Lin, J.-W. Yeh, Enhanced mechanical properties of HfMoTaTiZr and HfMoNbTaTiZr refractory high-entropy alloys, Intermetallics 62 (2015) 76-83.
[44] Z.D. Han, N. Chen, S.F. Zhao, L.W. Fan, G.N. Yang, Y. Shao, K.F. Yao, Effect of Ti additions on mechanical properties of NbMoTaW and VNbMoTaW refractory high entropy alloys, Intermetallics 84 (2017) 153-157.
[45] B. Kang, J. Lee, H.J. Ryu, S.H. Hong, Ultra-high strength WNbMoTaV high-entropy alloys with fine grain structure fabricated by powder metallurgical process, Materials Science and Engineering: A 712 (2018) 616-624.
[46] Y. Long, X. Liang, K. Su, H. Peng, X. Li, A fine-grained NbMoTaWVCr refractory high-entropy alloy with ultra-high strength: Microstructural evolution and mechanical properties, Journal of Alloys and Compounds 780 (2019) 607-617.
[47] S. Wei, S. Kim, J.Y. Kang, Y. Zhang, T. Furuhara, E.S. Park, C.C. Tasan, Natural-mixing guided design of refractory high-entropy alloys with as-cast tensile ductility, Nature Materials (2020) 1-7.
[48] T. Yang, Y.L. Zhao, W.P. Li, C.Y. Yu, J.H. Luan, D.Y. Lin, L. Fan, Z.B. Jiao, W.H. Liu, X.J. Liu, J.J. Kai, J.C. Huang, C.T. Liu, Ultrahigh-strength and ductile superlattice alloys with nanoscale disordered interfaces, Science 369(6502) (2020) 427.

[49] S.J. Sun, Y.Z. Tian, H.R. Lin, H.J. Yang, X.G. Dong, Y.H. Wang, Z.F. Zhang, Achieving high ductility in the 1.7 GPa grade CoCrFeMnNi high-entropy alloy at 77 K, Materials Science and Engineering: A 740-741 (2019) 336-341.

[50] B. Gwalani, S. Gorsse, D. Choudhuri, Y. Zheng, R.S. Mishra, R. Banerjee, Tensile yield strength of a single bulk Al0.3CoCrFeNi high entropy alloy can be tuned from 160 MPa to 1800 MPa, Scripta Materialia 162 (2019) 18-23.

[51] W. Guo, B. Liu, Y. Liu, T. Li, A. Fu, Q. Fang, Y. Nie, Microstructures and mechanical properties of ductile NbTaTiV refractory high entropy alloy prepared by powder metallurgy, Journal of Alloys and Compounds 776 (2019) 428-436.

[52] C. Chen, Y. Fan, H. Zhang, J. Hou, W. Zhang, P. Wei, W. Wang, J. Qin, R. Wei, T. Wang, F. Li, A novel Fe-Co-Ni-Si high entropy alloy with high yield strength, saturated magnetization and Curie temperature, Materials Letters 281 (2020) 128653.

[53] H. Yao, Z. Tan, D. He, Z. Zhou, Z. Zhou, Y. Xue, L. Cui, L. Chen, G. Wang, Y. Yang, High strength and ductility AlCrFeNiV high entropy alloy with hierarchically heterogeneous microstructure prepared by selective laser melting, Journal of Alloys and Compounds 813 (2020) 152196.

[54] W. Lai, F. Vogel, X. Zhao, B. Wang, Y. Yi, D. You, X. Tong, W. Li, X. Yu, X. Wang, Design of BCC refractory multi-principal element alloys with superior mechanical properties, Materials Research Letters 10(3) (2022) 133-140.

[55] N. Yurchenko, E. Panina, D. Shaysultanov, S. Zherebtsov, N. Stepanov, Refractory high entropy alloy with ductile intermetallic B2 matrix / hard bcc particles and exceptional strain hardening capacity, Materialia 20 (2021) 101225.

[56] I.A. Su, K.-K. Tseng, J.-W. Yeh, B. El-Sayed, C.-H. Liu, S.-H. Wang, Strengthening mechanisms and microstructural evolution of ductile refractory medium-entropy alloy Hf20Nb10Ti35Zr35, Scripta Materialia 206 (2022) 114225.

Chapter 7

Conclusion and Future Perspectives

In this chapter, the main outcomes of this thesis will be summarised. Future research arising as a natural progression of the work accomplished so far will be subsequently outlined.

7.1 Conclusions

The deformation mechanisms of multiple CCAs were examined and characterised in detail. A myriad of methods were used, including advanced microscopy techniques (HR STEM, EDS, EBSD, TKD, EELS, PED mapping), micromechanical testing (micropillar compression and nanoindentation), and other characterisation techniques (XRD, APT). The specific outcomes of the thesis are as follows:

1. The deformation behaviour of an equiatomic MEA CrCoNi alloy was characterised. The alloy consists of growth defects, such as stacking faults and twin boundaries, and it possesses FCC phase coexisting with small fractions of

HCP phase and FCC/HCP lamellae. Under indentation, multiple deformation mechanisms were activated in a systematic manner, which were regulated by innate planar defects. The following conclusions can be drawn: *(i)* Where FCC phase is dominant, the deformation process was governed by grain refinement, producing equiaxed nanoscale grains as a result of dislocation activities. *(ii)* In regions where a high fraction of HCP phase exists, high strain localisation was developed due to the lack of slip systems. As such, shear banding took place, facilitated by the presence of high density planar defects. *(iii)* Innate stacking faults, acting as embryos, are responsible for HCP $\rightarrow$ FCC phase transformation under mechanical loading. However, this phase transformation only proceeds after a change in orientation, via grain refinement or shear banding, both of which result in the realignment of the {111} planes. Therefore, the marked plastic response of this alloy is due to the different deformation pathways incorporated over multiple length scales under indentation loading.

2. An exceptional combination of high yield strength ($\sigma_Y \sim 2.55$ GPa) and ductility ($\varepsilon_p \sim 25.2\%$ @ UCS) was achieved in a BCC FeMnCoCr-based iHEA by uniting multiple design strategies. The key findings can be summarised as follows: *(i)* the unique abilities of three interstitial atoms (B, C and O) were harnessed to enhance the phase stability and facilitate the grain refinement process during deformation. *(ii)* The deformed structure contains highly refined grains, and short-range compositional fluctuations giving rise to appreciable lattice distortions that contribute to strain hardening. *(iii)* The alloy exhibits appreciable ductile behaviour via undergoing a two-step phase transformation upon deformation; first from BCC to HCP phase governed by a plane shearing and shuffling mechanism observing a Pitch-Schrader orientation relationship, and

then from HCP to FCC phase catalysed by stacking fault formation. (iv) The resultant HCP/FCC nanolamellar structure with a high density of planar defects (i.e. stacking faults, twin boundaries and phase boundaries), triggers self-hardening by impeding dislocation motion.

3. Nanoscale compositional fluctuations were exploited in conjunction with interstitial element additions and grain boundary segregation to create a strong and yet ductile BCC structured high entropy steel. An inverse relationship exists in spatial distribution between Fe and Cr contents, with the composition of each element fluctuating by up to 20%. The yield strength was determined using in-situ micropillar compression tests to be 2.92 ± 0.36 GPa, with a plasticity value of 13.7 ± 1.9% obtained at the ultimate compressive strength. Multiple slip systems were found to be active, evidenced by a high abundance of $\frac{1}{2}[\bar{1}11]$ pure edge dislocations with a slip plane of $(\bar{1}1\bar{2})$ co-operating with $[100]$ mixed dislocations with a $\frac{1}{2}[1\bar{1}0]$ edge component and a $\frac{1}{2}[110]$ screw component. Meanwhile, multiple shear events occurred steadily. The results shed light on the extent of compositional/structural control that can be exploited to achieve strength–ductility unity in BCC based high entropy steel.

4. The effect of deformation has on a BCC structured $Fe_{72.4}Co_{13.9}Cr_{10.4}Mn_{2.7}B_{0.34}$ alloy with a hierarchical chemical structure, featuring SRO at the atomic scale, and a spinodal structure of Fe- and Cr- rich regions at the nanoscale, was investigated. The hierarchical chemical structure allows a synergy of strengthening effects at multiple length scales, improving the alloy's strength and ductility. Upon deformation, the chemical fluctuations on both levels are gradually attenuated, which at the atomic scale is attributable to the glide plane

softening effect, whereby repeated movements of dislocations alter the local atomic ordering, and drive it towards a solid solution with more random distribution of alloying species, and at the nanoscale could be attributed to increased diffusion in the presence of severe plastic deformation driving towards an equilibrium structure. The attenuated chemical inhomogeneities presumably result in a decreased strain hardening response, evidenced by the relatively flat engineering stress-strain curve. The decrease in strain hardening is nonetheless offset by the competing dislocation behaviour enabled by compositionally complex alloys. Taken together, the new alloy is able to exhibit prolonged ductility by circumventing deleterious strain localisations, all the while maintaining high strength. In so doing this work offers a fresh approach to designing strong, yet tough, alloys for safety-critical load-bearing applications.

7.2 Future Perspectives

The mechanical properties of the alloys studied in this thesis were measured successfully, however, additional micromechanical testing techniques could be applied on the alloys to achieve a more comprehensive characterisation, rather than inferring mechanical response from compression tests and displayed plasticity alone. Examples of further testing techniques that could be applied includes tensile testing, and fracture toughness testing. These tests, in addition to compressive tests, could also be performed at elevated or cryogenic temperatures, to examine how the alloys would behave under extreme conditions. Due to the strong columnar texture of the alloys, it will be necessary to conduct further tests on equivalent bulk samples to explore the expected anisotropy of the mechanical properties. Other useful properties, such as wear resistance, oxidation resistance, electric resistivity, and corrosion resistance, could also be probed. Furthermore, in-situ experiments of dynamic factors, such as dislocation motion and phase transformations, could also be employed to examine

these phenomena directly, rather than by piecing together snapshots at various stages of deformation. Lastly, while Chapter 6 examined relative changes in SRO, this was not investigated in any of the preceding work. It would be beneficial to examine this in greater detail in future studies to unearth its contribution to the strengthening and deformation behaviours of those alloys. Additional structural information about the SRO in Chapter 6 (e.g. via analyses of superlattice reflections, probability density function calculations, or pair correlation coefficient calculations) could be investigated to complement the strain mapping measurements. Finally, chemical hierarchy in CCAs can be further expanded through investigations into the presence and extent of any medium range order [65] in these alloys, in addition to SRO and spinodal structures.

FeMnCoCrB-based alloys were a large focus of work in this thesis, and while the number of further improvements that could be made to this particular material via selection of alloying elements is limited, probing the FeMnCoCrB compositional space further will yield further improvements to its properties. Synthesising and testing the performance of materials one-by-one is an inefficient approach in the search for new materials. To accelerate this process, combinatorial deposition techniques such as co-sputtering, and high-throughput characterisation techniques, could be used. Combinatorial deposition could allow for the creation of coatings with unique, multi-directional composition profiles. This can be achieved by evaporating pure element 'targets' in a low-pressure chamber and depositing those elements onto a substrate in a non-uniform way so as to create a compositional gradient with the possibility to cover the entire phase diagram composition. Meanwhile, automation of high throughput characterisation to measure hardness, modulus of elasticity (i.e. stiffness), and crystal structure, can be determined using associated instruments with programmable sample-positioning stages [66]. Doing so could rapidly contribute insight to the design and evolution of CCAs.

Appendix A

XRD Calculations

In this appendix, the peaks from the XRD spectrum provided in the supplementary data for Paper #1 are indexed.

No.	2-theta(deg)	d(ang.)	Height(cps)	FWHM(deg)	Int. I(cps deg)	Int. W(deg)	Asym. factor
1	39.696(13)	2.2688(7)	5556(215)	0.17(3)	1623(75)	0.29(2)	1.1(5)
2	44.184(3)	2.04814(13)	871795(2695)	0.222(2)	243845(1183)	0.280(2)	1.84(11)

For Peak #2;

2θ = 44.18°, and d = 2.048 $\mathring{A}$ = 0.2048 nm.

$$d_{hkl} = \frac{a}{\sqrt{h^2 + k^2 + l^2}}$$

A1

The atomic radii of Ni, Co and Cr are all 0.125 nm. From HRTEM, the two phases present are HCP and FCC. The FCC phase will be tested first, for which the lattice constant is equal to:

$$a = 2\sqrt{2}\,r = 2(0.125)\sqrt{2} \approx 0.3536\,nm$$

Therefore,

$$h^2 + k^2 + l^2 = \left(\frac{a}{d_{hkl}}\right)^2 = \left(\frac{0.3536}{0.2048}\right)^2 = 2.980 \approx 3$$

In FCC crystal structures, *h, k* & *l* are all odd or all even. The only integers therefore to satisfy this equation are *h = k = l = 1*.

Hence, the peak at 2θ = 44.18° is the FCC (111) plane.

Peak #1 of 39.7° is a peak of negligible magnitude, and yields $h^2 + k^2 + l^2$ values of 2.43, 1.61 and 1.21 for FCC, BCC and HCP crystal structures respectively. These numbers are all non-integer values, and therefore cannot be indexed.

Appendix B

Error Analysis

All measured data are subject to inevitable scatter and variability at different regions of the same material even under the highly controlled environment, homogenous elemental distribution afforded by RFMS, and the precision of a nanoindenter. The average value of data sets was obtained by dividing the sum of all measured values by the number of measurements taken. The sample standard deviation s is determined using the equation B1 for n number of observations for parameter x and its corresponding average $\bar{x}$. Sample standard deviation was used instead of population standard deviation, as only finite sections of the sample were analysed.

$$s = \left[\frac{\sum_{i=1}^{n}(x_i - \bar{x})^2}{n-1}\right]^{\frac{1}{2}}$$

B1

Appendix C

CaRST Accreditation

I confirm that I have completed the required 120 hours within the four domains, as outlined in the Completion Certificate.

THE UNIVERSITY
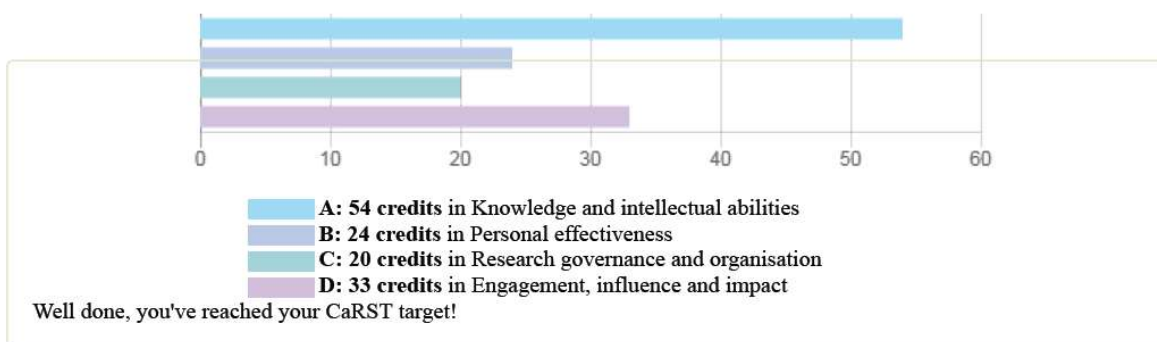*of* ADELAIDE

This is to certify that

Mr Simon Tsianikas

has completed

120 hours

of Career and Research Skills Training

24 Jan 2022
Date

Dr Monica Kerr,
Director, Career and Research Skills Training

adelaide.edu.au   CRICOS Provider Number 00123M

seek LIGHT

CaRST Credits Overview

A: **54 credits** in Knowledge and intellectual abilities
B: **24 credits** in Personal effectiveness
C: **20 credits** in Research governance and organisation
D: **33 credits** in Engagement, influence and impact

Well done, you've reached your CaRST target!

Date	Title / Summary	Total Credits	Domains	Approval Status	
09 Feb 17	Postgraduate Research Induction	2	Domain B -		
09 Mar 17	CaRST Launch	1	Domain B		
17 Mar 17	Manual Handling & Ergonomics	1	Domain C -		
05 Apr 17	CaRST Information Session	1	Domain C		
19 Apr 17	Preparing your Research Data Management Plan: Lecture	1	Domain C		
20 Apr 17	Leadership and the Art of Influence	3	Domain D		
21 Apr 17	Seven Secrets of Highly Successful Research Students	3	Domain B		
25 May 17	Create your Researcher Profile	2	Domain B		
30 May 17	Effective Journal Writing	8	Domain A -		
08 Jun 17	Managing an HDR Thesis with Word - Lecture	1	Domain A		

| Date	Event		Domain	
20 Jun 17	LinkedIn Lab	1	Domain B -	
03 Jul 17	Stand up, Speak up and Persuade	3	Domain D	
12 Jul 17	Australian-French Entrepreneurship Challenge	20	Domain D	
13 Jul 17	Handling Difficult Conversations Well	3	Domain D	
19 Jul 17	ANSYS FEA Training	21	Domain A -	
20 Jul 17	Core Component of the Structured Program (CCSP)	19	Domain B Domain C -	
12 Oct 17	Engaging with Industry	2	Domain D	
20 Oct 17	IP 101	1	Domain C	
03 Nov 17	Climathon 2017	24	Domain A -	
07 Dec 17	Emerging Leader: Communicating for Impact	2	Domain D	
09 Aug 18	Demystifying Research Metrics - Lecture	0	Domain A	
10 Sep 18	Conferences and Symposia - Attendance	12	Domain B	Approved

Appendix D

Supplementary Data for Publication #1
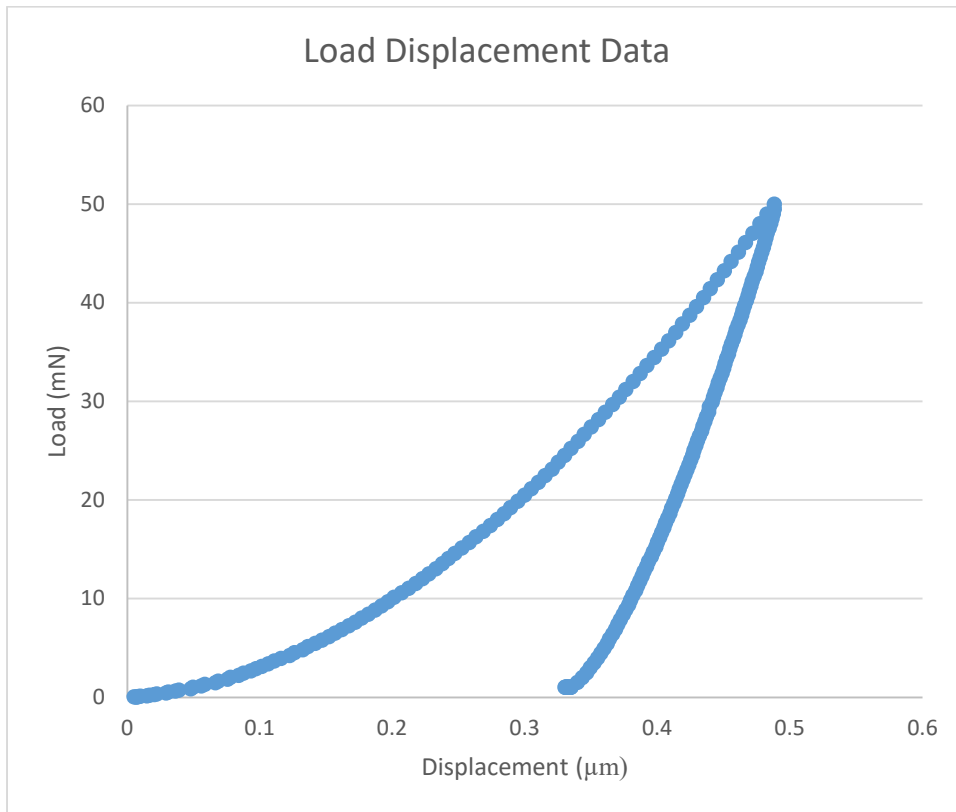
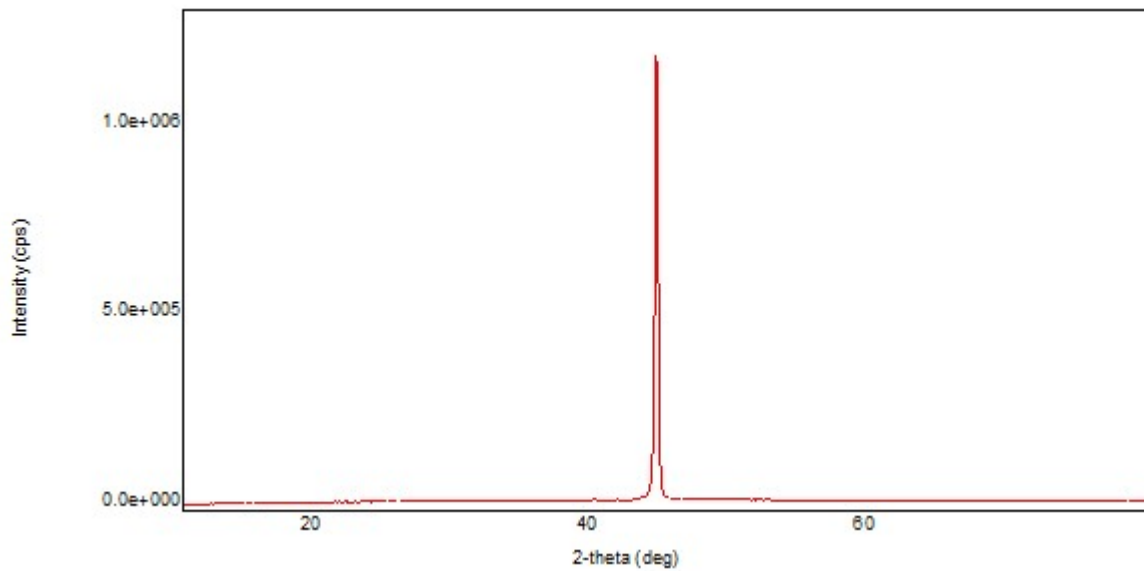*Figure S 1: Load-displacement curve for nanoindentation data.*

Figure S 2: X-Ray Diffraction Pattern of the CrCoNi alloy.

Appendix E

Supplementary Data for Publication #2

Supporting Information
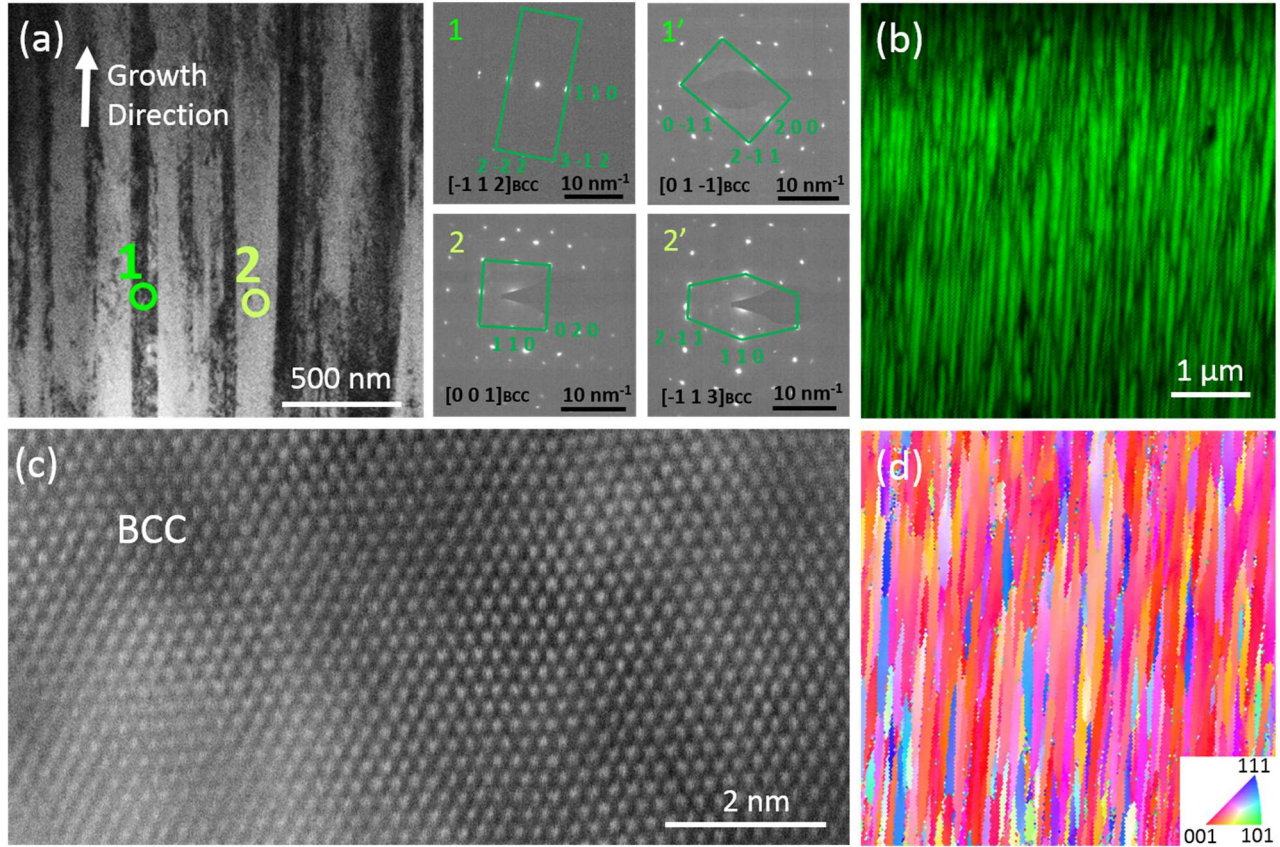**Verification of the BCC Crystal Structure**

Figure A 1: (a) bright-field transmission electron microscope image showing columnar grain structure showing the grains in which diffraction patterns 1 and 2 where collected. Diffraction patterns 1' and 2' were collected from the same grains, but at different tilts; (b) EBSD results, where the colour green is indexed to the BCC phase, and (d) the corresponding Inverse Pole Figure map; (c) a typical STEM image showing the BCC structure along the [-1 1 1] zone axis.

To verify the crystal structure as BCC (in conjunction with TKD and EBSD data), a series of diffraction patterns were collected and indexed. In Figure A 1, diffraction patterns 2 and 2', indexed as $[0\ 0\ 1]_{BCC}$ and $[-1\ 1\ 3]_{BCC}$ were collected at α tilts of $-29.24°$ and $-4.42°$, respectively, with the β tilt being held constant. The absolute difference in angles between these two patterns is $|(-29.24) - (-4.42)| = 24.82°$.

The angle between two vectors, denoted here as *a* and *b,* is given by;

$$cos\theta = \frac{\tilde{a} \cdot \tilde{b}}{\|a\|\|b\|}$$

E1

Thus,

$$\theta = \cos^{-1} \frac{[0\ 0\ 1] \cdot [-1\ 1\ 3]}{\sqrt{0^2 + 0^2 + 1^2} * \sqrt{(-1)^2 + 1^2 + 3^2}} \approx 25.2°$$

Hence, as the theoretical (25.2°) and experimental (24.8°) values are in close agreement with each other, this provides additional confirmation that the crystal structure is BCC.

Calculation of the Lattice Parameter

The lattice parameter of BCC was calculated using XRD data. First, the interplanar spacing, d, can be determined via Braggs Law in equation E2, viz.

$$2d \sin \theta = n\lambda \qquad\qquad E2$$

Here, θ is the angle of diffraction, n is the order of reflection, and λ is the wavelength of the incident x-ray, viz. $1.7889 \times 10^{-10}\ m$. The major peak in the XRD data is the $(1\ 1\ 0)_{BCC}$ reflection occurring at $2\theta = 52.2°$, thus yielding;

$$d = \frac{n\lambda}{2 sin\theta} = \frac{(1)(1.7889 \times 10^{-10}\ m)}{2 \sin\left(\frac{52.2}{2}\right)} \approx 2.033 \times 10^{-10}\ m$$

Then, equation E3 is applied to obtain the lattice parameter.

$$d_{hkl} = \frac{a}{\sqrt{h^2 + k^2 + l^2}}$$

$$E3$$

Here, d_{hkl} is the interplanar spacing with corresponding h, k, and l Miller indices, and a is the lattice parameter.

$$a = d_{hkl}\sqrt{h^2 + k^2 + l^2} = (2.033 \times 10^{-10}\ m)\left(\sqrt{1^2 + 1^2 + 0^2}\right) \approx 0.288\ nm$$

This value was subsequently used to calculate the atomic radius, which was used to determine the corresponding lattice parameters of FCC and HCP. These calculated lattice parameters were used to create block files used in the diffraction mapping; further details of which are available in the Experimental section.
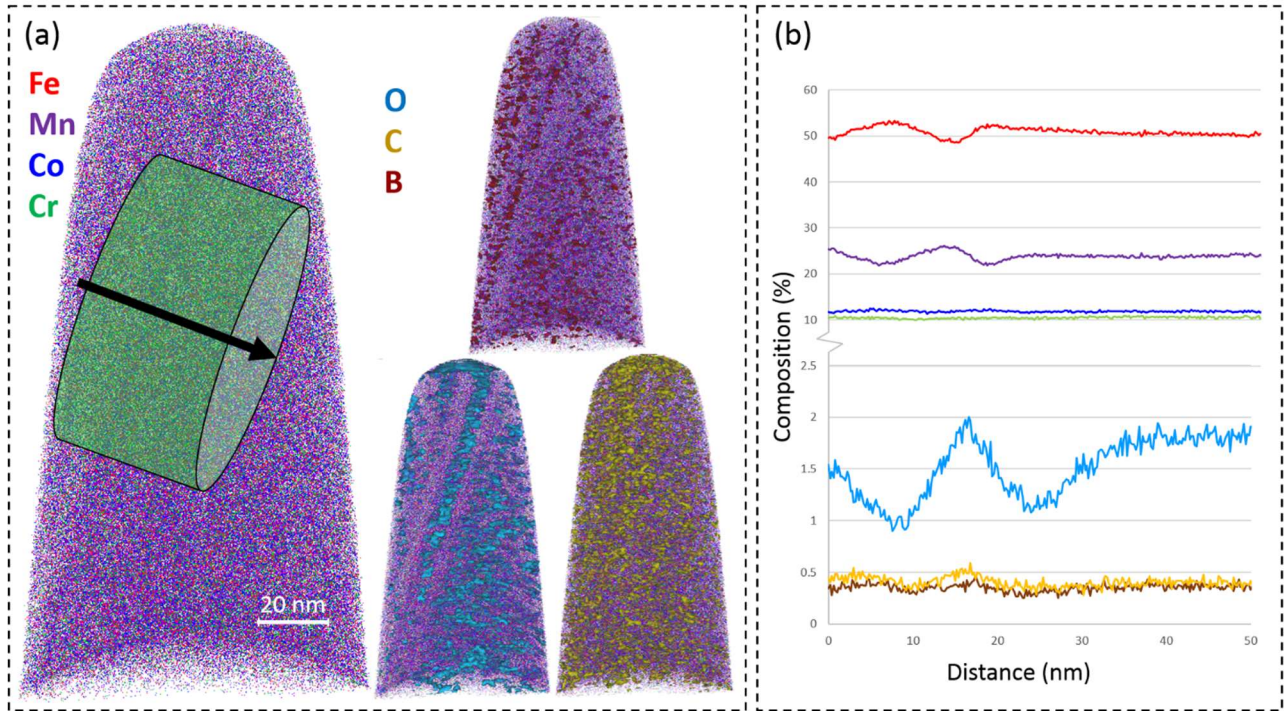
Supplementary APT Data

Figure C 1: (a) additional atom probe tomography reconstruction (left) showing Fe, Mn, Co and Cr, with B (0.8% threshold), C (1.0% threshold) and O (3.0% threshold) isosurfaces (right), and (b) 1D concentration line profiles displaying elemental segregation along the grain boundary (GB) along the arrow integrating over the cylinder cross section. Here, the inverse relationship between iron and manganese is more prominent.

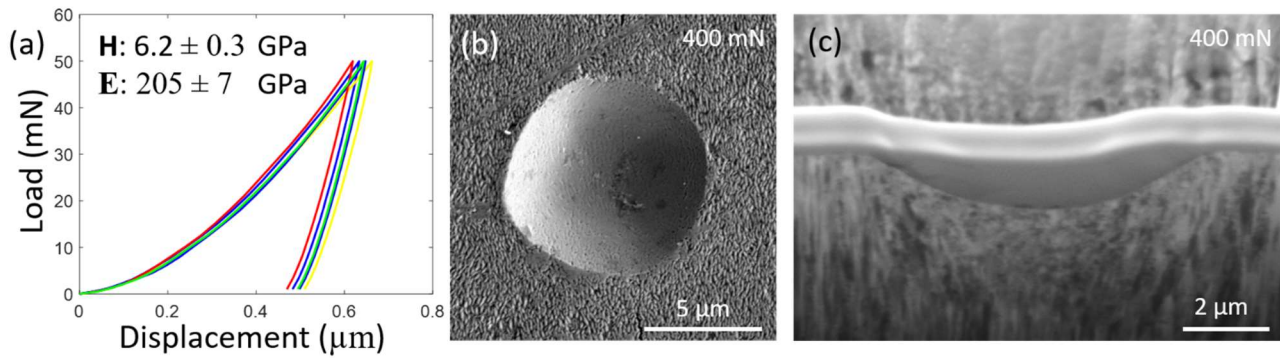**Nanoindentation Load-Displacement Curves**

Figure D 1: (a) Load-displacement curves of the iHEA sample under a load of 50 mN (five data sets out of twenty shown) with the averaged hardness and Young's modulus indicated, (b) SEM image of spherical indentation impression on the surface and (c) cross-section of the indent imaged during FIB milling.
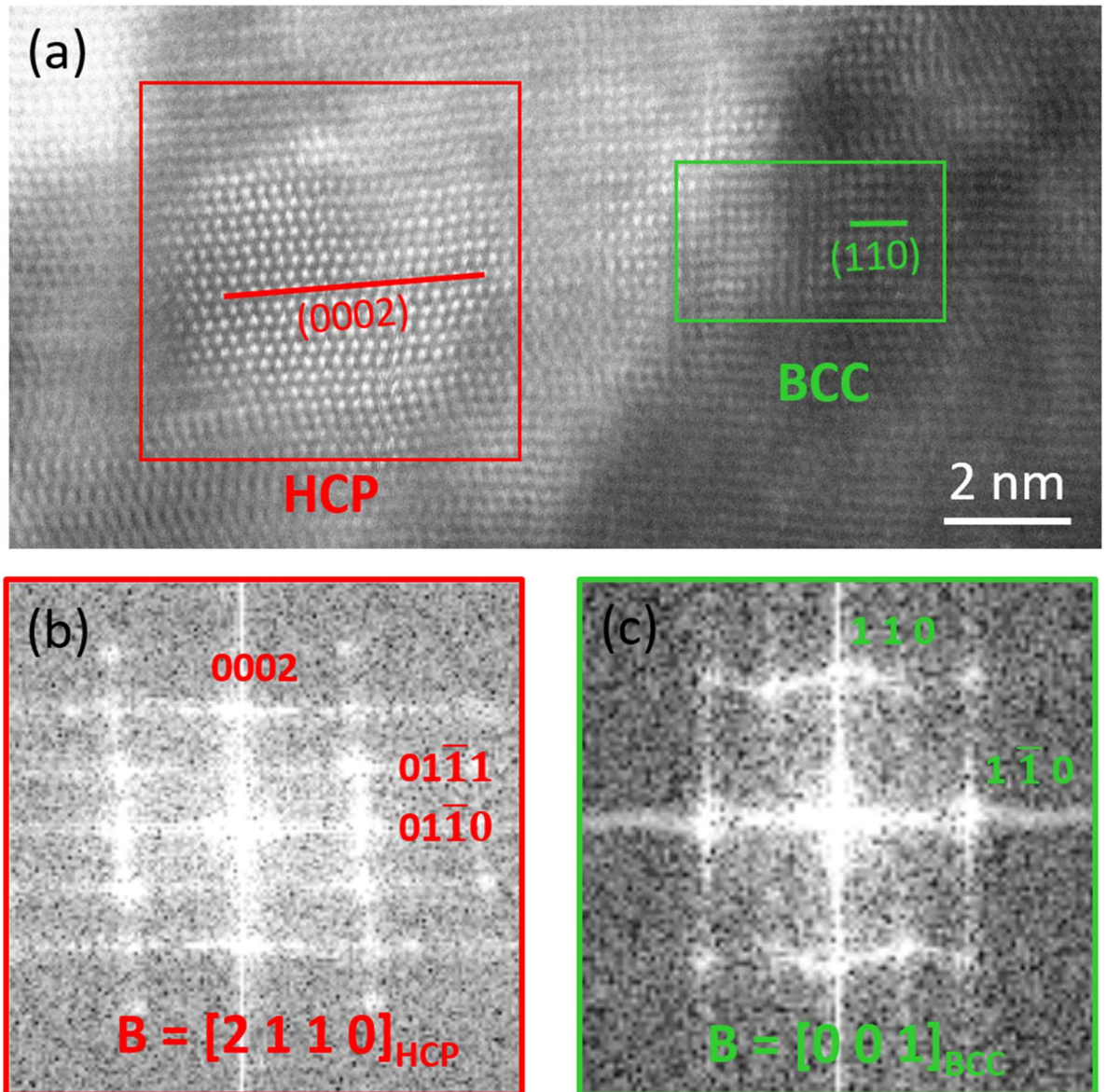
BCC || HCP Orientation Relationship

Figure E 1: $[2\bar{1}\bar{1}0]_{HCP}||[001]_{BCC}$ *Orientation relationship between BCC and HCP; (a) STEM imaging showing respective regions, and (b) & (c) FFT from selected representative regions with the indicated zone axis, B.*

Mechanical Property Data

Table 1: Summary of mechanical property data for selected high-strength HEAs used to create the comparison figure in Publication #2.

| Alloy Composition	Strain	Strength	Source
AlNbTiV	5.0	1020	[67]
NbMoTaWV	1.7	1246	[68]
TiZrNbTaMo	6.0	1390	[69]
$NbCrMo_{0.5}Ta_{0.5}TiZr$	5.0	1595	[70]
HfMoNbTaTiZr	10.0	1512	[71]
NbMoTaWVTi	10.6	1515	[72]
NbMoTaWTi	14.1	1343	[72]
WNbMoTaV	8.8	2612	[73]
NbMoTaWVCr	5.3	3416	[74]
TiVNbHf	16.1	1004	[75]
$Ti_{38}V_{15}Nb_{23}Hf_{24}$	22.5	802	[75]
$Ni_{43.9}Co_{22.4}Fe_{8.8}Al_{10.7}Ti_{11.7}B_{2.5}$	25	1040	[76]
CoCrFeMnNi	1.1	1210	[77]
$Al_{0.3}CoCrFeNi$	5.0	1800	[78]
NbTaTiV	23	1370	[79]
$Fe_{40}Co_{40}Ni_{10}Si_{10}$	38.3	1100	[80]
$Fe_{51.2}Mn_{24.3}Co_{11.9}Cr_{10.1}O_{1.4}C_{0.3}B_{0.2}$	28.9	2500	This Work

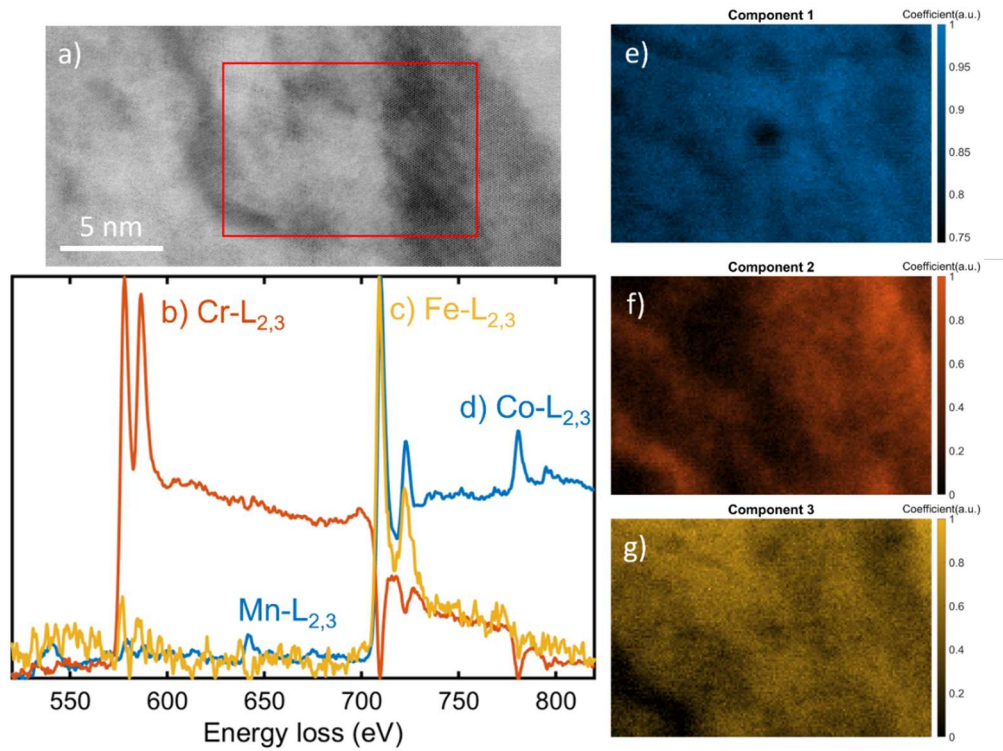# Appendix F

Supplementary Data for Publication #3
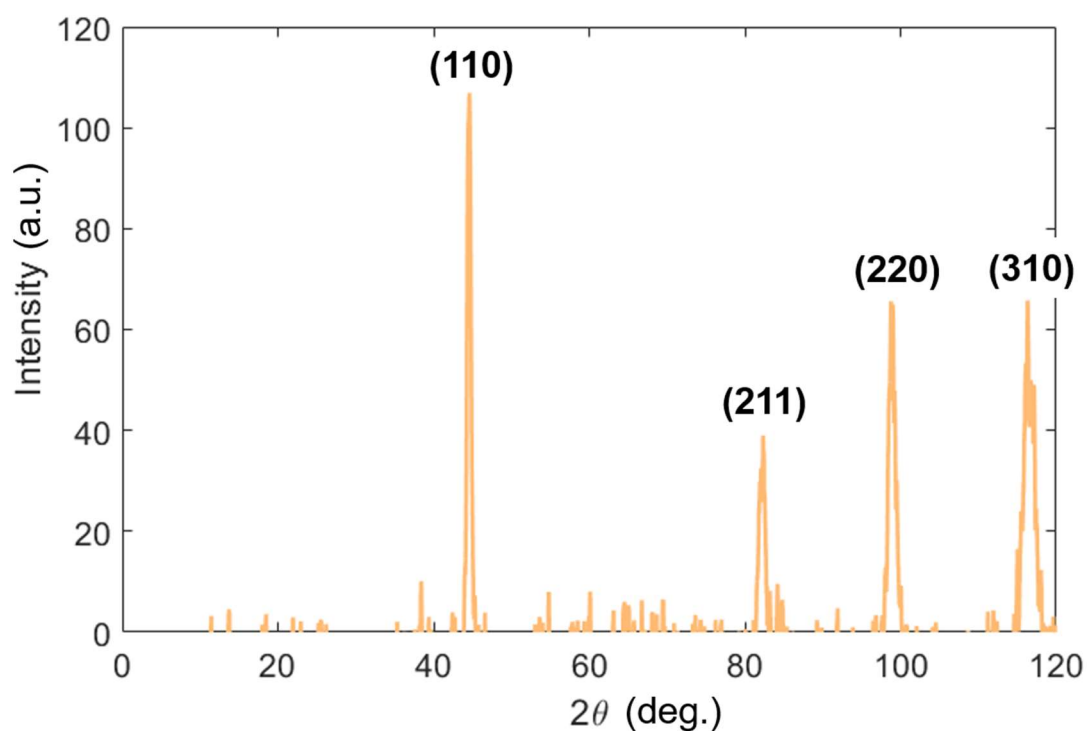
Fig. S3. X-ray diffraction (XRD) pattern obtained from the high entropy steel, featuring a body-centered cubic (BCC) crystal structure.
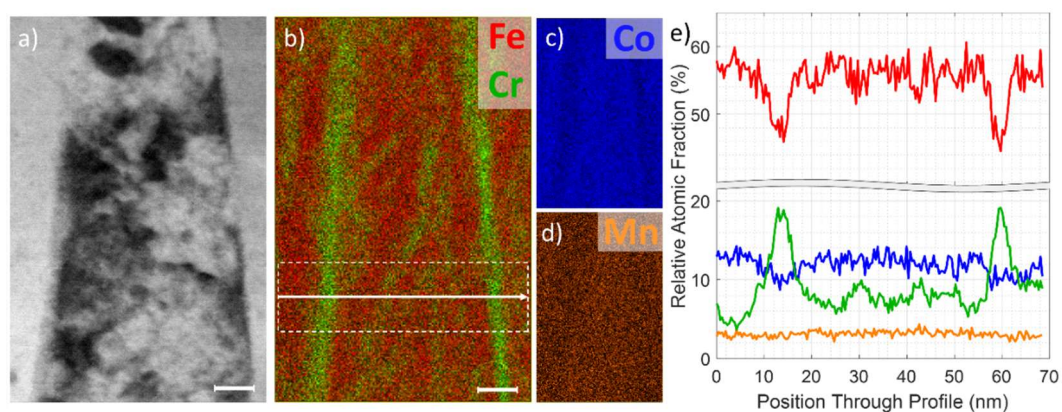
Fig. S4. (a) HAADF STEM image of grain in the undeformed sample, (b) EDS map of Fe and Cr, (c) Co, (d) Mn, and (e) compositional profile through the while box indicated in (b). The scale bar is 20 nm.

Fig. S5. Electron energy loss spectroscopy (EELS) spectrum imaging dataset (red box in (a)), and the statistical analysis by non-negative matrix factorization [62] into three major spectral components: (b), (c) and (d), with their corresponding weighting maps shown in (f), (g) and (e), respectively.
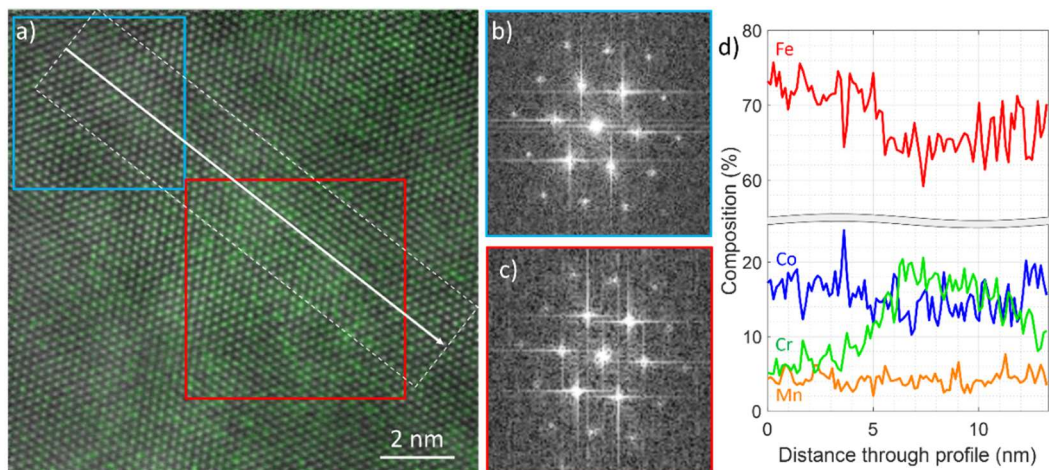
**Fig. S6.** (a) Drift corrected frame integration (DCFI) high-angle annular dark-field (HAADF) high-resolution scanning transmission electron microscopy (HR-STEM) image from the undeformed sample overlayed onto an energy dispersive spectroscopy (EDS) map of Cr, with corresponding fast Fourier transforms (FFTs) from Cr-deficient (b) and Cr-rich (c) regions, and (d) compositional profile of Fe, Mn, Co and Cr through the white rectangle box drawn in (a).
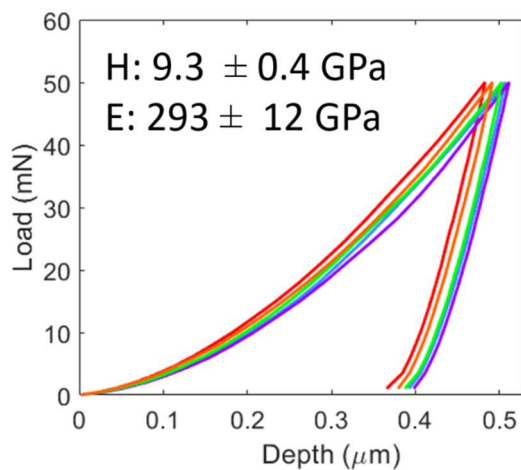
Fig. S7. Load–displacement curves obtained during nanoindentation tests (each color represents a different data set), with H and E values (top–left) determined by averaging the results of twenty tests.
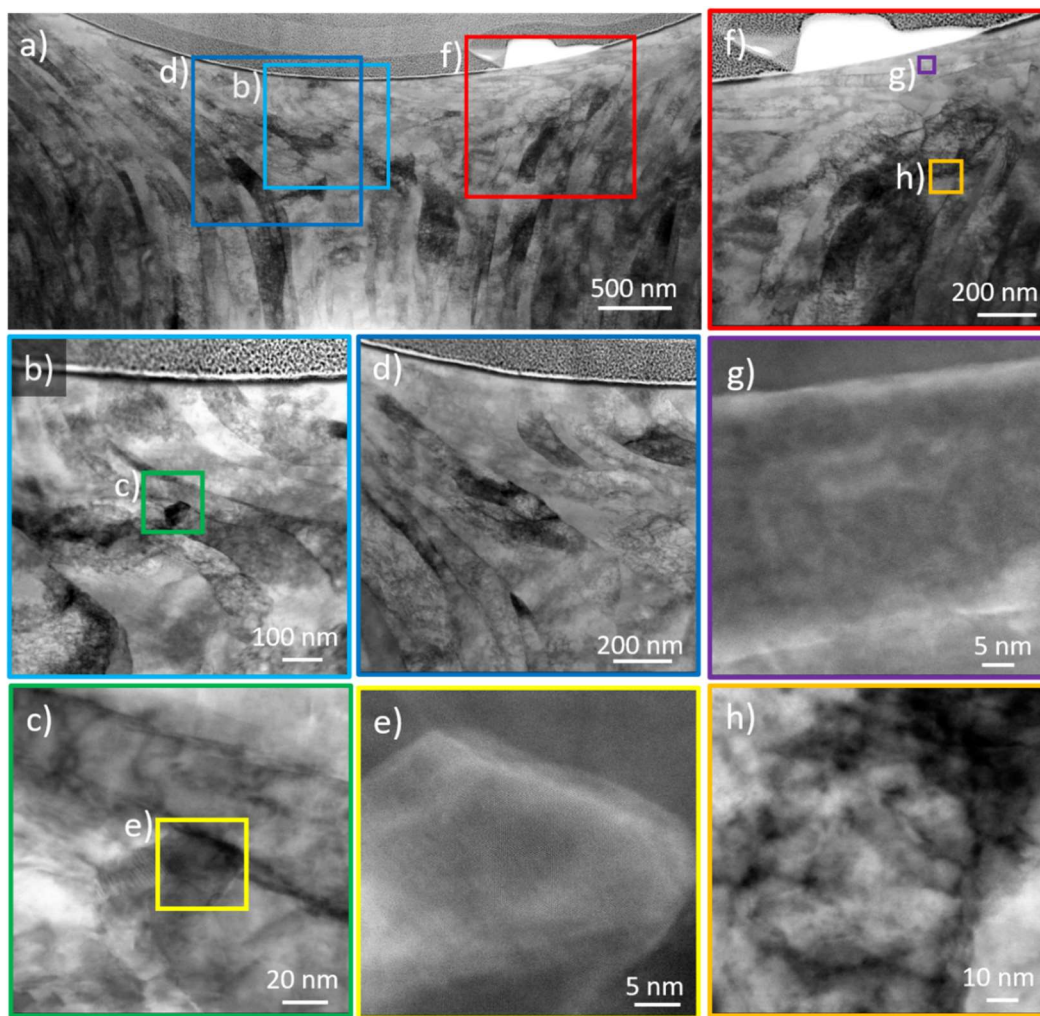
Fig. S8. (a–h) STEM images showing the deformation substructure and grain morphology of the high entropy steel deformed at 400 mN. Locations of images (b–h) are indicated via colored boxes and labels in corresponding images.

Appendix G

Supplementary Data for Publication #4
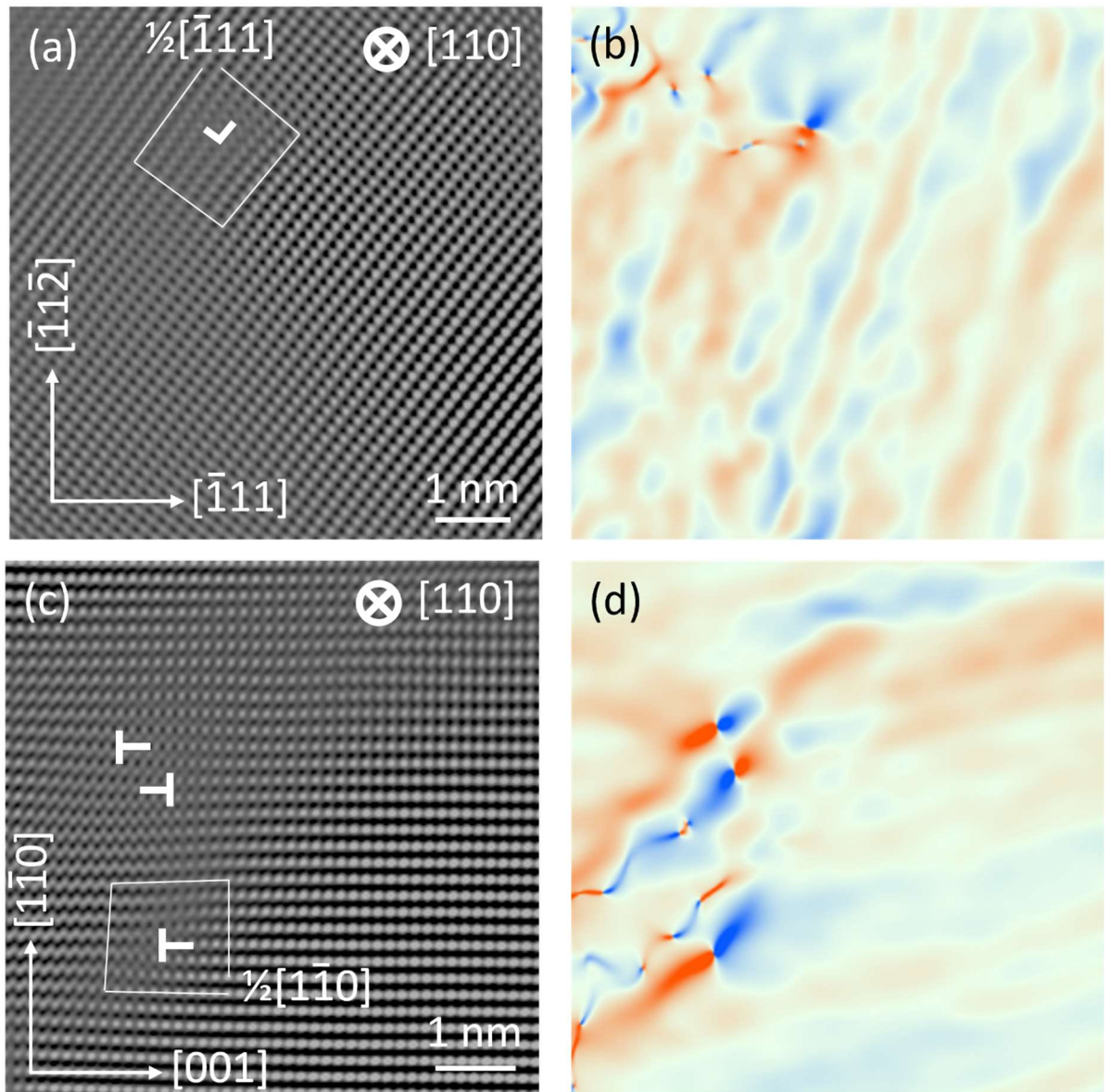
Figure S 9: Strain mapping of dislocations imaged in the shear region of the post-mortem pillar sample along the [110] zone axis; (a) $\frac{1}{2}[\bar{1}11]$ pure edge dislocation with (b) corresponding strain map showing strain at the dislocation site, (c) $\frac{1}{2}[1\bar{1}0]$ edge components from [100] mixed dislocations and (d) corresponding strain map showing dislocation-induced strain. TEM images shown in (a) and (c) have been filtered by inverse fast Fourier transform to show the dislocations clearly, whereas their original counterparts were used to generate the strain map.

Table S1: Summary of mechanical property data for selected high-strength compositionally complex alloys used to create the Ashby plot in Figure 2(b).

Alloy	Strain (%)	Strength (MPa)	Source
AlNbTiV	5.0	1020	[67]
NbMoTaWV	1.7	1246	[68]
TiZrNbTaMo	6.0	1390	[69]
$NbCrMo_{0.5}Ta_{0.5}TiZr$	5.0	1595	[70]
HfMoNbTaTiZr	10.0	1512	[71]
NbMoTaWVTi	10.6	1515	[72]
NbMoTaWTi	14.1	1343	[72]
WNbMoTaV	8.8	2612	[73]
NbMoTaWVCr	5.3	3416	[74]
TiVNbHf	16.1	1004	[75]
$Ti_{38}V_{15}Nb_{23}Hf_{24}$	22.5	802	[75]
$Ni_{43.9}Co_{22.4}Fe_{8.8}Al_{10.7}Ti_{11.7}B_{2.5}$	25	1040	[76]
CoCrFeMnNi	1.1	1210	[77]
$Al_{0.3}CoCrFeNi$	5.0	1800	[78]
NbTaTiV	23	1370	[79]
$Fe_{40}Co_{40}Ni_{10}Si_{10}$	38.3	1100	[80]
AlCrFeNiV	30.3	1057	[81]
$Ti_{35}Zr_{35}Nb_{10}Ta_{15}Mo_5$	19.1	1110	[82]
$Nb_{30}Mo_{30}Hf_{20}Co_{20}$	10	1180	[83]
$Hf_{20}Nb_{10}Ti_{35}Zr_{35}$	8.7	884	[84]
$Fe_{51.2}Mn_{24.3}Co_{11.9}Cr_{10.1}O_{1.4}C_{0.3}B_{0.2}$	28.9	2500	[85]
$Fe_{72.4}Cr_{13.9}Mn_{24.3}Co_{10.4}B_{0.34}$	13.7	2920	This Work

Bibliography

[1] W. Callister, D. Rethwisch, Materials Science and Engineering An Introduction, 9 ed., Wiley, United States of America, 2014.

[2] L.J. Santodonato, Y. Zhang, M. Feygenson, C.M. Parish, M.C. Gao, R.J.K. Weber, J.C. Neuefeind, Z. Tang, P.K. Liaw, Deviation from high-entropy configurations in the atomic distributions of a multi-principal-element alloy, Nature Communications 6 (2015).

[3] B. Cantor, I.T.H. Chang, P. Knight, A.J.B. Vincent, Microstructural development in equiatomic multicomponent alloys, Materials Science and Engineering: A 375-377 (2004) 213-218.

[4] J.W. Yeh, S.K. Chen, S.J. Lin, J.Y. Gan, T.S. Chin, T.T. Shun, C.H. Tsau, S.Y. Chang, Nanostructured high-entropy alloys with multiple principal elements: Novel alloy design concepts and outcomes, Advanced Engineering Materials 6(5) (2004) 299-303+274.

[5] Y. Zhang, T.T. Zuo, Z. Tang, M.C. Gao, K.A. Dahmen, P.K. Liaw, Z.P. Lu, Microstructures and properties of high-entropy alloys, Progress in Materials Science 61 (2014) 1-93.

[6] D.B. Miracle, O.N. Senkov, A critical review of high entropy alloys and related concepts, Acta Materialia 122 (2017) 448-511.

[7] J.W. Yeh, Recent progress in high-entropy alloys, Annales de Chimie: Science des Materiaux 31(6) (2006) 633-648.

[8] Z. Li, D. Raabe, Strong and Ductile Non-equiatomic High-Entropy Alloys: Design, Processing, Microstructure, and Mechanical Properties, JOM 69(11) (2017) 2099-2106.

[9] B. Gludovatz, A. Hohenwarter, K.V.S. Thurston, H. Bei, Z. Wu, E.P. George, R.O. Ritchie, Exceptional damage-tolerance of a medium-entropy alloy CrCoNi at cryogenic temperatures, Nature Communications 7 (2016).

[10] G. Laplanche, A. Kostka, C. Reinhart, J. Hunfeld, G. Eggeler, E.P. George, Reasons for the superior mechanical properties of medium-entropy CrCoNi compared to high-entropy CrMnFeCoNi, Acta Materialia 128 (2017) 292-303.

[11] X.R. Wang, Z.Q. Wang, W.S. Li, T.S. Lin, P. He, C.H. Tong, Preparation and microstructure of CuNiTiZr medium-entropy alloy coatings on TC11 substrate via electrospark – computer numerical control deposition process, Materials Letters 197 (2017) 143-145.

[12] S. Yoshida, T. Bhattacharjee, Y. Bai, N. Tsuji, Friction stress and Hall-Petch relationship in CoCrNi equi-atomic medium entropy alloy processed by severe plastic deformation and subsequent annealing, Scripta Materialia 134 (2017) 33-36.

[13] Z. Zhang, H. Sheng, Z. Wang, B. Gludovatz, Z. Zhang, E.P. George, Q. Yu, S.X. Mao, R.O. Ritchie, Dislocation mechanisms and 3D twin architectures generate exceptional strength-ductility-toughness combination in CrCoNi medium-entropy alloy, Nature Communications 8 (2017).

[14] Y. Deng, C.C. Tasan, K.G. Pradeep, H. Springer, A. Kostka, D. Raabe, Design of a twinning-induced plasticity high entropy alloy, Acta Materialia 94 (2015) 124-133.

[15] Y. Chen, D. Chen, X. An, Y. Zhang, Z. Zhou, S. Lu, P. Munroe, S. Zhang, X. Liao, T. Zhu, Z. Xie, Unraveling dual phase transformations in a CrCoNi medium-entropy alloy, Acta Materialia 215 (2021) 117112.

[16] Z. Li, C.C. Tasan, H. Springer, B. Gault, D. Raabe, Interstitial atoms enable joint twinning and transformation induced plasticity in strong and ductile high-entropy alloys, Scientific Reports 7(1) (2017) 40704.

[17] D. Raabe, C.C. Tasan, H. Springer, M. Bausch, From High-Entropy Alloys to High-Entropy Steels, steel research international 86(10) (2015) 1127-1138.

[18] Z. Lei, X. Liu, Y. Wu, H. Wang, S. Jiang, S. Wang, X. Hui, Y. Wu, B. Gault, P. Kontis, D. Raabe, L. Gu, Q. Zhang, H. Chen, H. Wang, J. Liu, K. An, Q. Zeng, T.G. Nieh, Z. Lu, Enhanced strength and ductility in a high-entropy alloy via ordered oxygen complexes, Nature 563(7732) (2018) 546-550.

[19] J.B. Seol, J.W. Bae, J.G. Kim, H. Sung, Z. Li, H.H. Lee, S.H. Shim, J.H. Jang, W.-S. Ko, S.I. Hong, H.S. Kim, Short-range order strengthening in boron-doped high-entropy alloys for cryogenic applications, Acta Materialia 194 (2020) 366-377.

[20] J.B. Seol, J.W. Bae, Z. Li, J. Chan Han, J.G. Kim, D. Raabe, H.S. Kim, Boron doped ultrastrong and ductile high-entropy alloys, Acta Materialia 151 (2018) 366-376.

[21] M. Traversier, P. Mestre-Rinn, N. Peillon, E. Rigal, X. Boulnat, F. Tancret, J. Dhers, A. Fraczkiewicz, Nitrogen-induced hardening in an austenitic CrFeMnNi high-entropy alloy (HEA), Materials Science and Engineering: A 804 (2021) 140725.

[22] D. Raabe, M. Herbig, S. Sandlöbes, Y. Li, D. Tytko, M. Kuzmina, D. Ponge, P.P. Choi, Grain boundary segregation engineering in metallic alloys: A pathway to the design of interfaces, Current Opinion in Solid State and Materials Science 18(4) (2014) 253-261.

[23] C. Liu, W. Lu, W. Xia, C. Du, Z. Rao, J.P. Best, S. Brinckmann, J. Lu, B. Gault, G. Dehm, G. Wu, Z. Li, D. Raabe, Massive interstitial solid solution alloys achieve near-theoretical strength, Nature Communications 13(1) (2022) 1102.

[24] Z. Rao, B. Dutta, F. Körmann, W. Lu, X. Zhou, C. Liu, A.K. da Silva, U. Wiedwald, M. Spasova, M. Farle, D. Ponge, B. Gault, J. Neugebauer, D. Raabe, Z. Li, Beyond Solid Solution High-Entropy Alloys: Tailoring Magnetic Properties via Spinodal Decomposition, Advanced Functional Materials 31(7) (2021) 2007668.

[25] Y.-J. Liang, L. Wang, Y. Wen, B. Cheng, Q. Wu, T. Cao, Q. Xiao, Y. Xue, G. Sha, Y. Wang, Y. Ren, X. Li, L. Wang, F. Wang, H. Cai, High-content ductile coherent nanoprecipitates achieve ultrastrong high-entropy alloys, Nature Communications 9(1) (2018) 4063.

[26] Z. An, S. Mao, T. Yang, C.T. Liu, B. Zhang, E. Ma, H. Zhou, Z. Zhang, L. Wang, X. Han, Spinodal-modulated solid solution delivers a strong and ductile refractory high-entropy alloy, Materials Horizons 8(3) (2021) 948-955.

[27] C.C. Tasan, Y. Deng, K.G. Pradeep, M.J. Yao, H. Springer, D. Raabe, Composition Dependence of Phase Stability, Deformation Mechanisms, and Mechanical Properties of the CoCrFeMnNi High-Entropy Alloy System, JOM 66(10) (2014) 1993-2001.

[28] J.M. Torralba, P. Alvaredo, A. García-Junceda, High-entropy alloys fabricated via powder metallurgy. A critical review, Powder Metallurgy 62(2) (2019) 84-114.

[29] Y. Chen, P. Munroe, Z. Xie, S. Zhang, High-Entropy Alloy-Based Coatings, 2021, pp. 205-232.

[30] B.R. Braeckman, F. Boydens, H. Hidalgo, P. Dutheil, M. Jullien, A.L. Thomann, D. Depla, High entropy alloy thin films deposited by magnetron sputtering of powder targets, Thin Solid Films 580 (2015) 71-76.

[31] D. Depla, S. Mahieu, J.E. Greene, Chapter 5 - Sputter Deposition Processes, in: P.M. Martin (Ed.), Handbook of Deposition Technologies for Films and Coatings (Third Edition), William Andrew Publishing, Boston, 2010, pp. 253-296.

[32] S.S. Sohn, A. Kwiatkowski da Silva, Y. Ikeda, F. Körmann, W. Lu, W.S. Choi, B. Gault, D. Ponge, J. Neugebauer, D. Raabe, Ultrastrong Medium-Entropy Single-Phase Alloys Designed via Severe Lattice Distortion, Advanced Materials 31(8) (2019) 1807142.

[33] J. Brechtl, S. Chen, C. Lee, Y. Shi, R. Feng, X. Xie, D. Hamblin, A.M. Coleman, B. Straka, H. Shortt, R.J. Spurling, P.K. Liaw, A Review of the Serrated-Flow Phenomenon and Its Role in the Deformation Behavior of High-Entropy Alloys, Metals 10(8) (2020) 1101.

[34] X. Chen, Q. Wang, Z. Cheng, M. Zhu, H. Zhou, P. Jiang, L. Zhou, Q. Xue, F. Yuan, J. Zhu, X. Wu, E. Ma, Direct observation of chemical short-range order in a medium-entropy alloy, Nature 592(7856) (2021) 712-716.

[35] H. Li, H. Zong, S. Li, S. Jin, Y. Chen, M.J. Cabral, B. Chen, Q. Huang, Y. Chen, Y. Ren, K. Yu, S. Han, X. Ding, G. Sha, J. Lian, X. Liao, E. Ma, J. Sun, Uniting tensile ductility with ultrahigh strength via composition undulation, Nature 604(7905) (2022) 273-279.

[36] L. Lilensten, J.P. Couzinié, L. Perrière, A. Hocini, C. Keller, G. Dirras, I. Guillot, Study of a bcc multi-principal element alloy: Tensile and simple shear properties and underlying deformation mechanisms, Acta Materialia 142 (2018) 131-141.

[37] J. Cairney, A rival to superalloys at high temperatures, Science 370(6512) (2020) 37-38.

[38] F. Wang, G.H. Balbus, S. Xu, Y. Su, J. Shin, P.F. Rottmann, K.E. Knipling, J.-C. Stinville, L.H. Mills, O.N. Senkov, I.J. Beyerlein, T.M. Pollock, D.S. Gianola, Multiplicity of dislocation pathways in a refractory multiprincipal element alloy, Science 370(6512) (2020) 95-101.

[39] E. Ma, Unusual dislocation behavior in high-entropy alloys, Scripta Materialia 181 (2020) 127-133.

[40] F. Maresca, W.A. Curtin, Theory of screw dislocation strengthening in random BCC alloys from dilute to "High-Entropy" alloys, Acta Materialia 182 (2020) 144-162.

[41] C. Varvenne, A. Luque, W.A. Curtin, Theory of strengthening in fcc high entropy alloys, Acta Materialia 118 (2016) 164-176.

[42] R. Zhang, S. Zhao, J. Ding, Y. Chong, T. Jia, C. Ophus, M. Asta, R.O. Ritchie, A.M. Minor, Short-range order and its impact on the CrCoNi medium-entropy alloy, Nature 581(7808) (2020) 283-287.

[43] N.R. Tao, K. Lu, Nanoscale structural refinement via deformation twinning in face-centered cubic metals, Scripta Materialia 60(12) (2009) 1039-1043.

[44] J.F.C. Lins, H.R.Z. Sandim, H.J. Kestenbach, D. Raabe, K.S. Vecchio, A microstructural investigation of adiabatic shear bands in an interstitial free steel, Materials Science and Engineering: A 457(1) (2007) 205-218.

[45] N. Jia, P. Eisenlohr, F. Roters, D. Raabe, X. Zhao, Orientation dependence of shear banding in face-centered-cubic single crystals, Acta Materialia 60(8) (2012) 3415-3434.

[46] Z. Li, K.G. Pradeep, Y. Deng, D. Raabe, C.C. Tasan, Metastable high-entropy dual-phase alloys overcome the strength-ductility trade-off, Nature 534(7606) (2016) 227-230.

[47] K.G. Pradeep, N. Wanderka, P. Choi, J. Banhart, B.S. Murty, D. Raabe, Atomic-scale compositional characterization of a nanocrystalline AlCrCuFeNiZn high-entropy alloy using atom probe tomography, Acta Materialia 61(12) (2013) 4696-4706.

[48] B. Cantor, Multicomponent and High Entropy Alloys, Entropy 16(9) (2014) 4749-4768.

[49] Z. Li, C.C. Tasan, K.G. Pradeep, D. Raabe, A TRIP-assisted dual-phase high-entropy alloy: Grain size and phase fraction effects on deformation behavior, Acta Materialia 131 (2017) 323-335.

[50] J. Li, Q. Fang, B. Liu, Y. Liu, Transformation induced softening and plasticity in high entropy alloys, Acta Materialia 147 (2018) 35-41.

[51] H. Yu, J. Zhang, W. Fang, R. Chang, X. Bai, J. Yan, X. Zhang, B. Liu, F. Yin, A brief review of metastable high-entropy alloys with transformation-induced plasticity, Materials Science and Technology 36(18) (2020) 1893-1902.

[52] Z. Li, F. Körmann, B. Grabowski, J. Neugebauer, D. Raabe, Ab initio assisted design of quinary dual-phase high-entropy alloys with transformation-induced plasticity, Acta Materialia 136 (2017) 262-270.

[53] W. Lu, C.H. Liebscher, G. Dehm, D. Raabe, Z. Li, Bidirectional Transformation Enables Hierarchical Nanolaminate Dual-Phase High-Entropy Alloys, Advanced Materials 30(44) (2018) 1804727.

[54] C.S. Pande, K.P. Cooper, Nanomechanics of Hall–Petch relationship in nanocrystalline materials, Progress in Materials Science 54(6) (2009) 689-706.

[55] W. Steurer, Single-phase high-entropy alloys – A critical update, Materials Characterization 162 (2020) 110179.

[56] D. Williams, C. Carter, Transmission Electron Microscopy: A Textbook for Materials Science, 2009.

[57] B. Gault, M.P. Moody, J.M. Cairney, S.P. Ringer, Atom Probe Microscopy, 1st ed. 2012. ed., Springer New York, New York, NY, 2012.

[58] B. Gault, A. Chiaramonti, O. Cojocaru-Mirédin, P. Stender, R. Dubosq, C. Freysoldt, S.K. Makineni, T. Li, M. Moody, J.M. Cairney, Atom probe tomography, Nature Reviews Methods Primers 1(1) (2021) 51.

[59] S. Zaefferer, A critical review of orientation microscopy in SEM and TEM, Crystal Research and Technology 46(6) (2011) 607-628.

[60] G.C. Sneddon, P.W. Trimby, J.M. Cairney, Transmission Kikuchi diffraction in a scanning electron microscope: A review, Materials Science and Engineering: R: Reports 110 (2016) 1-12.

[61] J. Jeong, N. Cautaerts, G. Dehm, C.H. Liebscher, Automated Crystal Orientation Mapping by Precession Electron Diffraction-Assisted Four-Dimensional Scanning Transmission Electron Microscopy Using a Scintillator-Based CMOS Detector, Microscopy and Microanalysis 27(5) (2021) 1102-1112.

[62] S. Zhang, C. Scheu, Evaluation of EELS spectrum imaging data by spectral components and factors from multivariate analysis, Microscopy (Oxford, England) 67 (2017) 1-9.

[63] W.C. Oliver, An improved technique for determining hardness and elastic modulus using load and displacement sensing indentation experiments, Journal of Materials Research 7(6) (1992) 1564-1583.

[64] J.R. Greer, W.C. Oliver, W.D. Nix, Size dependence of mechanical properties of gold at the micron scale in the absence of strain gradients, Acta Materialia 53(6) (2005) 1821-1830.

[65] J. Wang, P. Jiang, F. Yuan, X. Wu, Chemical medium-range order in a medium-entropy alloy, Nature Communications 13(1) (2022) 1021.

[66] K. Wieczerzak, O. Nowicka, S. Michalski, T.E.J. Edwards, M. Jain, T. Xie, L. Pethö, X. Maeder, J. Michler, Ultrastrong nanocrystalline binary alloys discovered via high-throughput screening of the CoCr system, Materials & Design 205 (2021) 109710.

[67] N.D. Stepanov, D.G. Shaysultanov, G.A. Salishchev, M.A. Tikhonovsky, Structure and mechanical properties of a light-weight AlNbTiV high entropy alloy, Materials Letters 142 (2015) 153-155.

[68] O.N. Senkov, G.B. Wilks, J.M. Scott, D.B. Miracle, Mechanical properties of Nb25Mo25Ta25W25 and V20Nb20Mo20Ta20W20 refractory high entropy alloys, Intermetallics 19(5) (2011) 698-706.

[69] S.-P. Wang, J. Xu, TiZrNbTaMo high-entropy alloy designed for orthopedic implants: As-cast microstructure and mechanical properties, Materials Science and Engineering: C 73 (2017) 80-89.

[70] O.N. Senkov, C.F. Woodward, Microstructure and properties of a refractory NbCrMo0.5Ta0.5TiZr alloy, Materials Science and Engineering: A 529 (2011) 311-320.

[71] C.-C. Juan, M.-H. Tsai, C.-W. Tsai, C.-M. Lin, W.-R. Wang, C.-C. Yang, S.-K. Chen, S.-J. Lin, J.-W. Yeh, Enhanced mechanical properties of HfMoTaTiZr and HfMoNbTaTiZr refractory high-entropy alloys, Intermetallics 62 (2015) 76-83.

[72] Z.D. Han, N. Chen, S.F. Zhao, L.W. Fan, G.N. Yang, Y. Shao, K.F. Yao, Effect of Ti additions on mechanical properties of NbMoTaW and VNbMoTaW refractory high entropy alloys, Intermetallics 84 (2017) 153-157.

[73] B. Kang, J. Lee, H.J. Ryu, S.H. Hong, Ultra-high strength WNbMoTaV high-entropy alloys with fine grain structure fabricated by powder metallurgical process, Materials Science and Engineering: A 712 (2018) 616-624.

[74] Y. Long, X. Liang, K. Su, H. Peng, X. Li, A fine-grained NbMoTaWVCr refractory high-entropy alloy with ultra-high strength: Microstructural evolution and mechanical properties, Journal of Alloys and Compounds 780 (2019) 607-617.

[75] S. Wei, S. Kim, J.Y. Kang, Y. Zhang, T. Furuhara, E.S. Park, C.C. Tasan, Natural-mixing guided design of refractory high-entropy alloys with as-cast tensile ductility, Nature Materials (2020) 1-7.

[76] T. Yang, Y.L. Zhao, W.P. Li, C.Y. Yu, J.H. Luan, D.Y. Lin, L. Fan, Z.B. Jiao, W.H. Liu, X.J. Liu, J.J. Kai, J.C. Huang, C.T. Liu, Ultrahigh-strength and ductile superlattice alloys with nanoscale disordered interfaces, Science 369(6502) (2020) 427.

[77] S.J. Sun, Y.Z. Tian, H.R. Lin, H.J. Yang, X.G. Dong, Y.H. Wang, Z.F. Zhang, Achieving high ductility in the 1.7 GPa grade CoCrFeMnNi high-entropy alloy at 77 K, Materials Science and Engineering: A 740-741 (2019) 336-341.

[78] B. Gwalani, S. Gorsse, D. Choudhuri, Y. Zheng, R.S. Mishra, R. Banerjee, Tensile yield strength of a single bulk Al0.3CoCrFeNi high entropy alloy can be tuned from 160 MPa to 1800 MPa, Scripta Materialia 162 (2019) 18-23.

[79] W. Guo, B. Liu, Y. Liu, T. Li, A. Fu, Q. Fang, Y. Nie, Microstructures and mechanical properties of ductile NbTaTiV refractory high entropy alloy prepared by powder metallurgy, Journal of Alloys and Compounds 776 (2019) 428-436.

[80] C. Chen, Y. Fan, H. Zhang, J. Hou, W. Zhang, P. Wei, W. Wang, J. Qin, R. Wei, T. Wang, F. Li, A novel Fe-Co-Ni-Si high entropy alloy with high yield strength, saturated magnetization and Curie temperature, Materials Letters 281 (2020) 128653.

[81] H. Yao, Z. Tan, D. He, Z. Zhou, Z. Zhou, Y. Xue, L. Cui, L. Chen, G. Wang, Y. Yang, High strength and ductility AlCrFeNiV high entropy alloy with hierarchically heterogeneous microstructure prepared by selective laser melting, Journal of Alloys and Compounds 813 (2020) 152196.

[82] W. Lai, F. Vogel, X. Zhao, B. Wang, Y. Yi, D. You, X. Tong, W. Li, X. Yu, X. Wang, Design of BCC refractory multi-principal element alloys with superior mechanical properties, Materials Research Letters 10(3) (2022) 133-140.

[83] N. Yurchenko, E. Panina, D. Shaysultanov, S. Zherebtsov, N. Stepanov, Refractory high entropy alloy with ductile intermetallic B2 matrix / hard bcc particles and exceptional strain hardening capacity, Materialia 20 (2021) 101225.

[84] I.A. Su, K.-K. Tseng, J.-W. Yeh, B. El-Sayed, C.-H. Liu, S.-H. Wang, Strengthening mechanisms and microstructural evolution of ductile refractory medium-entropy alloy Hf20Nb10Ti35Zr35, Scripta Materialia 206 (2022) 114225.

[85] S. Tsianikas, Y. Chen, J. Jeong, S. Zhang, Z. Xie, Self-toughened high entropy alloy with a body-centred cubic structure, Nanoscale 13(6) (2021) 3602-3612.